

# Validation & Verification of Hydro-Elastic Analyses for Marine Propellers

MSc Thesis

K. van de Sanden





# Validation & Verification of Hydro-Elastic Analyses for Marine Propellers

MSc Thesis

by

K. van de Sanden

to obtain the degree of Master of Science  
at the Delft University of Technology,  
to be defended publicly on Wednesday August 26, 2020 at 2:00 PM.

Student number: 4955005  
Project duration: November 19, 2019 – August 26, 2020  
Thesis committee: Dr. ir. H. C. J. van Wijngaarden, MARIN  
Prof. dr. ir. T. J. C. van Terwisga, MARIN, TU Delft  
Ir. H. C. Neatby, TU Delft, DRDC  
Dr. ir. L. Pahlavan, TU Delft  
Dr. ir. A. Laskari, TU Delft



# Preface

A few years back my knowledge on ships, let alone marine propellers was very limited, though I have always had some affinity with the maritime sector. Nonetheless, I enrolled in the Marine Technology MSc. program where I soon realized to have made the right choice. Since many of my chosen subjects were related to fluid dynamics and marine propulsion systems, I soon determined that this is a direction in which I wanted to proceed my study. As I also have much interest in a sustainable future for shipping, the ultimate goal of applying composite propellers as a means to increase efficiency sounded very appealing to me.

Although my time spent at MARIN turned out a little shorter than intended due to some virus, I have still greatly enjoyed the colleagues that I have met. I would like to express my gratitude to Erik van Wijngaarden and Holly Neatby. As my daily supervisor at MARIN, Erik has been of great help in explaining the theory and discussing details, where I rapidly noticed that my opinion, as just a simple student, was very much valued. Holly has often been of great help pointing me in the right direction, and in setting up the validation and verification plan. Off course I would also like to thank Tom van Terwisga, for keeping an eye on the bigger picture and introducing me to MARIN in the first place. Finally I would like to thank Pooria Pahlavan for evaluating my work, and his guidance during the thesis.

*K. van de Sanden  
Delft, July 2020*



# Summary

To date, the vast majority of marine propellers has been manufactured by roughly the same materials as a century ago, viz. Nickel-Aluminium Bronze alloys. A fairly recent development is the rising interest in the application of composite propellers, as they have great potential to outperform the metallics. They offer good corrosion resistance, fatigue resistance, a low magnetic signature for defense purposes, and a high strength to stiffness ratio. When propelling a ship, a high strength to stiffness ratio may be utilized by adapting the geometry passively to suit the loading condition more optimal. A possible purpose of applying flexible (composite) propellers is to mitigate cavitation behaviour by utilizing their large deformations when subjected to loads.

The hydrodynamic response of a flexible propeller in a flow field can be predicted by the use of Fluid-Structure Interaction (FSI) software, which is currently being developed at the Maritime Research Institute Netherlands (MARIN). The project is called Composite Propeller Application (ComPropApp). ComPropApp combines existing fluid and structural solvers, PROCAL and TRIDENT/VAST. PROCAL is a boundary element method used almost exclusively for the analysis of marine propellers, and TRIDENT/VAST is a finite element solver for marine applications. However, as the ComPropApp is still under development it needed to be verified and validated, which is the main objective of this thesis.

The first part of this thesis treats the theory applied in the FSI software. The working principles of the structural and fluid solvers are elaborated in some detail, together with the applied adjustments to the software. Further, the coupling mechanisms to combine the two packages in an iterative way are described. ComPropApp can be applied in uniform flow (steady), and non-uniform (unsteady) flow. These different conditions require different solution methods, hence the program contains a steady and unsteady FSI module. The unsteady module is computationally more comprehensive, as it includes important dynamic effects on the structural as well as the fluid side.

Next, the verification study is described. A suitable propeller model was selected to perform the verification, a model size version of the Wageningen C4 – 40 series was selected. As an initial step in the verification study, a falsification study was applied for the steady and unsteady FSI modules. This led to the discovery of a few errors, to which corrections have been applied to improve the program. With an updated version, computations with a number of different materials were performed to finalize the verification.

The Wageningen C4 – 40 propeller has been manufactured at MARIN to be used in the experimental validation. The propeller was machined out of the isotropic polyurethane material SikaBlock M700. The experiments were performed in the cavitation tunnel testing facility at MARIN. Here the propeller operated in several different conditions, i.e. different advance ratios in uniform and non-uniform flows. A number of ComPropApp simulations were used to set these testing conditions. Initially determining the experimental conditions had the purpose to obtain deflections large enough to be measured accurately whilst remaining well within the elastic regime. The results were then compared to the computations in order to successfully validate the ComPropApp.

Lastly, in order to study the benefits that composite propellers have to offer, it was investigated in which conditions cavitation is expected to occur, and whether the application of a composite can reduce cavitation. This is for theoretical research only, since the polyurethane propeller would fail far before reaching cavitating conditions. The use of PROCAL was made to analyze the cavitating behavior for an undeformed propeller in a wakefield. From this, a requirement for twist deformation was set up. Based on these requirements, a range of composite materials was defined, and with it, ComPropApp computations were performed. The resulting displacements and pressure distributions were then compared for the rigid and composite cases.

With the presented verification study, it can be concluded that the FSI software is capable of providing realistic computation results. However, small unresolved errors remain, most important of which are caused by interpolation steps performed in the conversion between fluid and structural solver. The validation study has led to conclude that the unsteady FSI module is capable of qualitatively predicting the bend deformations in open water conditions. However, due to the large uncertainties arising from the SikaBlock material properties and machining quality, the measurements cannot be utilized to define the accuracy of the FSI software. In wakefield conditions the additional uncertainty of the wake velocity distribution meant that these measurements are inconclusive, hence the validation was only performed for open water conditions. The material

study with the purpose of mitigating cavitation has shown potential in the application of anisotropic materials. Composites with a specific ply orientation sequence have the possibility of realizing bend twist coupling motions, such that the propeller would unload itself when the local advance ratio decreases, with reduced cavitation as an expected result.

# Contents

<b>1</b>	<b>Introduction</b>	<b>1</b>
<b>2</b>	<b>Composite Propeller Application</b>	<b>3</b>
2.1	Introduction . . . . .	3
2.2	Boundary Element Method . . . . .	4
2.2.1	Governing equations. . . . .	4
2.2.2	Discretization . . . . .	5
2.2.3	Iterative Pressure Kutta Condition . . . . .	8
2.2.4	Input files . . . . .	9
2.2.5	Limitations. . . . .	10
2.3	Finite Element Method . . . . .	10
2.3.1	Static analysis . . . . .	11
2.3.2	Dynamic Analysis . . . . .	11
2.3.3	Input files . . . . .	13
2.4	Adaptations to BEM and FEM software . . . . .	13
2.4.1	Adaptations to PROCAL . . . . .	13
2.4.2	PROCAL to TRIDENT/VAST conversion . . . . .	14
2.4.3	TRIDENT/VAST . . . . .	14
2.5	Steady FSI Analysis . . . . .	15
2.6	Unsteady FSI Analysis. . . . .	16
2.6.1	Frequency domain solution . . . . .	16
2.6.2	Coupling Iteration Methods . . . . .	17
2.6.3	Coupling procedure . . . . .	17
<b>3</b>	<b>Verification study</b>	<b>19</b>
3.1	Introduction . . . . .	19
3.2	Input files setup. . . . .	20
3.2.1	PROCAL control parameters . . . . .	20
3.2.2	Panel grid construction . . . . .	21
3.2.3	Open water diagram . . . . .	21
3.2.4	TRIDENT control parameters . . . . .	22
3.2.5	Finite element mesh . . . . .	22
3.3	Processing ComPropApp output . . . . .	23
3.4	Steady FSI analysis . . . . .	25
3.4.1	Analytic solution. . . . .	25
3.4.2	Manual coupling procedure . . . . .	27
3.4.3	Validity limits . . . . .	27
3.5	Unsteady FSI analysis. . . . .	29
3.5.1	Open water conditions. . . . .	29
3.5.2	Wakefield conditions. . . . .	32
3.5.3	Oblique wake conditions. . . . .	34
3.6	Verification . . . . .	36
3.6.1	Sikablock M700 . . . . .	37
3.6.2	Epoxy . . . . .	39
3.6.3	Glass fiber reinforced epoxy: . . . . .	41
3.6.4	Bronze:. . . . .	42
3.7	Conclusions. . . . .	43

<b>4 Experiments</b>	<b>45</b>
4.1 Introduction . . . . .	45
4.2 Experimental setup . . . . .	45
4.3 Defining conditions. . . . .	48
4.3.1 Deformation size. . . . .	48
4.3.2 Tip deformation matrix . . . . .	49
4.4 Results . . . . .	50
4.4.1 Open Water . . . . .	50
4.4.2 Wakefield Conditions . . . . .	51
4.5 Conclusions. . . . .	51
<b>5 Composite application</b>	<b>53</b>
5.1 Introduction . . . . .	53
5.2 Cavitation on marine propellers . . . . .	53
5.2.1 Tip vortex cavitation . . . . .	54
5.2.2 Sheet cavitation . . . . .	55
5.2.3 Cloud cavitation . . . . .	56
5.2.4 Cavitation number. . . . .	56
5.2.5 Modelling of Cavitation . . . . .	57
5.2.6 Application to the Wageningen C4-40 series . . . . .	57
5.3 Material setup. . . . .	60
5.3.1 Composite properties . . . . .	60
5.3.2 Defining material properties. . . . .	63
5.4 Results . . . . .	65
5.5 Conclusions. . . . .	67
<b>6 Recommendations</b>	<b>69</b>
6.1 ComPropApp Guidelines . . . . .	71
<b>A Composite properties</b>	<b>73</b>
<b>B Datasheet SikaBlock M700</b>	<b>75</b>
<b>C Cavitation</b>	<b>77</b>
<b>D Constructing ComPropApp input files</b>	<b>79</b>
D.1 Propeller Geometry File (obtained from [3]) . . . . .	79
D.1.1 Contents and Layout. . . . .	79
D.1.2 Current Provide Restrictions on Input Data and Formatting . . . . .	79
D.1.3 Example Propeller Geometry File . . . . .	80
D.2 Trident instructions files . . . . .	81
D.2.1 Meshing instructions . . . . .	81
D.2.2 Composite properties . . . . .	82
D.3 PROCAL Control File . . . . .	84
<b>Bibliography</b>	<b>87</b>



# Introduction

Marine propellers have been applied in numerous configurations to optimize their efficiency, noise emission, erosion/fatigue resistance, operational flexibility, etc. Up until now, the vast majority of propellers is still manufactured by the same materials as a century ago, namely Nickel-Aluminium Bronze alloys. Within the maritime sector, the interest in composite materials has grown substantially over the past decades. When focusing upon the application of marine propulsion, composites show potential due to excellent material properties at reduced weight compared to metallics. They provide excellent resistance to salt water and several chemicals, yielding improved corrosion resistance and mitigated biological growth [31]. The aerospace industry has developed new technologies using composites for lifting bodies, such as turbines, rotors, and wings. These structures have shown improvements in vibration damping properties, fatigue resistance, and life-cycle cost [31].

When operating below a vessel, marine propellers usually encounter a non-uniform inflow field. There are several causes for this, among which the turbulent boundary layer beneath the hull created by the water viscosity. Further, non-uniform inflow can occur when a propeller is positioned under an inclination when there is propeller-rudder interaction or interaction with the free surface. Other factors such as waves and currents, or presence of other propellers are of influence as well. Non-uniform inflow adversely influences the conditions in which the propeller operates, since the effective inflow angle on the blades becomes time-dependent. With a rapid variation in angles of attack, the blade loading becomes a time dependent as well, which yields a periodic fluctuation in loads. A disadvantage of time-dependent inflow angles is that they may overshoot a certain angle of attack yielding sheet- and cloud cavitation. When these types of cavitation would already have occurred in a uniform flow, larger problems arise as a result of the varying inflow angle causing the cavity to grow and shrink throughout a revolution. This is a highly unstable type of cavitation and leads to large pressure pulses and in some cases permanent damages to the propeller or hull.

Since composites have a high strength to stiffness ratio, an interesting application is to design a propeller that passively adapts its shape to the flow conditions. It is appealing to utilize bend and twist coupling between a composite propeller and the fluid in which it is operating. Specifically, in higher loading conditions the pitch distribution adjusts passively to ideally obtain a constant angle of attack when operating in a non-uniform flow. In reality, this is of course limited to mitigating the fluctuations in the angle of attack as much as possible. Ultimately this will reduce noise and vibrations and it has the potential to improve the overall propulsion efficiency. An important objective, since emission policies and regulations regarding the maritime sector are tightening. For a realistic attempt to reduce the environmental impact of shipping, carbon dioxide, nitrogen oxides, particulate matter but also noise emissions have to be mitigated or avoided altogether within the near future. Composite propellers have the potential to offer a small step towards achieving these future emission goals.

The analysis of flexible propellers requires a so-called Fluid Structure Interaction (FSI) method. Two approaches are possible, a partitioned and a monolithic approach. The partitioned approach is based on separately solving the fluid dynamics and structural dynamics, where the interaction between both is obtained by performing coupling iterations. The monolithic approach solves the fluid and structural dynamics simultaneously, but has the drawback of high complexity, therefore limiting the applicability to structures with a relatively small deformation [17]. Other than that, it is limited to sub-cavitating conditions [20]. The coupled approach has the advantage of combining existing black-box software. Such software is a Boundary Element

Method (BEM) to solve fluid problems, and a Finite Element Method (FEM) for structural application.

In the past, numerous methods have been presented for FSI analyses, but only a few of which treat propellers operating in a non-uniform flow. These methods are based on certain assumptions, e.g. neglected fluid stiffness effects, relatively small deformations, etc. [9, 29, 30]. These assumptions may limit their applicability in realistic conditions. To completely utilize the benefits that flexible propellers have to offer, a reliable method for FSI is required, which has the ability to compute the hydro-elastic response of flexible propellers in different operating conditions. These conditions may be small to large blade deformations, cavitating or non-cavitating, uniform or non-uniform flow, and isotropic or anisotropic materials. This thesis presents a verification and validation study on software specifically developed for flexible composite propellers. The first chapter elaborates on the applied software in the fluid structure interaction software, this is followed by the verification study, after which the validation is carried out. The final chapter in the thesis describes a preliminary design of a composite propeller, focusing on utilizing the material properties of different composites with the purpose of alleviating cavitation.

# 2

## Composite Propeller Application

### 2.1. Introduction

The Composite Propeller Application (ComPropApp) is a software application developed at MARIN in collaboration with Lloyd's Register Applied Technology Group. It is a coupled version of PROCAL, a Boundary Element Method (BEM) for propeller analysis, and Finite Element Method (FEM) software for the structural analysis. VAST/Trident is the applied FEM package, although combinations with ANSYS and NASTRAN are under development as well. The ComPropApp is being developed for examining the performance of flexible propellers in behind ship conditions, as well as open water conditions. It applies an iterative coupling method, which is based on the work performed by Ph.D. student Pieter Maljaars [20]. The simulation is built up from several Fluid Structure Interaction (FSI) cycles, where the BEM model computes the loads, the FEM model the deformations with which the new geometry is updated to perform a new iteration. Updating the geometry is performed by constructing new panel files with the MATLAB based PROPART Toolbox [12]. This chapter describes the working principles of the separate solvers, and the coupling mechanisms applied in the ComPropApp.

## 2.2. Boundary Element Method

The Boundary Element Method is a powerful tool for flow analyses, where only the surface (boundary) of the domain is required to be discretised, saving significant computational time compared to Computational Fluid Dynamics (CFD) solvers. Boundary Element Methods for marine propulsion purposes are capable of calculating several flow conditions passed (ducted, podded) propellers or rudders. In the scope of this research, steady (open water conditions) and unsteady flow (ship wake conditions) along a propeller are simulated.

### 2.2.1. Governing equations

PROCAL is BEM software for analyzing flow around a propeller, it was developed by MARIN for the CRS (Co-operative Research Ships) organisation. It solves the integral equation for the velocity potential in a fluid, based on the Morino formulation. This is a low-order potential-based panel method, and has been very popular particularly in the field of various turbo machinery systems, including marine propulsion systems [25]. In the Morino formulation the propeller induced velocity disturbances are assumed irrotational. A scalar variable  $\phi$  is defined, denoting the disturbance velocity potential. The total velocity vector is denoted as  $\mathbf{v}$ , and can be written as:

$$\mathbf{v}(\mathbf{x}, t) = \mathbf{v}_\infty(\mathbf{x}, t) + \nabla\phi(\mathbf{x}, t) \quad (2.1)$$

Here  $\mathbf{x}$  is the position vector,  $t$  denotes time and  $\mathbf{v}_\infty$  is the undisturbed velocity vector. Alternatively, the undisturbed velocity can be written as a function of the ship wake field velocity  $\mathbf{v}_w$  and the angular velocity  $\boldsymbol{\theta}$ :

$$\mathbf{v}_\infty(\mathbf{x}, t) = \mathbf{v}_w(\mathbf{x}, t) - \boldsymbol{\theta} \times \mathbf{x} \quad (2.2)$$

The angular velocity  $\boldsymbol{\theta}$  is a function of the rotational shaft speed,  $n$ :  $\boldsymbol{\theta} = (2\pi n, 0, 0)$ . In potential theory the flow is assumed constant in density and incompressible, therefore the Laplace equation is applicable:

$$\nabla^2\phi(\mathbf{x}, t) = 0 \quad (2.3)$$

The pressures ( $p$ ) of the fluid can be determined using Bernoulli's law:

$$\frac{\partial\phi}{\partial t} + \frac{1}{2}|\mathbf{v}|^2 + \frac{p}{\rho_w} + gz = \frac{p_\infty}{\rho_w} + \frac{1}{2}|\mathbf{v}_\infty|^2 \quad (2.4)$$

where  $\rho_w$  is the water density,  $g$  the gravitational constant and  $p_\infty$  the undisturbed pressure upstream, satisfying the hydrostatic law:  $p_\infty = p_{atm} + \rho_w g z_{shaft}$ . The atmospheric pressure is denoted by  $p_{atm}$  and  $z_{shaft}$  is the depth of the shaft. In the Morino formulation, a superposition of sources and dipoles is applied to produce the velocity field which suffices the boundary conditions. Sources and dipoles are algebraic functions which satisfy Laplace's equation, and can be combined to construct flowfields. Dipoles can be interpreted as the combination of a source and sink of equal strength, kept at an infinitesimally small distance apart.

Since the propeller can be considered as an impermeable surface, the first boundary condition applied in PROCAL states that the normal velocity at the surface equals zero:

$$\mathbf{n} \cdot \mathbf{v} = 0 \rightarrow \mathbf{n} \cdot \nabla\phi = -\mathbf{n} \cdot \mathbf{v}_\infty \quad (2.5)$$

with  $\mathbf{n}$  denoting the surface normal. This boundary condition specifies the source strength  $\sigma$  of each panel to a known value since both the undisturbed velocity and normal vectors at each panel are known:

$$\sigma = -\mathbf{n} \cdot \mathbf{v}_\infty \quad (2.6)$$

The second boundary condition states that the dipole strength is equal to the potential difference across the panel. At the propeller blade, assuming the potential outside the volume  $V$  is zero, the following condition applies at the blade surface:

$$\mu = -\phi \quad (2.7)$$

with  $\mu$  denoting the dipole strength at the blade. Assuming locally two-dimensional flow, the dipole strength of the wake  $\mu_w$  is expressed as the potential difference between the upper and lower trailing edge:

$$\mu_w = -(\phi_{TEupper} - \phi_{TElower}) = \Delta\phi \quad (2.8)$$

In PROCAL, the wake sheet of the propeller is assumed as an imaginary surface area that cannot support a pressure difference between both sides, yielding the following dynamic boundary condition:

$$\Delta p = p^+ - p^- = 0 \quad (2.9)$$

with  $p^+$  the upper side and  $p^-$  the lower side of the wake sheet. This boundary condition is known as the Kutta condition, which is treated in more detail in section 2.2.3. The wake sheet is modeled as an impermeable stream-surface of the flow, hence the following kinematic boundary condition applies:

$$\mathbf{v} \cdot \mathbf{n} = 0 \quad (2.10)$$

The relation between the potential in the fluid domain and the source strengths is given by the integral equation as follows from the third Green's Identity. With the Morino method this can be written as:

$$\begin{aligned} \epsilon(\mathbf{a})\phi(\mathbf{a}, t) &= \int_{S_B} \left[ \phi(\mathbf{b}, t) \frac{\partial G(\mathbf{a}, \mathbf{b})}{\partial \mathbf{n}_b} - G(\mathbf{a}, \mathbf{b}) \frac{\partial \phi(\mathbf{b}, t)}{\partial \mathbf{n}_b} \right] dS \\ &+ \int_{S_W} \left[ \Delta \phi(\mathbf{b}, t) \frac{\partial G(\mathbf{a}, \mathbf{b})}{\partial \mathbf{n}_b} - G(\mathbf{a}, \mathbf{b}) \Delta \left( \frac{\partial \phi(\mathbf{b}, t)}{\partial \mathbf{n}_b} \right) \right] dS \end{aligned} \quad (2.11)$$

Here  $\mathbf{a}$  is a field point, and  $\mathbf{b}$  is a point on the boundary surface. The outward normal at position  $\mathbf{b}$  is denoted as  $\mathbf{n}_b$ ,  $\epsilon$  is the solid angle of an infinitesimal sphere around the field point. when  $\mathbf{a}$  is on the boundary surface,  $\epsilon = 2\pi$ . The body and wake field surfaces are denoted by  $S_B$  and  $S_W$  respectively.  $G$  is the Green's function for the Laplace equation and is defined as:

$$G(\mathbf{a}, \mathbf{b}) = \frac{1}{r(\mathbf{a}, \mathbf{b})} = \frac{1}{|\mathbf{r}|} = \frac{1}{|\mathbf{a} - \mathbf{b}|} \quad (2.12)$$

with  $\mathbf{r}$  the vector connecting a surface point  $\mathbf{b}$  with a field point. Then, in the BEM a series of collocation points are taken as field points. Applying the dynamic boundary condition for the wake sheet, yields the following integral equation:

$$\begin{aligned} 2\pi\phi(\mathbf{a}, t) &= \int_{S_B} \left[ \phi(\mathbf{b}, t) \frac{\partial G(\mathbf{a}, \mathbf{b})}{\partial \mathbf{n}_b} - \frac{\partial \phi(\mathbf{b}, t)}{\partial \mathbf{n}_b} G(\mathbf{a}, \mathbf{b}) \right] dS \\ &+ \int_{S_W} \Delta \phi(\mathbf{b}, t) \frac{\partial G(\mathbf{a}, \mathbf{b})}{\partial \mathbf{n}_b} dS \end{aligned} \quad (2.13)$$

Alternatively, written in terms of source strengths,  $\sigma$ , and dipole strengths,  $\mu$ :

$$\phi(\mathbf{p}) = -\frac{1}{2\pi} \int_{S_B} \left[ \mu \mathbf{n} \cdot \nabla \left( \frac{1}{|\mathbf{r}|} \right) + \sigma \frac{1}{|\mathbf{r}|} \right] dS - \frac{1}{2\pi} \int_{S_W} \left[ \mu_W \mathbf{n} \cdot \nabla \left( \frac{1}{|\mathbf{r}|} \right) \right] dS \quad (2.14)$$

When a deformable body is being considered, operation in an unsteady flow field or both, the vector  $\mathbf{b}$  and surface areas become time dependent. For such situation, equation (2.14) transforms into the following:

$$\begin{aligned} 2\pi\phi(\mathbf{a}(t), t) &= \int_{S_B(t)} \left[ \phi(\mathbf{b}(t), t) \frac{\partial G(\mathbf{a}(t), \mathbf{b}(t))}{\partial \mathbf{n}_b(t)} - \frac{\partial \phi(\mathbf{b}(t), t)}{\partial \mathbf{n}_b(t)} G(\mathbf{a}(t), \mathbf{b}(t)) \right] dS \\ &+ \int_{S_W(t)} \Delta \phi(\mathbf{b}(t), t) \frac{\partial G(\mathbf{a}(t), \mathbf{b}(t))}{\partial \mathbf{n}_b(t)} dS \end{aligned} \quad (2.15)$$

In the next section, this integral equation will be solved in a discretization procedure.

### 2.2.2. Discretization

PROCAL solves equations (2.14) and (2.15) by discretizing the surfaces  $S_B$  and  $S_W$  to a finite number of panels ( $N_{tot}$ ). The integral equation is applied to collocation points of each panel to ultimately reach a system of equations with unknown source and dipole elements strengths. This system of equations can be solved by imposing the boundary conditions. In the following sections, the PROCAL calculations in the case of a non-cavitating propeller are briefly explained.

PROCAL decomposes boundary surfaces in the fluid domain, i.e. the blade and wake surface in a key part and a symmetry part. The key part contains one blade with its corresponding hub section and wake sheet. The symmetry part includes the other blades, hub sections and wake sheets. This division is practical, since it yields a smaller system of equations by utilizing the propeller's symmetric properties. Figure 2.1 shows the geometry of a propeller and wake divided into panels. The parameters displayed in this figure are:

- $N_{surf}$ : Number of surfaces, in this case two; hub and blade

- $N_{sym}$ : Number of symmetry parts, equal to number of blades.
- $N_i$ : Number of chordwise panels on propeller.
- $N_j$ : Number of spanwise panels on propeller.
- $N_{wi}$ : Number of streamwise panels on the wake sheet.
- $N_{wj}$ : Number of radial panels on the wake sheet

In discretized form for a steady simulation, equation (2.14) becomes:

$$\begin{aligned} \sum_{isurf=1}^{N_{surf}} \sum_{isym=1}^{N_{sym}} \sum_{i=1}^{N_i} \sum_{j=1}^{N_j} \mathbf{D}_{nij} \phi_{ij} + \sum_{isurf=1}^{N_{surf}} \sum_{isym=1}^{N_{sym}} \sum_{i=1}^{N_{wi}} \sum_{i=1}^{N_{wi}} \mathbf{W}_{nij} \Delta \phi_{ij} \\ = \sum_{isurf=1}^{N_{surf}} \sum_{isurf=1}^{N_{sym}} \sum_{i=1}^{N_i} \sum_{j=1}^{N_j} \mathbf{S}_{nij} \sigma_{ij} \end{aligned} \quad (2.16)$$

Here  $\mathbf{D}$ ,  $\mathbf{W}$  and  $\mathbf{S}$  denote the hydrodynamic coefficient matrices for the body dipoles, wake dipoles and body sources respectively.  $n$  ranges from one up to  $N_{total}$ , which is the total number of panels. In the case of a flexible propeller operating in unsteady flow, it becomes more complex as all the influence coefficients are now time dependent. The following equation applies:

$$\begin{aligned} \sum_{isurf=1}^{N_{surf}} \left[ \sum_{j=1}^{N_j} \sum_{i=1}^{N_i} \mathbf{D}_{nij}^k \phi_{ij}^k + \sum_{j=1}^{N_{wj}} \mathbf{W}_{n1j}^k \Delta \phi_{1j}^k \right] = \sum_{isurf=1}^{N_{surf}} \left[ \sum_{j=1}^{N_j} \sum_{i=1}^{N_i} \mathbf{S}_{nij}^k \sigma_{ij}^k + \sum_{j=1}^{N_{wj}} \sum_{i=1}^{N_{wi}} \mathbf{W}_{nij}^k \Delta \phi_{ij}^k \right] \\ - \sum_{isurf=1}^{N_{surf}} \sum_{isym=2}^{N_{sym}} \left[ \sum_{j=1}^{N_j} \sum_{i=1}^{N_i} \mathbf{D}_{nij}^{k_{isym}} \phi_{ij}^{k_{isym}} + \sum_{j=1}^{N_j} \sum_{i=1}^{N_i} \mathbf{S}_{nij}^{k_{isym}} \sigma_{ij}^{k_{isym}} - \sum_{j=1}^{N_{wj}} \sum_{i=1}^{N_{wi}} \mathbf{W}_{nij}^{k_{isym}} \Delta \phi_{ij}^{k_{isym}} \right] \end{aligned} \quad (2.17)$$

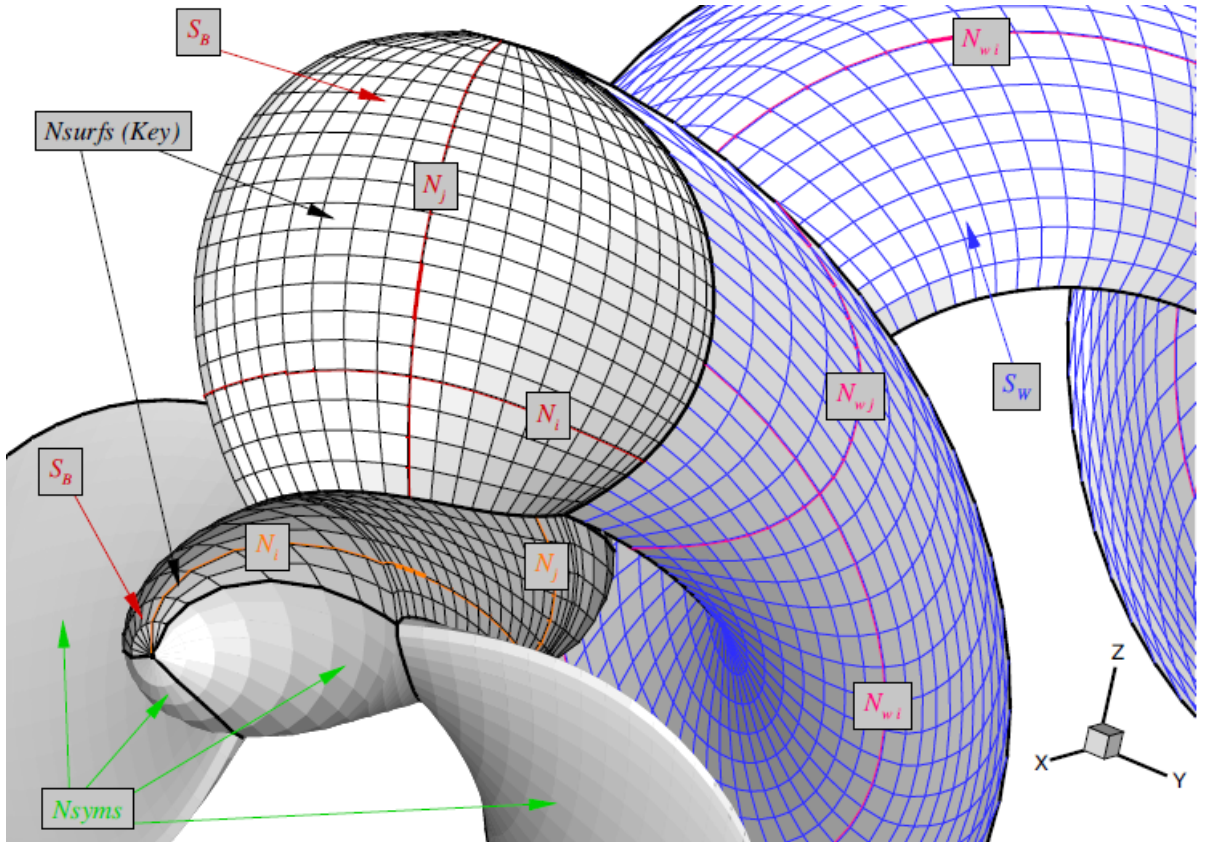


Figure 2.1: Parameters for the geometry discretization in PROCAL (figure obtained from [20])

In this equation the time step times the revolution is denoted by  $k$  ( $k = N_{revs} \cdot N_{time}$ ).  $k_{isym}$  denotes the moment where the key surfaces were at the position where the symmetry surface is at the current step. Since memorizing all symmetry surface coefficients for each time step is computationally heavy, it was chosen to use these coefficients at time step  $k$ , instead of  $k_{isym}$ . This assumption has been validated in [20] and can safely be used, since the symmetry surfaces are in the far-field relative to the key blade, hence the effects are negligible. To find the potential, the system of equations above can be solved using the method of Lower Upper (LU) decomposition.

**Velocities & Pressures** With the potential function at the surfaces computed, it is possible to determine the velocity and pressure components. The velocities are defined as the spatial derivatives of the potential. However, the coordinate system for which the potential is derived is curvilinear since the panel coordinates are geometric surfaces. Two directions,  $s_1$  and  $s_2$ , corresponding to respectively the  $i$  and  $j$  index of the panel grid form this curvilinear system with unit vectors  $(\mathbf{t}_1, \mathbf{t}_2)$ . This is transformed to an orthogonal coordinate system with unit vectors  $(\mathbf{e}_1, \mathbf{e}_2)$ .

$$\begin{aligned}\mathbf{n} &= \mathbf{t}_1 \times \mathbf{t}_2 \\ \mathbf{e}_1 &= \mathbf{t}_1 \\ \mathbf{e}_2 &= \mathbf{n} \times \mathbf{t}_1\end{aligned}\quad (2.18)$$

The potential gradient in the orthogonal coordinate system is computed as:

$$\begin{aligned}\frac{\partial \phi}{\partial \mathbf{e}_2} &= \frac{\frac{\partial \phi}{\partial s_2} - (\mathbf{t}_2 \cdot \mathbf{e}_1) \frac{\partial \phi}{\partial s_1}}{(\mathbf{t}_2 \cdot \mathbf{e}_2)} \\ \frac{\partial \phi}{\partial \mathbf{e}_1} &= \frac{\partial \phi}{\partial s_1}\end{aligned}\quad (2.19)$$

The total potential gradient in directions  $(\mathbf{e}_1, \mathbf{e}_2, \mathbf{n})$  are given as:

$$\begin{aligned}\frac{\partial \Phi}{\partial \mathbf{e}_1} &= \frac{\partial \phi}{\partial \mathbf{e}_1} + (\mathbf{v}_s \mathbf{v}_w + \boldsymbol{\theta} \times \mathbf{x}) \cdot \mathbf{e}_1 \\ \frac{\partial \Phi}{\partial \mathbf{e}_2} &= \frac{\partial \phi}{\partial \mathbf{e}_2} + (\mathbf{v}_s \mathbf{v}_w + \boldsymbol{\theta} \times \mathbf{x}) \cdot \mathbf{e}_2 \\ \frac{\partial \Phi}{\partial \mathbf{n}} &= \sigma + (\mathbf{v}_s \mathbf{v}_w + \boldsymbol{\theta} \times \mathbf{x}) \cdot \mathbf{n}\end{aligned}\quad (2.20)$$

Then in the non-rotating coordinate system the velocity vector  $\mathbf{V}$  is defined as:

$$\mathbf{V} = \frac{\partial \Phi}{\partial \mathbf{e}_1} \mathbf{e}_1 + \frac{\partial \Phi}{\partial \mathbf{e}_2} \mathbf{e}_2 + \frac{\partial \Phi}{\partial \mathbf{n}} \mathbf{n}\quad (2.21)$$

For an unsteady flow, the following second order scheme is used to derive a time derivative of the potential:

$$\frac{\partial \phi(t)}{\partial t} = \frac{3\phi(t) - 4\phi(t-1) + \phi(t-2)}{2\Delta t}\quad (2.22)$$

With the time- and spatial derivatives known, an expression is derived for the pressure coefficient  $C_p$  and dynamic pressure coefficient  $C_{pn}$ :

$$C_p = 1 - \frac{|\mathbf{V}|^2}{|\mathbf{v}_{\infty, x}|^2} - 2 \frac{\frac{\partial \phi}{\partial t}}{|\mathbf{v}_{\infty, x}|^2}\quad (2.23)$$

$$C_{pn} = 1 - \frac{|\mathbf{V}|^2}{(nD)^2} - 2 \frac{\frac{\partial \phi}{\partial t}}{(nD)^2} - 2 \frac{gz}{(nD)^2}\quad (2.24)$$

**Forces & Moments** The forces and moments are obtained using the pressure coefficients and the viscous shear stresses. The latter are approximated by applying skin friction coefficients determined with formulations of Blasius in the laminar regime, Brad-Aucher in turbulent regime and Prandtl-Schlichting to include the propeller roughness. These formulations are the following:

$$\begin{aligned} \text{Laminar: } C_f &= \frac{1.328}{\sqrt{\text{Re}}} \\ \text{Turbulent: } C_f &= \frac{0.044}{\text{Re}^{1/6}} - 5.0 \frac{1}{\text{Re}^{2/3}} \\ \text{Roughness: } C_f &= \frac{1}{\left(1.89 + 1.62 \log\left(\frac{\text{chord}}{K_p}\right)\right)^{2.5}} \end{aligned} \quad (2.25)$$

where the Reynolds number (Re) can be determined either using the arc, or the chord length of the propeller blade.  $K_p$  is the roughness parameter. Now the force  $\mathbf{F}$  and moment  $\mathbf{M}$  vectors can be determined with the following relations:

$$\begin{aligned} \mathbf{F} &= \sum_{i=1}^{N_i} \sum_{j=1}^{N_j} \left[ \frac{1}{2} \rho (nD)^2 C_p n_{ij} \mathbf{n}_{ij} + \frac{1}{2} \rho C_{f,ij} |\mathbf{v}_{i,j}| \mathbf{v}_{i,j} \right] A_{ij} \\ \mathbf{M} &= \sum_{i=1}^{N_i} \sum_{j=1}^{N_j} \left[ \frac{1}{2} \rho (nD)^2 C_p n_{ij} (\mathbf{x}_{ij} \times \mathbf{n}_{ij}) + \frac{1}{2} \rho C_{f,ij} |\mathbf{v}_{i,j}| (\mathbf{x}_{ij} \times \mathbf{v}_{i,j}) \right] A_{ij} \end{aligned} \quad (2.26)$$

where  $i$  and  $j$  are the panel indices,  $\mathbf{n}_{ij}$  is the normal component,  $\mathbf{v}_{ij}$  the local velocity component,  $\mathbf{x}_{ij}$  the location of the panel center and  $A_{ij}$  the panel area.

### 2.2.3. Iterative Pressure Kutta Condition

The Kutta condition is a principle in fluid dynamics which applies to solid bodies with a sharp trailing edge, such as the cross sectional profile of propeller blades. The condition states that the this body creates a circulation about itself to create the rear stagnation point at the trailing edge. Figure 2.2 displays the scenario when the Kutta condition is met, and when it is not. In order to have the stagnation point at the trailing edge, the flow along the pressure side and the suction side have to be parallel near the trailing edge. This can only be the case when there is a zero pressure gradient, as described earlier in equation (2.9). Applying the Kutta boundary condition at the trailing edge, enables the calculation of the fluid-dynamic lift produced by a wing in potential flow [21].

To suffice the zero pressure gradient boundary condition at the trailing edge (gradient in the direction perpendicular to the wake sheet, eq. (2.9)), as a result of the Kutta condition, PROCAL applies the Iterative Pressure Kutta Condition (IPKC). In this iterative procedure, the dipole strengths are being adjusted such, that the pressure difference reduces until it is below a specified tolerance. The following condition needs to apply:

$$\Delta C p_{jb}(\phi_{jw}) = 0 \quad (2.27)$$

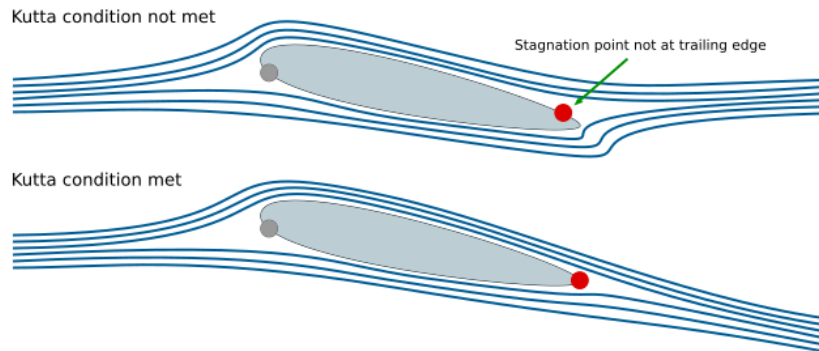


Figure 2.2: Illustration of the kutta condition (figure obtained from [24])

where  $j_b$  and  $j_w$  denote the panel index in  $j$ -direction (see figure 2.1) for the body and wake surface respectively. In a steady flow computation the wake dipole strength of all panels in streamwise direction is updated, whereas in unsteady flow it is only updated for the first panel. The equation above is non-linear and, to solve it, a Newton-Raphson iteration is applied:

$$\boldsymbol{\phi}_w^{k+1} = \boldsymbol{\phi}_w^k + \delta\boldsymbol{\phi}_w^k = \boldsymbol{\phi}_w^k - \bar{\mathbf{J}}^{-1} \Delta\mathbf{Cp}^k \quad (2.28)$$

with  $k$  denoting the iteration number,  $\delta$  the change of the variable and  $\bar{\mathbf{J}}$  the Jacobian, defined as:

$$\mathbf{J}_{i,j} = \frac{\delta(\Delta C p_i)}{\delta\boldsymbol{\phi}_{w,j}} \quad (2.29)$$

The Jacobian is computed by determining the perturbation wake strength of panel  $j$  with  $\delta\boldsymbol{\phi}_j$ :

$$\delta\boldsymbol{\phi}_{w,j} = \varepsilon_{jac}\boldsymbol{\phi}_{w,j} \quad (2.30)$$

Where  $\varepsilon_{jac}$  is a control variable which can be specified by the user (typically  $\varepsilon_{jac} = 0.001$ ). Then, the change in dipole strength on the body and subsequently the pressure difference at the  $i$  index of the trailing edge panels can be determined. The influence of a difference in wake strength on the blade potentials can be computed as it yields a linear system of equations. This system of equations is given as:

$$\begin{aligned} \mathbf{D}\delta\boldsymbol{\phi}_b + \mathbf{W}\delta\boldsymbol{\phi}_w &= 0 \Leftrightarrow \\ \delta\boldsymbol{\phi}_b &= -\mathbf{D}^{-1}\mathbf{W}\delta\boldsymbol{\phi}_w \Leftrightarrow \\ \delta\boldsymbol{\phi}_b &= \mathbf{W}_{ipkc}\delta\boldsymbol{\phi}_w \end{aligned} \quad (2.31)$$

The matrix  $\mathbf{W}_{ipkc}$  is calculated once for every computation. It is computed separately for each key lifting surface independent of the other surfaces and symmetry surfaces.

#### 2.2.4. Input files

The main input for PROCAL comes from one control file (.ctr) where all available options for physical parameters, modeling settings, operating conditions and output properties can be specified. The control file calls for other specified input files listed below:

- Surface panel files (.pan): Define the Cartesian coordinates of the panel distributions of the analyzed geometry surface.
- Ship wake file (.wak): When the velocity distribution is non uniform across the propeller disk, it is contained in this file. (optional)
- Field point file (.fld): Defines the location of points at which propeller-induced flow solutions will be evaluated. (optional)
- Solid boundary factor file (.sbf): Defines solid boundary factors when PROCAL is applied for hull pressure calculations. (optional)

While the optional input files for the ship wake, field points and solid boundary factors must be generated externally, the mandatory control and surface panel files can be generated with the PROCAL VISualisation Environment (ProVise) [3]. ProVise was developed to facilitate the generation of PROCAL input files, as well as to monitor runs and display results of flow solutions. In the case of propeller flow simulation where a panel file should be generated, ProVise requires input from a propeller geometry file (.ppg), which contains the geometrical parameters for propeller blade sections lying on cylindrical surfaces at a discrete set of constant radial stations. Besides the blade parameters, the hub geometry can be defined as well in case of a non-constant hub geometry. Here the hub radius is defined at different axial positions.

### 2.2.5. Limitations

Since BEM solvers are based on potential flow theory, the assumptions on which they are based may limit the reliability of the results. For potential flow theory to be valid, the flow is assumed to be irrotational. In an irrotational flow, the curl of the velocity field is always zero. As a result, in regions where vorticity is important, e.g. boundary layers, potential flow theory is unable to provide accurate computations. In case of high Reynolds numbers (say  $Re > 10^5$ ) when the flow is fully turbulent, the thickness of the boundary layer can be neglected. However, at lower Reynolds numbers the BEM may not be able to provide reasonable predictions of the flow. Another limitation to potential flow is that it does not account for viscosity. Though in different magnitudes, any liquid has viscosity, the question is whether it is insignificant enough to be neglected. With marine propellers this is not always the case, hence a correction is applied in PROCAL. However, this does increase the uncertainty of the solution since use is made of empiric relations such as shown in equation (2.25). A study has been performed in [20] to validate the BEM method against Computational Fluid Dynamics (CFD) methods and experimental results. The applied CFD method was a Reynolds Averaged Navier Stokes (RANS) solver, where viscosity is considered. Results have shown that the BEM method yields feasible results for intermediate advance ratios [20]. The loss of accuracy at high advance coefficients may be explained by the increasingly dominant viscous forces, for which empiric adjustments are applied in PROCAL. For lower advance ratios, inaccuracies may occur due to stronger leading edge vortex separation, which is not captured by BEM software.

### 2.3. Finite Element Method

The finite element method is applied to solve numerous engineering problems, such as structural analyses, heat transfer, and fluid dynamics. To solve a problem, the FEM subdivides a large system into smaller parts (finite elements). The FEM software TRIDENT/VAST is applied for the structural analysis. It was developed by Lloyd's Register - Martec for the modeling and analysis of marine applications, among which marine propellers. The main working principle of the FEM analysis is as follows [7]:

- Discretization of the continuum, i.e. division of the control volume into a mesh of e.g. beam or solid elements. The mesh is described with several arrays consisting of nodal coordinates and element connectivities.
- Interpolation across the field variables of the element (shape functions).
- Finding the element properties. The matrix equation for the finite elements should be established relating the nodal values to other parameters.
- Assemble the element equations which are required to find the global equation system for the domain, i.e. combining the local element equations for all elements and use their connectivities for the assembly. To find a solution, boundary conditions have to be imposed.
- Solve the global equation system. Direct and iterative methods can be used as a solution to find the nodal values.

For a propeller analysis, the hub is considered as a non-deformable body, hence only the blade is modeled. It should be noted that this assumption can influence the structural response since the root is now modeled as a fixed connection, whereas the real hub is a connection with a finite stiffness. This modeling choice still provides reasonable results since the hub and shaft have a significantly higher stiffness than the blade itself. However, a blade-hub or even a blade-hub-shaft model will provide more realistic results, especially for higher modes [26].

Trident has the capability to automatically generate a solid finite element model with a user specified grid and the geometric model of the blade which PROCAL uses as well. Figure 2.3 displays a FE mesh for a propeller blade generated by Trident, with the boundary condition that the root is completely fixed. The analysis tool (P)VAST (Propeller Vibration and Strength Analysis Tool) can perform a static, dynamic and an eigenvalue analysis. A static analysis can be performed in a situation where the loads are constant in time, i.e. uniform flow conditions. When loading conditions are time dependent, an eigenvalue analysis is performed prior to the dynamic analysis. The static and dynamic solvers are further discussed in the following two sections.

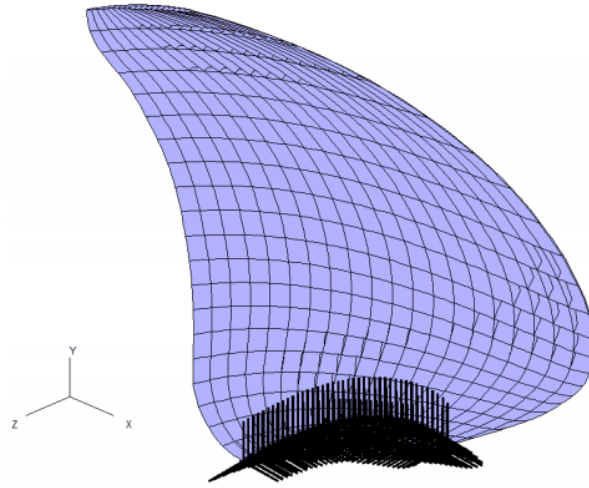


Figure 2.3: Mesh generated by VAST with fixed root (figure obtained from [26])

### 2.3.1. Static analysis

In the case of a steady analysis, a static, geometrically non-linear analysis is performed by VAST. It solves the governing static equations, which are:

$$\mathbf{K}\{\mathbf{u}\} = \{\mathbf{f}\} \quad (2.32)$$

Here  $\mathbf{K}$  denotes the coupled stiffness matrix,  $\mathbf{u}$  the displacement vector and  $\mathbf{f}$  the applied load vector. The equations are solved for the displacements by means of Lower-Upper (LU) decomposition, which ultimately is used to calculate internal stresses. VAST can process pressure input per element, and has the ability to include centrifugal forces as a result of the rotational velocities and accelerations.

### 2.3.2. Dynamic Analysis

For the dynamic analysis, it is assumed that the structure behaves geometrically linear. That is, non-linear effects, e.g. buckling are neglected, and calculated loads are always applied to the non-deformed structure. Geometric linearity imposes limitations to the relative magnitude of deformations. However, the benefit of assuming geometric linearity is that it enables the use of a modal analysis, where the modal shape functions need to be determined only once, prior to the unsteady analysis. The discretized equations of motion in FEM are:

$$\mathbf{M}\{\ddot{\mathbf{u}}\}(t) + \mathbf{C}\{\dot{\mathbf{u}}\}(t) + \mathbf{K}\{\mathbf{u}\}(t) = \{\mathbf{f}\}(t) \quad (2.33)$$

Here  $\mathbf{M}$  denotes mass,  $\mathbf{K}$  stiffness and  $\mathbf{C}$  damping, in matrix form. The vectors  $\mathbf{u}$  and  $\mathbf{f}$  denote the node displacements and forces respectively for each degree of freedom, both as a function of time,  $t$ . To obtain the natural frequencies of this system of equations, the damping matrix and load vector can be set to zero, yielding the eigenvalue problem:

$$\mathbf{M}\{\ddot{\mathbf{u}}\}(t) + \mathbf{K}\{\mathbf{u}\}(t) = 0 \quad (2.34)$$

Since the free vibration solution has to be found, the displacement can be written as a harmonic function with amplitude  $\hat{\mathbf{u}}$ :

$$\begin{aligned} \mathbf{u} &= \{\hat{\mathbf{u}}\} \cos(\omega t) \\ \ddot{\mathbf{u}} &= -\omega^2 \cdot \{\hat{\mathbf{u}}\} \cos(\omega t) \end{aligned} \quad (2.35)$$

Substitution of equation (2.35) into (2.34) yields;

$$(\mathbf{K} - \omega^2 \mathbf{M})\{\hat{\mathbf{u}}\} = 0 \quad (2.36)$$

Solving this eigenvalue problem yields the eigenvectors along with their corresponding natural frequencies. The non trivial eigenvectors describe the mode shapes. With this the system modes  $\hat{\mathbf{u}}_i$  can be described,

where  $i = 1 \dots m$  with  $m$  as the number of mode shapes. The mode shape matrix  $\Psi$  is constructed as:

$$\Psi = [\{\hat{\mathbf{u}}\}_1, \{\hat{\mathbf{u}}\}_2, \dots, \{\hat{\mathbf{u}}\}_m] \quad (2.37)$$

This is the space dependent part of the solution, now the periodic part remains to be determined, since the displacement can be described with a spatial and periodic part:

$$\{\mathbf{u}\}(t) = \sum_{i=1}^m \hat{\mathbf{u}}_i \{q\}_i(t) = \Psi \{q\}(t) \quad (2.38)$$

where  $q$  denotes the modal scale vector consisting of the temporal variations and scaling factors (also known as participation factors). This equation is then substituted into equations (2.33), and pre-multiplied by  $\Psi^T$  to yield:

$$\mathbf{M}_m \{\ddot{q}\}(t) + \mathbf{C}_m \{\dot{q}\}(t) + \mathbf{K}_m \{q\}(t) = \Psi^T \{f\}(t) \quad (2.39)$$

where  $\mathbf{M}_m$ ,  $\mathbf{C}_m$ ,  $\mathbf{K}_m$  and  $\mathbf{f}_m$  are now in modal form. Due to the orthogonality properties of  $\Psi$ , the modal mass and stiffness are diagonal matrixes ( $m \times m$ ) which can be scaled, to yield  $\mathbf{M}_m = \mathbf{I}$  and  $\mathbf{K}_m = \Omega$  diagonal with  $\omega_i^2$ . In case of modal of proportional damping, i.e. when  $\mathbf{C}_m$  is a diagonal matrix, it can be scaled to diagonal matrix  $\mathbf{Z}$ . This leads to a decoupled system, where the modal participation factors can be solved independently:

$$\mathbf{I}\{\ddot{q}\}(t) + \mathbf{Z}\{\dot{q}\}(t) + \Omega\{q\}(t) = \Psi^T \{f\}(t) \quad (2.40)$$

For the case of a marine propeller, equation (2.33) transforms to the structural dynamic equation:

$$[\mathbf{M}] \{\ddot{\mathbf{u}}\} + [\mathbf{C}] \{\dot{\mathbf{u}}\} + [\mathbf{K}] \{\mathbf{u}\} = \{\mathbf{f}_h\} + \{\mathbf{f}_{fict}\} \quad (2.41)$$

Where the force is divided into a hydrodynamic part ( $\mathbf{f}_h$ ) which includes the added mass, hydrodynamic damping and restoring stiffness, and a fictitious part ( $\mathbf{f}_{fict}$ ). The fictitious part represents the forces due to the propeller rotation, it is the sum of centrifugal, and Coriolis forces:

$$\{\mathbf{f}_{fict}\}(t) = \{\mathbf{f}_{centrifugal}\}(t) + \{\mathbf{f}_{Coriolis}\}(t) \quad (2.42)$$

The centrifugal force is described as:

$$\mathbf{f}_{centrifugal} = \mathbf{f}_c = m(\dot{\boldsymbol{\theta}} \times (\dot{\boldsymbol{\theta}} \times \mathbf{x}(t))) = m(2\pi n)^2 \mathbf{r}(t) \quad (2.43)$$

$\mathbf{r}$  denotes the radial projection of the position vector at the propeller plane. The Coriolis force is:

$$\mathbf{f}_{Coriolis} = 2m \left( \dot{\boldsymbol{\theta}} \times \frac{d\mathbf{x}(t)}{dt} \right) \quad (2.44)$$

This causes some additional damping, which is negligible compared to the hydrodynamic damping, and is therefore left out of the equation of motion. Using modal analysis, substitution into equation (2.40) yields a system of equations for the dry modes:

$$\mathbf{I}\{\ddot{q}\}(t) + \mathbf{Z}\{\dot{q}\}(t) + \Omega\{q\}(t) = \Psi^T \{f_h + f_c\}(t) \quad (2.45)$$

One can also take the added mass, hydrodynamic damping and restoring stiffness into account to determine the wet mode shapes. In this case the fluid added mass and hydrodynamic damping should be removed from the right hand side. This yields a new hydrodynamic force vector which is denoted  $\mathbf{f}_h^*$ . This way, equation (2.41) transforms into:

$$(\mathbf{M} + \mathbf{M}_a)\{\ddot{u}\}(t) + (\mathbf{C} + \mathbf{C}_a)\{\dot{u}\}(t) + \mathbf{K}\{u\}(t) = \{\mathbf{f}_h^* + \mathbf{f}_c\}(t) \quad (2.46)$$

This can be rewritten to the wet form of equation (2.45):

$$\mathbf{I}\{\ddot{q}\}(t) + \tilde{\mathbf{Z}}\{\dot{q}\}(t) + \tilde{\Omega}\{q\}(t) = \tilde{\Psi}^T \{\mathbf{f}_h^* + \mathbf{f}_c\}(t) \quad (2.47)$$

Even though computation of the wet mode shapes is a more complete approach, it has the disadvantage that it requires approximations for the added mass and hydrodynamic damping components. This can be done by TRIDENT/VAST, but since PROCAL captures the blade velocity and acceleration effects, the choice was made to include these in the right hand side of the equation, thus using dry modes instead.

### 2.3.3. Input files

In order to perform an structural analysis, TRIDENT requires a number of input files, as are listed below:

- Meshing instructions file (.cdr): Contains the instructions for the mesh, i.e. the number of finite elements (chord/span) and local grid refinements. Furthermore, it contains information about the type of elements applied and material properties: the elasticity modulus, Poisson's ratio and mass density. Lastly, it describes the load type (pressure details) and options for load conversion to the FEM grid.
- Propeller geometry file (.ppg): Contains the geometrical parameters of the propeller blade sections at different radial positions. This is the same basic propeller geometry input as used by PROCAL.
- Material properties (.prp): In the case of an anisotropic material, this file contains the material properties. It contains information regarding the orientation of the laminate structure of composites.

These files are then used to generate the input for VAST, listed here:

- Solution control parameters (.use): These parameters are required for controlling the VAST execution in non-linear analyses, which are applied in the case of a steady FSI computation (section 2.5). These define a solution strategy, load steps (incrementally increasing the deformation with a percentage of the full load to avoid divergence) and a convergence criterion.
- FEM model (.gom) Contains the finite element model based on the geometry of the propeller, including nodal co-ordinates, element connectivity information and material properties. This file is generated with the .ppg file and the .cdr file.
- Boundary conditions (.smd): Contains the fixed root boundary conditions, assumed constant at all times.
- Pressure information (.lod): Contains the pressures obtained from the last hydrodynamic analysis (PROCAL) converted into loads.

## 2.4. Adaptations to BEM and FEM software

### 2.4.1. Adaptations to PROCAL

For the unsteady FSI application of PROCAL adaptations are required to the standard software package. A DLL version of PROCAL has been made, with the important difference of including the vibrations of the blade, and conserving the generated data structure (revs, time steps, panel normal vectors, vibration velocities), such that it can be used in subsequent calculation steps. The applied scripts within the ComPropApp C# environment were made for four types of computations:

- Type 1: Steady analysis, in this case the steady FSI solver in ComPropApp can be applied, for this no adaptations to PROCAL are required.
- Type 2: Either the undeformed propeller geometry or the geometry obtained from a steady analysis is input for an unsteady PROCAL analysis, without altering the geometry any further. The results of this functions as a starting point for type 3 computations.
- Type 3: Propeller deformations are included in the unsteady analysis by updating the panel/wake geometry and the hydrodynamic influence coefficients per time step. Therefore the equation of motion (eq: (2.41)) is constant at the left-hand-side and the right-hand-side changes for each time step. The computation consists of three parts; initialization (1<sup>st</sup> time- and revolution step), the main part (subsequent steps until 2<sup>nd</sup> to last time step), and the end part (last time step). In the last step the data is written to the output files.
- The type 4 computations have the same working principle as type 3, but now the hydrodynamic influence coefficients at the left-hand-side of the equation of motion are recomputed for each time step with the type 3 computations as starting point. This is computationally more demanding, although the results of the type 3 equations should be close to the final output, therefore rapid convergence is expected. This type of computation is not included in the current version of ComPropApp (1.0.2.3), but may be included in a future version.

Another adaptation required in the FSI application, is the time derivative of the velocity potential in PROCAL. When deformations are included in the BEM computations, the accelerations need to be considered by applying the material derivative. Equation 2.22 is no longer valid, the new formulation becomes:

$$\frac{\partial \Phi'}{\partial t} = \frac{D\Phi}{Dt} - \mathbf{V}_g \cdot \nabla \Phi = \frac{\partial \Phi}{\partial t} + (\mathbf{V} - \mathbf{V}_g) \cdot \nabla \Phi \quad (2.48)$$

Here  $\mathbf{V}_g$  denotes the vibration velocity vector, obtained with the FEM computation. The material derivative can be calculated with the time gradient of the potential using a high order finite difference method.

#### 2.4.2. PROCAL to TRIDENT/VAST conversion

When PROCAL has performed a steady FSI iteration it generates a load output file, which gets processed by the program Extproptec to write it as separate loads per radial position corresponding to the radial positions described in the propeller geometry file. For an unsteady FSI computation, the panel center pressures are converted to nodal forces, corresponding to the nodes in the structural mesh. Since the finite element mesh is built up differently than the panel mesh, load values applying on structural nodes have to be interpolated. In both the steady and unsteady FSI, these forces need to be transformed to a readable format for VAST. This is required since VAST uses a different coordinate system, as is shown in table 2.1. Once the VAST displacement values have been determined, they are transformed back to the PROCAL coordinate system, such that it can perform a new iteration with the deformed geometry.

	PROCAL [m]	VAST [mm]
Upstream	$x$	$-z$
Portside	$y$	$-x$
Upwards	$z$	$y$

Table 2.1: PROCAL-VAST coordinate transformation

#### 2.4.3. TRIDENT/VAST

To make TRIDENT/VAST applicable within the ComPropApp, the main adaptations required is the ability to run in batch mode. This is mainly due to the iterative nature of the ComPropApp, hence it should be possible to provide the software instructions only with command files, bypassing a series of menus. These command files have the extension (.clf) and are constructed by ComPropApp, dependent on the selected procedure. Another implementation in the steady FSI procedure in ComPropApp is a special load generation algorithm, which is active in VAST. Here the set of pressure loads from the previous iteration is applied to the geometry, after which the pressure gradually increases to the current pressure. For each restart of VAST, the starting and ending load steps are adjusted by the ComPropApp.

## 2.5. Steady FSI Analysis

In the steady analysis, the geometry behavior is assumed as non-linear, the benefit of this assumption is that there are fewer limitations on the deformation magnitudes. If the entire structural load would be applied immediately, divergence problems could occur in the FEM analysis. Therefore PROCAL computes the loads by increasing the revolutions and stream velocity incrementally, such that the advance velocity remains constant to keep the loading distribution similar. For each of the load steps, TRIDENT/VAST computes the deformed load shape, which is then used as a basis for the new panel file for the next load increment. For the steady analysis, TRIDENT/VAST can treat the fairing of deformed blade geometries to perform updates on the PROCAL panel file. TRIDENT/VAST works on an incremental basis as well for a FEM analysis, the difference between both methods being that PROCAL uses a constant geometry whilst adjusting the load at each (iteration) step, and VAST incrementally increases the percentage of a constant load, to gradually increase deformation, which all occurs within one ComPropApp iteration. This entire process repeats itself until the full load is applied. The number of load increments and the maximum number of iterations to reach convergence can be specified in the GUI of ComPropApp. The maximum number of iterations is always equal or greater than the number of load increments, since the difference between them defines the number of iterations at full load. These iterations at constant maximum load are performed until convergence is reached between thrust and blade deformation. After the last iteration, a new propeller geometry file is generated by TRIDENT. It is possible to use this geometry file for more detailed flow analyses, for instance, cavitation calculations or to verify the load convergence.

In the ComPropApp versions prior to 1.0.1, used in the initial part of the verification study, the steady procedure is as follows: TRIDENT and VAST are run through command line batch files which are written by the ComPropApp. Throughout the steady analysis, there are four files; Trident1.clf, Trident2.clf, Trident3.clf, and Trident4.clf. After completion of the first TRIDENT session (Trident1.clf), VAST is executed with the initial blade geometry. Next, the panel file is updated with the new deformations, which occurs in a separate TRIDENT session (Trident2.clf). After that, PROCAL performs another run and the resulting loads are used to generate new pressure files, solution control files, and another TRIDENT session (Trident3.clf). With these new parameters, VAST is executed again, the panel file gets updated, the second TRIDENT session is overwritten and after another PROCAL run, the third TRIDENT session is obtained again. This process repeats itself until the convergence criterion is met. At that point, the propeller geometry file and panel file are updated in the fourth TRIDENT session (Trident4.clf).

In the ComPropApp versions above 1.0.2, the procedure has undergone a number of changes: Trident2.clf and Trident4.clf have been replaced with Propart4Comprop (P4C), a propart toolbox which is capable of generating the new panel files with the deformed FE structure.

## 2.6. Unsteady FSI Analysis

In the unsteady FSI analysis of ComPropApp a modal analysis is performed, of which the methodology is explained in this section. In the analysis a geometrically linear finite element procedure is applied. This is an assumption to which there are certain limitations, as listed below:

- Materials are required to abide Hooke's law, which is the case in the elastic regime in which a propeller should operate.
- Loads are applied to the undeformed structure to determine deformation, hence the magnitude of deformation is limited. That said, since the loads are actually pressures, they always apply in the normal direction to the surface.
- Geometrically non-linear behavior cannot be modeled with linear beam elements, e.g. buckling effects as an effect of radial loads.

### 2.6.1. Frequency domain solution

The FSI solution is of a periodic nature, creating the possibility to perform computations in the frequency domain, which should lead to faster convergence of the steady state solution than time integration. The reason being that the equations of motion can be solved in the frequency domain, hence transients which negatively affect convergence behavior are not computed. The periodic coupling method is recommended for the BEM-FEM coupling in non-uniform conditions, due to the periodic nature of the BEM solution. A time-step coupling approach will require more computational time to solve. Since the solutions must be periodic on a propeller revolution basis, the force vector in the equation of motion can be determined at the same blade position taken at the previous revolution. The ComPropApp uses dry mode shapes, such that the added mass and hydrodynamic damping components are obtained from PROCAL and added to the right hand side of the equation of motion, i.e. equation (2.45) is applied in this case. In the frequency domain, equation (2.45) transforms into:

$$\mathbf{I}\{\ddot{q}\}^k + \mathbf{Z}\{\dot{q}\}^k + \mathbf{\Omega}\{q\}^k = \Psi^T \{\mathbf{f}_{total}\}^{k-1} \quad (2.49)$$

Here  $k$  denotes the revolution index. Rather than time steps, the revolution consists of a number of blade positions,  $M$ . For a full revolution, a set of  $M$  modal force vectors needs to be determined. Applying the forward Fourier transform yields a series of modal force vectors in frequency domain, which are defined as:

$$\{\mathbf{F}_m\} = \sum_{l=0}^{M-1} \Psi^T \{\mathbf{f}_l\} e^{-i\theta l \Delta t} \quad (2.50)$$

where  $\theta$  denotes the angular shaft velocity ( $2\pi n$ ),  $l$  the blade position index ( $l = 1, 2, \dots, M-1$ ) and  $\Delta t$  the time step. For the modal participation factors the following applies:

$$\{q_l\} = \sum_{l=0}^{M-1} \{Q_l\} e^{i\theta l \Delta t} \quad (2.51)$$

$$\{\dot{q}_l\} = \sum_{l=0}^{M-1} \{i\theta l \cdot Q_l\} e^{i\theta l \Delta t} \quad (2.52)$$

$$\{\ddot{q}_l\} = \sum_{l=0}^{M-1} \{-(\theta l)^2 \cdot Q_l\} e^{i\theta l \Delta t} \quad (2.53)$$

With the equations above, equation (2.49) can be transformed to the frequency domain to yield an expression where the modal participation factors can be solved:

$$\{Q_m\}^k = [-(\theta l)^2 \mathbf{I} + i\theta l \mathbf{Z} + \mathbf{\Omega}]^{-1} \{\mathbf{F}_m\}^{k-1} \quad (2.54)$$

The solution for the nodal deformation in the time domain, becomes:

$$\mathbf{u}_l^k = \Psi \{q_l\}^k \quad (2.55)$$

### 2.6.2. Coupling Iteration Methods

Since the structural and hydrodynamic equations are solved separately in the partitioned approach, inaccuracies and divergence problems may occur. This is especially the case when the interaction when the interaction between flow and propeller is strong, i.e. when the fluid added mass becomes relatively large compared to the structural mass. In order to overcome these problems, so called coupling iterations are applied when values for the next time (or rather blade position) step have been computed. The working principle of coupling iterations is to utilize values obtained in the previous timestep(s), to predict the current timestep. Coupling iteration methods can be performed in several techniques, the most commonly applied are discussed here, viz. Aitken relaxation and a Newton iteration method. When  $\{\mathbf{f}_h\}$  denotes the structural hydrodynamic load at the fluid-structure interface, this can be expressed with fluid operator  $F$  as a function of the displacements:

$$\{\mathbf{f}_h\} = \mathbf{F}(\{\mathbf{u}\}) \quad (2.56)$$

Now a fluid grid needs to be deformed based on the deformed positions of the propeller blade. The fluid equations of motion are solved to obtain the hydrodynamic load on the fluid-structure interface. The propeller panel file is updated, after which a PROCAL computation is performed, yielding the surface pressure distribution on the deformed propeller blade. Now, a structure operator defined as  $S$  applies the hydrodynamic forces on the deformed structure returning an update of the structural response vector at the interface:

$$\{\mathbf{u}\} = \mathbf{S}(\{\mathbf{f}_h\}) \quad (2.57)$$

In theory substitution of the hydrodynamic load obtained from (2.56) into the structure operator should result in the exact same displacement vector  $\{\mathbf{u}\}$ . However, due to the partitioned method it is not the case and some residual  $\mathbf{R}$  remains:

$$\mathbf{R} = \mathbf{S}[F(\{\mathbf{u}\})] - \{\mathbf{u}\} \quad (2.58)$$

In discretized form, applying Newton-Raphson the following equation is obtained:

$$\{\mathbf{u}\}_{k+1} = \{\mathbf{u}\}_k - \mathbf{J}_k^{-1} R(\{\mathbf{u}\}_k) \quad (2.59)$$

Here  $\mathbf{J}^{-1}$  represents the inverse of the Jacobian which is unknown, but can be approximated using Quasi-Newton solution methods. In ComPropApp, the Quasi-Newton iterative least squares (QN-ILS) approach is used. These methods are required since there is no access to the Jacobian since the coupling occurs with black box systems, which makes differentiation virtually impossible [10]. With QN-ILS the inverse Jacobian is determined implicitly in the new update of interface structural response. The approximation of the new response at the interface is as follows:

$$\{\tilde{\mathbf{u}}\}_{k+1} = \{\mathbf{u}\}_k + \sum_{i=0}^{k-1} \{\alpha_k\}_i \cdot (\{\mathbf{u}\}_i - \{\mathbf{u}\}_k) \quad (2.60)$$

where  $\{\tilde{\mathbf{u}}\}_{k+1}$  represents the predicted structural response at the next time step.  $\alpha_k$  is a vector at iteration  $k$  for which the coefficients are found using a least squares minimization of the approximated residual:

$$\alpha_k = \arg \min \left\| \left\| R(\{\mathbf{u}\}_k) + \sum_{i=0}^{k-1} \{\alpha_k\}_i \cdot \left( R(\{\mathbf{u}\}_i) - R(\{\mathbf{u}\}_k) \right) \right\| \right\| \quad (2.61)$$

The method takes the best linear combination of all previous estimates of the residuals. Equations (2.60) and (2.61) are applied in the ComPropApp only after a few iterations, due to initialization problems of this since it requires information of previous iterations of  $\mathbf{u}$ . To overcome this, Aitken's method is applied at the first two iterations. In Aitken's method, the inverse Jacobian is approximated as  $\mathbf{J}^{-1} = -\alpha_k \cdot \mathbf{I}$ , where relaxation coefficient  $\alpha_k$  is now a scalar between 0 and 1 for each iteration  $k$ . Predicted and computed interface response for two coupling iterations ( $\{\tilde{\mathbf{u}}_{k-1}, \mathbf{u}_{k-1}\}$ ) and ( $\{\tilde{\mathbf{u}}_k, \mathbf{u}_k\}$ ) are required to estimate them for the next iteration.

$$\{\tilde{\mathbf{u}}\}_{k+1} = \{\tilde{\mathbf{u}}\}_k + \alpha_k (\{\mathbf{u}\}_k - \{\tilde{\mathbf{u}}\}_k) \quad (2.62)$$

### 2.6.3. Coupling procedure

This section describes the procedure followed by the ComPropApp throughout an unsteady FSI analysis. An explanation is listed below.

1. The unsteady analysis starts its first iteration with PROCAL, solving the pressure distribution on the blades using the undeformed propeller geometry. PROCAL computes several revolutions until thrust has converged and a steady state solution for the loads is obtained. This problem is solved iteratively, where the convergence is checked after each propeller revolution. The obtained pressure distribution is written in the \*pressure.dat file for each angular step in one revolution.
2. With the pressure distribution obtained from PROCAL and results from the modal analysis, the blade vibrations are computed per angular blade step. This is done by transforming the pressure coefficients at PROCAL corner points to nodal pressures on the FE grid. Then, the nodal pressures are transformed to nodal forces, along with the centrifugal load forces. These are subsequently converted to the forces in modal space. The time periodic coupling method is then applied, where the Fourier transform is used to transform the modal vectors into  $M$  modal force vectors in the frequency domain.
3. The applied load remains constant throughout the FEM analysis. Multiple revolutions may be required to reach quasi-steady blade deformations, meaning no further changes occur at a new revolution. Aitken relaxation is applied in the first two revolutions, after which (QN-ILS) method is applied for the remaining iterations. This is to prevent divergence problems, since QN-ILS requires data from a number of previous time steps. When the quasi-steady state is reached, the blade deformations, velocities and accelerations for all angular positions are stored.
4. The next step is turning the new deformed blade geometries, which differ per angular step, into a range of new panel files. This is performed by the PROPART toolbox [12]. With these new panel files, new PROCAL simulations are performed for each angular position separately. Note that the source strengths are redefined for each revolution step to account for the blade vibration velocities. The adapted version of PROCAL, which is explained in section 2.4.1, is applied in this case.
5. Steps 2 to 4 are repeated until the displacements have converged for all angular positions.

A schematic of the unsteady procedure is given in figure 2.4. Here  $k$  denotes the FSI iteration counter and  $r$  the revolution counter.  $M$  is the number of angular blade positions evaluated.

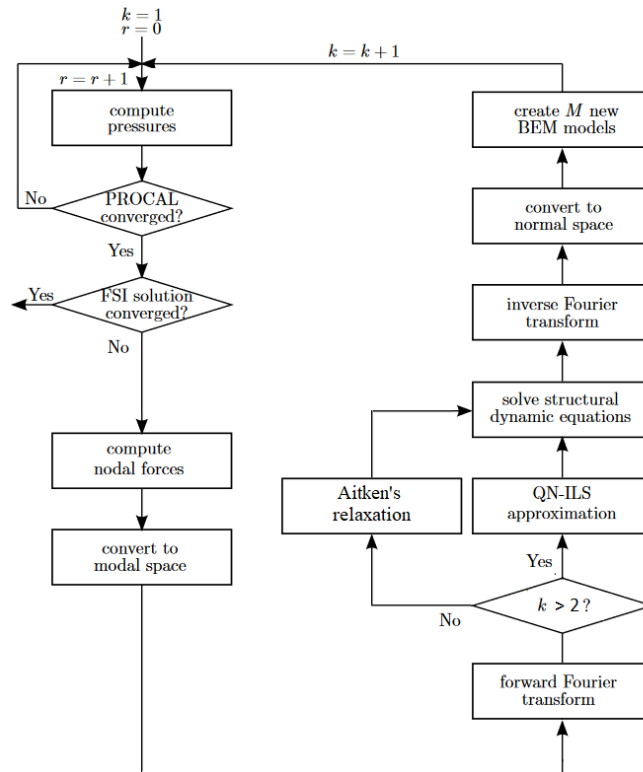


Figure 2.4: Unsteady FSI schematic (adapted from [20])

# 3

## Verification study

### 3.1. Introduction

The Wageningen C4 – 40 series has been manufactured at MARIN using the isotropic polyurethane material SikaBlock M700. It has a P/D value of 0.8. The propeller was shaped using a CNC milling machine. Figure 3.1 displays the model design. This propeller geometry is used to perform the verification study, which means a simulation model of this design will be constructed. A geometry file (.ppg) of the model was available and with it, the input files for ComPropApp can be set up. Prior to performing the verification study, a falsification study was applied for the steady and unsteady FSI modules. This to find where the theory fails and, where possible, to apply corrections in order to overcome this. The initial material that was used for the computations is epoxy. This because at the beginning of the verification study the measurements on the polyurethane were not performed yet. The datasheet in Appendix B.1 displays the properties given by the manufacturer, but measurements by the Defence Research Center of Canada (DRDC) have shown that these are approximations that differ from a sample taken from the material. The elasticity modulus of the sample is 20% lower than indicated by the manufacturer. As a final step in the verification process, simulations are also performed for the SikaBlock material, and a number of these simulations are used in the validation process afterwards.



Figure 3.1: C4-40 CAT Reduced D034,  $P/D_{0.7} = 0.8$  (figure obtained from [4])

## 3.2. Input files setup

### 3.2.1. PROCAL control parameters

The first step is the configuration of the PROCAL part, where the physical properties, operating conditions and control parameters need to be defined. This is done within the Prowise environment, applying the guidelines and theory found in the PROCAL theory manual and Prowise user guide [3, 13]. The physical properties are shown in table 3.1.

Parameter	Symbol	Value	Unit
Water density	$\rho_w$	998	$kg/m^3$
Kinematic viscosity	$\nu$	1.010E-06	$m^2/s$
Roughness	$k_p$	0	$m$
Ambient pressure	$p_\infty$	1025	$kPa$
Vapour pressure	$p_v$	1.7	$kPa$
Gravitational constant	$g$	9.81	$m/s^2$

Table 3.1: Physical properties of the simulation

Subsequently, a grid study was performed. This procedure is described in section 3.2.2. The defined grid simulations have been performed for different operational conditions, since the behavior of the propeller throughout different operating conditions are of interest. In section 3.2.3 an open water diagram is setup by running PROCAL at different advance ratios whilst keeping the shaft speed constant. Table 3.2 displays the operation conditions in the different situations.

Parameter	Symbol	Unit	OWD	Grid study
Free stream velocity	$V_0$	$m/s$	0.0 - 4.6	3.06
Advance ratio	J	[-]	0.0 - 0.9	0.6
Rotation speed	n	$rps$	15	15

Table 3.2: Operating conditions of the simulations

Further, the PROCAL control parameters are setup with PROWISE, and the guidelines given in its user guide [3]. The general parameters are shown in table 3.3, along with a short description.

Parameter	Value	Explanation
Number of revolutions	5	Number of blades + 1
Steps between blade	15	Revolution divided into 6° steps
Post processing revolutions	1	Revolutions written to output files
Farfield criterion	8	Defines when influence of a panel can be approximated (default)
Viscous scale factor	1	Used for froude scaling
Viscous mode	2	Reynolds number based on chord length at 0.7 · radius
$C_t$ min value	0	Minimal value for tangential force
<b>Kutta</b>		
Convergence criterion	0.01	Iterations stop when $\Delta C_p < \text{criterion}$
Number of steps	20	Maximum number of steps
Epsilon Jacobian	0.01	Relaxation factor (cf. section 2.2.3)
IPKC model	1	Consider lifting surfaces separately
<b>Wake alignment</b>		
Convergence criterion	0.01	Iterations stop when $\Delta \text{RMS}(\text{wake displacement}) < \text{criterion}$
Number of steps	15	Maximum number of steps
Relaxation	0.2	Relaxation parameter iterative wake alignment procedure
Alignment mode	1	Apply fully described wake model
Prescribed pitch	2	Smooth trailing edge flow and tip vortex pitch near tip
Prescribed contraction	2	Minimum contraction model

Table 3.3: General control parameters PROCAL (steady computation)

### 3.2.2. Panel grid construction

The panel grid has been set up using the propeller geometry file of the 'C4-40' propeller. PROCAL has certain guidelines to define the parameters listed below, and these are implemented into the model [8].

- Number of blade panels (chord/span): Explained in the paragraph below  $\rightarrow 30 \times 30$
- Tip chord fraction: Highest defined radius = 0.970  $\rightarrow 0.6$
- Tip spacing: 0.001 - 0.006  $\rightarrow 0.001$
- Root spacing: Panel length should be mostly constant  $\rightarrow 0.003$
- Spacing at trailing edge: Panel width at trailing edge  $\approx$  half width mid chord panels  $\rightarrow 0.003$
- Spacing at leading edge: 0.001 - 0.006  $\rightarrow 0.001$
- Hub panels Leading edge - Upstream: 4 per 0.1d (diameter)  $\rightarrow L_{LU} = 0.65d \rightarrow 30$  panels
- Hub panels Trailing edge - Downstream: 4 per 0.1d  $\rightarrow L_{TD} = 0.2d \rightarrow 10$  panels
- Hub panel spacing, upstream and downstream: 0.02 (deviates from guidelines, due to hub curvature)
- Hub root spacing: 0.005

The total number of panels in chord and span direction has been determined with a grid convergence study. For a constant advance ratio,  $J = 0.6$ , the thrust and torque coefficient, respectively  $K_t$  and  $K_q$  have been computed for several grid refinements. Figure 3.2 displays  $K_t$  and  $K_q$  as a function of the total number of grid points on the propeller blade ( $n = N_{i,blade} \cdot N_{j,blade}$ ). It shows that the solution accuracy does not necessarily increase by refining the mesh, it is only when the grid becomes very coarse ( $n < 250$ ) that significant deviations in the results occur. This information and the guidelines for grid construction initially led to choosing a panel resolution of  $25 \times 25$  ( $N_{i,blade} \times N_{j,blade}$ ). However, in ComPropApp a new panel file with this resolution is automatically generated after each iteration by a program based on the PROPART toolbox. Since these newly generated panel files have a less ideal distribution, it was chosen to use a finer resolution ( $30 \times 30$ ).

### 3.2.3. Open water diagram

Figure 3.3 displays the open water diagram of the propeller, which is operating in a uniform flow field and does not experience any deformation. The figure displays thrust and torque coefficients, and the open water efficiency,  $\eta_o$  as a function of the advance coefficient,  $J$ . The computed data is compared to what has been obtained in earlier experiments performed with a rigid (aluminium) C4-40 propeller at MARIN [4]. It shows a reasonable resemblance, especially for intermediate advance ratios ( $0.3 < J < 0.7$ ). The lower accuracy at high advance coefficients may be explained by the increasingly dominant viscous forces, for which empiric adjustments are applied in PROCAL. For lower advance ratios, inaccuracies may occur due to stronger leading edge vortex separation, which is not simulated by BEM software.

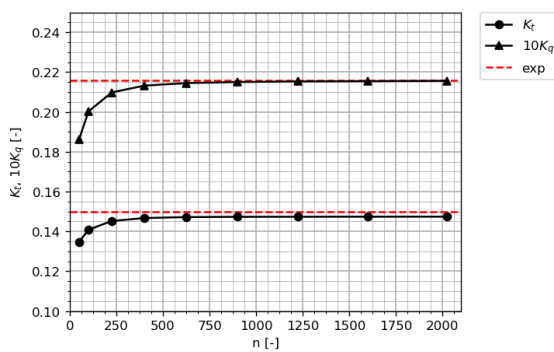


Figure 3.2: BE Grid convergence (experimental data acquired from [4])

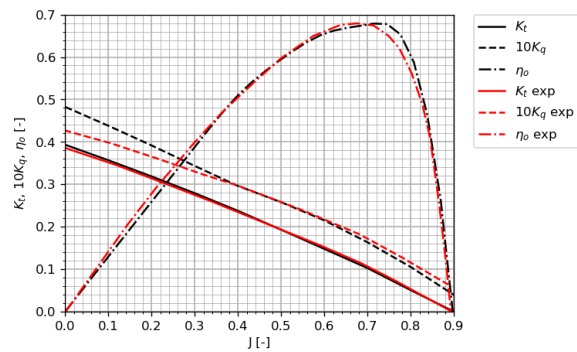


Figure 3.3: Open water diagram rigid C4-40 propeller (experimental data acquired from [4])

In table 3.4 the percentile difference between measurement and computation is displayed. When the BEM software is implemented in the FSI computations, mainly the error in thrust prediction will have an influence on the end result, because deformation is expected primarily in axial direction, i.e. the direction in which thrust applies. It should be noted that it is assumed that the measurements are 100 % correct, whereas these results are corrupted with small measurements errors as well.

Advance ratio [-]	0.1	0.2	0.3	0.4	0.5	0.6	0.7	0.8
Error $\eta_o$ [%]	9.62	7.61	2.96	-0.87	0.47	1.22	0.25	-6.68
Error $K_t$ [%]	-1.27	-1.44	-1.45	-1.17	0.23	2.95	4.01	4.97
Error $K_q$ [%]	-9.01	-6.69	-3.91	0.22	0.39	1.61	5.78	9.80

Table 3.4: BEM errors in comparison to experiments

### 3.2.4. TRIDENT control parameters

The control parameters for TRIDENT are set for the epoxy propeller, as displayed in table 3.5. A motivation for this particular mesh size is given in section 3.2.5. For the modal analysis, 20 modes are used in the computations, as these were found to capture more than 99.99 % of the deformations in comparison with a structural solution using 99 modes.

Parameter	Value
Material density	1140 $kg/m^3$
Young's modulus	3.6 $GPa$
Poisson's ratio	0.30
Water density	998 $kg/m^3$
Grid distribution (chord/span)	30×30
Load form	Front & back pressures
Number of Modes (unsteady FSI)	20

Table 3.5: Control parameters TRIDENT

### 3.2.5. Finite element mesh

Similar to the followed procedure for the panel grid, a grid convergence study is performed to define a suitable FE mesh. This is done by comparing the natural frequencies of the mode shapes determined by PVAST for different mesh refinements. Figure 3.5 displays the convergence behavior of the first three dry natural frequencies against FE grid refinement. The natural frequencies reach a constant value for  $n > 400$ ,  $n$  being the total number of FE nodes. A notable observation was a large deviation in the result when the number of elements in chord direction differed from the number of elements in span direction. To obtain a high enough resolution for the results whilst keeping computational time to a minimum, a grid distribution of 30 × 30 (chord/span) is applied, this grid is displayed in figure 3.4.

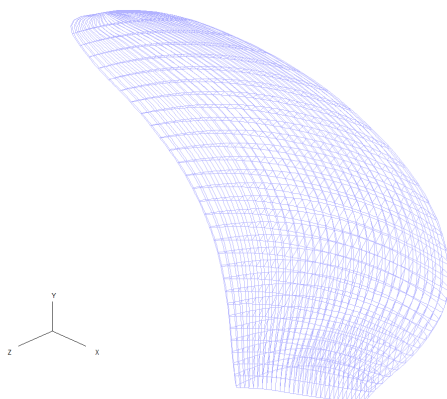


Figure 3.4: FE mesh of the blade (resolution: 30x30)

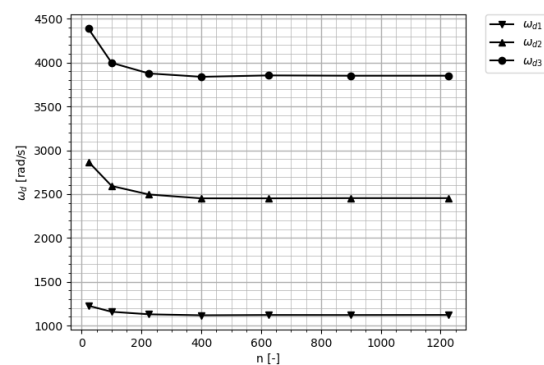


Figure 3.5: FE grid convergence

### 3.3. Processing ComPropApp output

In order to qualitatively compare the results of the FSI computations, a number of criteria had to be set up. A Steady fluid structure interaction analysis on the Wageningen C4-40 propeller has been performed by the ComPropApp. Figure 3.6 shows the displacements for a number of different cross sections. Expectedly, the figures show an increasing deformation when evaluating from root to tip. For small deformations, it can be expected that the cross sectional shapes do not change significantly. Thus, it is reasonable to assume that the deformation can be described with bend and twist deformation evaluated at mid-chord position along the radius for the Epoxy propeller for small deformations. For large deformations an additional parameter, camber, is included as a measure for the changing shape of a cross section. Mainly twist (causing a change in pitch) and camber will influence hydrodynamic behavior of the blades.

The bending deformation ( $w$ ) is evaluated at the mid-chord position of the propeller blade. It is calculated as the absolute value of the mid-chord displacements for each radial point:

$$w_j = \sqrt{dx_j^2 + dy_j^2 + dz_j^2} \quad (3.1)$$

Here  $dx$ ,  $dy$  and  $dz$  represent the displacement in axial, tangential and radial direction respectively. Figure 3.7a displays the bend deformation as a function of the radial position.

Next, the twist deformation is determined by calculating the angular differences at all radial positions. First the angles of the deformed and undeformed blade sections are calculated:

$$\begin{aligned} \phi_{undeformed,j} &= \tan^{-1} \left[ \frac{y_{LE,j} - y_{TE,j}}{x_{LE,j} - x_{TE,j}} \right] \\ \phi_{deformed,j} &= \tan^{-1} \left[ \frac{(y_{LE,j} + dy_{LE,j}) - (y_{TE,j} + dy_{TE,j})}{(x_{LE,j} + dx_{LE,j}) - (x_{TE,j} + dx_{TE,j})} \right] \end{aligned} \quad (3.2)$$

where LE and TE denote the leading edge and trailing edge respectively. With both angles known, the difference ( $\Delta\phi_j = \phi_{deformed,j} - \phi_{undeformed,j}$ ) is calculated and plotted against radial position in figure 3.7b.

Lastly, the change in camber is defined as the maximum distance between the chord line and the camber line, such as shown in figure 3.8. This was done by drawing a straight line through the leading and trailing edge, and defining the normal distance towards  $N_i$  points along on the camber line. The coordinates taken for these points are two-dimensional, i.e. the  $z$ -coordinate is assumed constant for each cross section. The

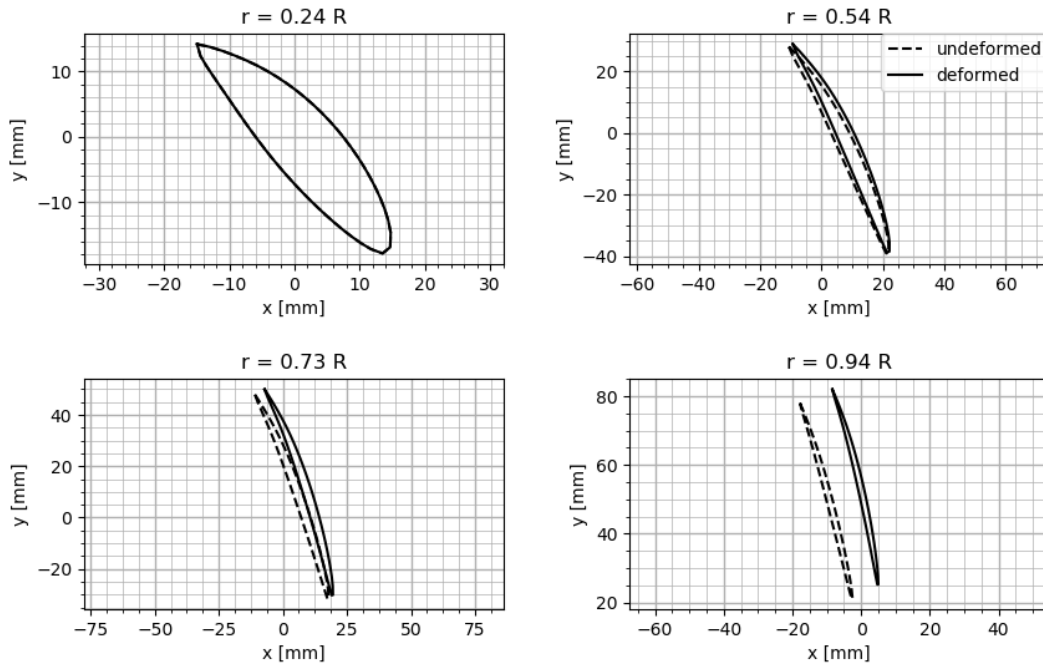
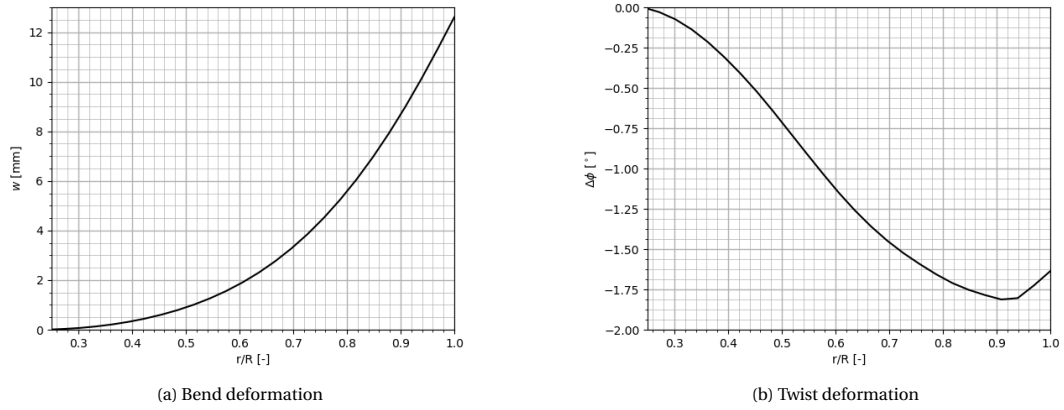


Figure 3.6: Cross sectional deformation in uniform flow ( $n = 15$  rps,  $J = 0.6$ )

Figure 3.7: Deformation along radius in uniform flow ( $n = 15$  rps,  $J = 0.6$ )

chord line vector is defined as:

$$\begin{Bmatrix} x_j \\ y_j \end{Bmatrix} = \begin{Bmatrix} x_{LE,j} - x_{TE,j} \\ y_{LE,j} - y_{TE,j} \end{Bmatrix} t + \begin{Bmatrix} x_{TE,j} \\ y_{TE,j} \end{Bmatrix} \quad (3.3)$$

which can be transformed to the line equation in the form ( $ax + by + c = 0$ ):

$$x_j - \frac{x_{LE,j} - x_{TE,j}}{y_{LE,j} - y_{TE,j}} y + \frac{x_{LE,j} - x_{TE,j}}{y_{LE,j} - y_{TE,j}} y_{TE,j} - x_{TE,j} = 0 \quad (3.4)$$

The distance from any point  $(x_p, y_p)$  to a line  $ax + by + c = 0$  is:

$$d = \frac{|a(x_p) + b(y_p) + c|}{\sqrt{a^2 + b^2}} \quad (3.5)$$

Hence, substitution of equation (3.4), and taking points  $(x_p, y_p)$  at the camber line  $(x_{cl,ij}, y_{cl,ij})$  yields:

$$c_{max,undeformed,j} = \max_i \left\{ \frac{x_{cl,ij} + \frac{x_{LE,j} - x_{TE,j}}{y_{LE,j} - y_{TE,j}} y_{cl,ij}}{\sqrt{1 + \left( \frac{x_{LE,j} - x_{TE,j}}{y_{LE,j} - y_{TE,j}} \right)^2}} \right\} \quad (3.6)$$

In a similar manner as for the twist deformation, an expression for the maximum deformed camber can be computed. The difference in camber is then defined as:  $\Delta c_{max,j} = c_{max,deformed,j} - c_{max,undeformed,j}$ . This parameter is then non-dimensionalized to a percentage of the local chord length:

$$\Delta c_{max,j}[\%] = \frac{\Delta c_{max,j}[\text{mm}]}{L_{chord,j}} \cdot 100\% \quad (3.7)$$

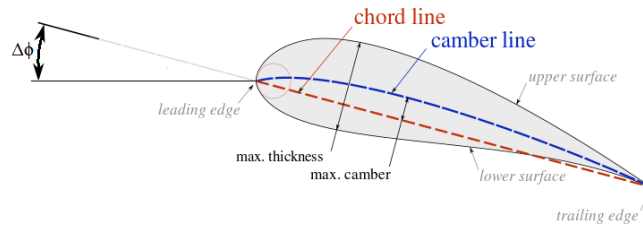


Figure 3.8: Schematic view of a blade cross section (adapted from [28])

### 3.4. Steady FSI analysis

Now that the deflection profile of the blade is known, the calculations performed by ComPropApp can be evaluated. This section contains results of the ComPropApp 1.0.1 computations. It is assumed that PROCAL provides the correct data, which is a reasonable assumption, as it has already proved to agree well with measurements (see figure 3.3). What remains is the interaction between PROCAL and TRIDENT, and the structural solution of TRIDENT. Two methods are presented in order to verify the results; a comparison with an analytic solution, and a manual coupling between PROCAL and TRIDENT. These are treated in the following two sections.

#### 3.4.1. Analytic solution

The twist and bend deformation results given in figures 3.7a and 3.7b display the converged deformation values in a uniform flow field, i.e. the propeller has reached a steady state where the deformations are constant in time. This means that all forces acting upon the the propeller have reached an equilibrium. Regardless, there are still accelerations due to centrifugal and Coriolis forces. These are in radial and tangential direction though, therefore it is assumed that the axial forces are static. This, combined with the fact that bend deformations are relatively small and mostly axial, means that they may be analytically solved with relative ease.

PROCAL provides an output of forces for each panel center, the axial forces have been utilized to approximate point forces at a number of radial positions. These are displayed in figure 3.9. The sum of all these point loads amounts to 25 % of the propeller thrust, since the total thrust is distributed over four blades.

In order to calculate the bend deformations, the blade is modelled as a two dimensional beam with a non-uniform cross section. This is modelled as a two dimensional plane, where the x- axis and y-axis represent radial and axial directions respectively. The two-dimensional simplification is shown in figure 3.10.

This static problem is solved by means of superposition, where the beam is subdivided into  $N_j$  segments. Each of these has a different cross section, and different loading. The first segment is modeled as clamped at one end, and has a prescribed vertical force and moment causing it to deform. The vertical deformation  $\delta$  and angular deformation  $\theta$  are determined at the first two radial positions:

$$\begin{aligned} \delta_0 &= 0 \\ \delta_1 &= \left( \sum_{p=1}^{N_j} F_p \right) \cdot \frac{\Delta r^3}{3EI_1} + M_1 \cdot \frac{\Delta r^2}{2EI_1} \end{aligned} \quad (3.8)$$

$$\begin{aligned} \theta_0 &= 0 \\ \theta_1 &= \left( \sum_{p=1}^{N_j} F_p \right) \cdot \frac{\Delta r^2}{2EI_1} + M_1 \cdot \frac{\Delta r}{EI_1} \end{aligned} \quad (3.9)$$

where the elasticity modulus is denoted by E and  $M_1$  denotes the moment acting upon segment one, calculated as:

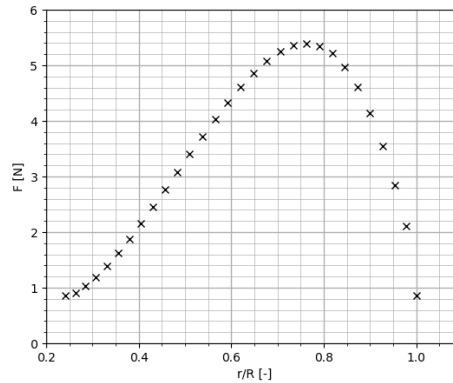


Figure 3.9: Axial point forces applying on finite number of radial positions

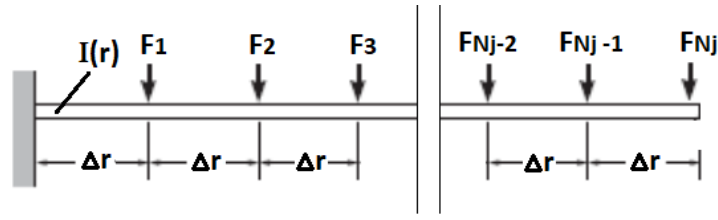


Figure 3.10: Illustration of beam approximation

$$M_j = \left( \sum_{p=j+1}^{N_j} F_p \right) \cdot (r_p - r_j) \quad (3.10)$$

The bending moment of inertia,  $I_j$ , is calculated per cross section, with an approximation for airfoils:

$$I_j = K_I c_j t_j \cdot (t_j^2 + h_j^2) = 0.036 \cdot c_j t_j \cdot (t_j^2 + h_j^2) \quad (3.11)$$

where  $K_I$  is a coefficient determined by [18],  $c_j$  is the local chord length. The local maximum camber and maximum thickness are represented by  $h_j$  and  $t_j$  respectively.

To calculate the angular and vertical deformation for the remaining radial positions, each segment is again considered as a clamped beam. However, the clamped sides now have a non-zero position and angle, which should be considered as well. The position and angle of the previous radial position are therefore added to the equations:

$$\delta_j = \left( \sum_{p=j}^{N_j} F_p \right) \cdot \frac{\Delta r^3}{3EI_j} + M_j \cdot \frac{\Delta r^2}{2EI_j} + \theta_{j-1} \cdot \Delta r + \delta_{j-1} \quad j = 2, \dots, N_j \quad (3.12)$$

$$\theta_j = \left( \sum_{p=j}^{N_j} F_p \right) \cdot \frac{\Delta r^2}{2EI_j} + M_j \cdot \frac{\Delta r}{EI_j} + \theta_{j-1} \quad j = 2, \dots, N_j \quad (3.13)$$

Figure 3.11 displays a comparison between the axial deformation as determined by the ComPropApp and the analytic solution for the simplified structure. It shows that qualitatively there is a decent resemblance between the solutions, with some explicable differences. The analytic solution yields larger deformations near the root and the opposite in the tip region. This can be explained by the larger pitch angles near the root which is neglected in the inertia term (eq. (3.11)), but would actually increase the stiffness in axial direction. The same principle may be responsible for a lower expected deformation near the tip, since here the axial forces act nearly perpendicular to the structure.

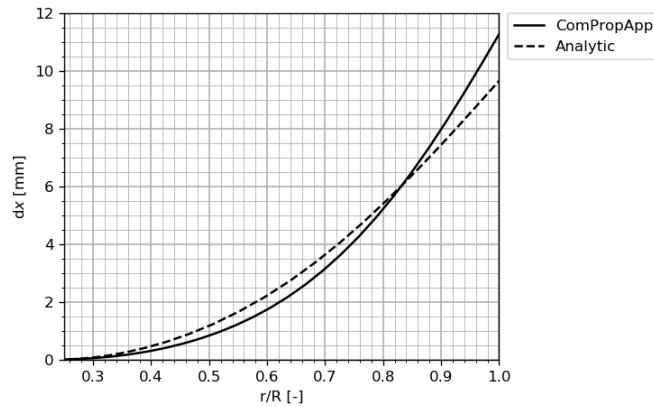


Figure 3.11: Comparison analytic and numeric axial deformation

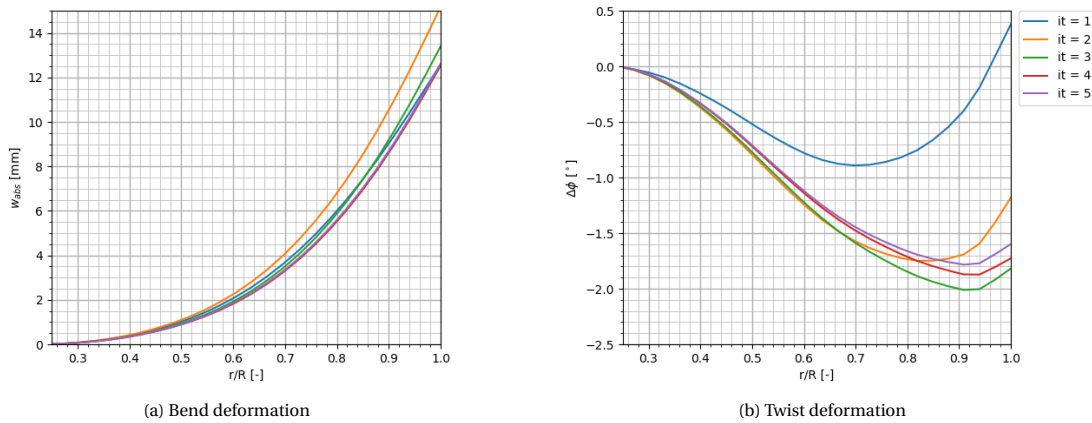


Figure 3.12: Deformation in uniform flow, manual coupling ( $n = 15$  rps,  $J = 0.6$ )

### 3.4.2. Manual coupling procedure

As an additional check on the performance of the ComPropApp in the steady case, assuming both PROCAL and TRIDENT yield reliable results, the BEM-FEM coupling is performed manually. As this is a static analysis, and it has already been shown that convergence was reached in only a few iterations, it should be possible to obtain similar results by manually implementing the pressure loads into TRIDENT to compute deformations, executing PROCAL with the new geometry, recomputing deformations, etc. The results of this manual coupling are displayed in figure 3.12, where the last iteration shows excellent resemblance with what has been obtained using the ComPropApp. An important difference between the ComPropApp procedure and the manual procedure is in the load application on the blade. Where the ComPropApp applies the loads incrementally, here the entire load has been applied immediately. The consequences of this approach are notable in figure 3.12. Although the bend deformation is estimated accurately after the initial FEM analysis, the twist computations are wrong. The consequence is a prediction of an even larger thrust by PROCAL, leading to more bend deformation of the blade in the second iteration. This explains why, in particular for relatively large deformations, it may be beneficial to use the incremental pressure build up in order to prevent diverging solutions. Notable is the converging behavior of the twist deformation, which may be a suitable criterion to determine whether a final solution has been reached.

### 3.4.3. Validity limits

To successfully apply ComPropApp as a development tool, it should be universally applicable. That is, the application provides feasible results for various conditions, i.e. various flow fields, propeller geometries and material properties. The steady FSI module, has shown limitations for the material properties. Simulations performed for isotropic materials with the elasticity modulus as a variable have shown that for extremely flexible materials, Hooke's Law is no longer complied with. This discrepancy is displayed in figure 3.13a,

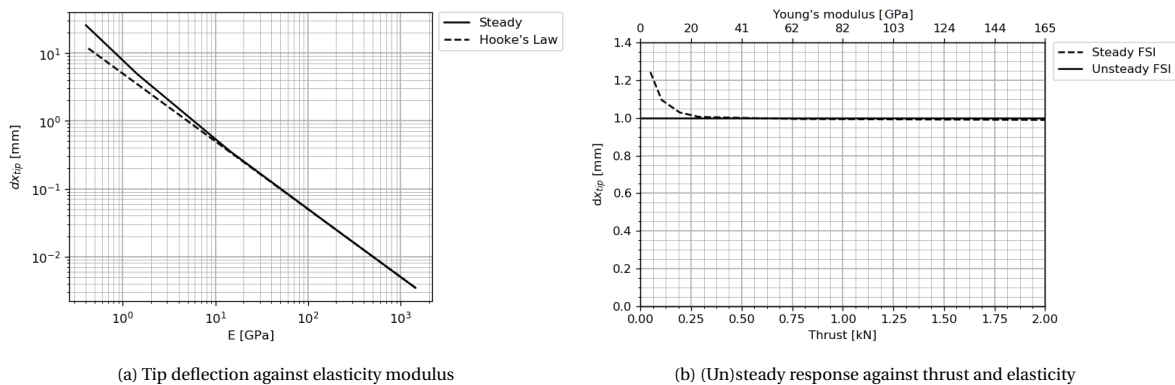


Figure 3.13: Comparisons tip deflection after  $1^{st}$  iteration

showing the tip deformation as a consequence of the pressures on the undeformed geometry against elasticity. It shows that for  $E < 10 \text{ GPa}$  the deformation is over predicted by the static non-linear analysis in TRIDENT/VAST, the implemented structural solver in ComPropApp. One could conclude from figure 3.13a that the deviation arises as a result of non-linear effects. However, these would not lead to differences of such extent. More importantly, this behavior occurs regardless of the deformation size, hence it cannot be a result of non-linearities, as was found in an open water comparison between the unsteady and steady FSI module. For open water conditions, it can be assumed that the bend deformation of a blade is constant, as long as the Elasticity modulus/thrust is constant. Figure 3.13b displays the computed ComPropApp results for conditions where the deformation is predicted at 1 mm, which shows that the steady FSI module deviates below 250 N of thrust. As a check whether this would be physically possible, the same conditions were modelled in ANSYS and Abaqus. Both showed fully linear behavior of the material, confirming the error in VAST. These limitations were caused by the solution technique applied in the non-linear VAST analysis. It was also found that the linear solution, with the same applied loads, did provide the correct answer. In the conditions modelled thus far, the thrust is higher than that ( $\pm 400 \text{ N}$ ), hence it does not significantly influence the results presented above.

### 3.5. Unsteady FSI analysis

With the steady FSI analysis reviewed, the next part to be investigated is the unsteady FSI method in the ComPropApp. Like for the steady FSI computations, ComPropApp 1.0.1 is used in this section. The most obvious method to evaluate the unsteady FSI, is via a comparison to the steady method in similar conditions. This is done by performing an unsteady computation in a uniform flow field, in which case it should yield an almost constant deformation throughout a revolution equal to the steady case. Further, the unsteady computations for a non-uniform flow field can be compared with a number of steady computations where the flow field is only varying in radial direction. This number of radially varying flow fields are taken at different angular positions of the non-uniform flow field. This also provides an insight into whether a hydrodynamic analysis is required or the solution can be assumed quasi-static, which has the benefit of computational simplicity.

#### 3.5.1. Open water conditions

Initially, the computations for the unsteady analysis are performed in open water, and compared to the steady FSI results computed earlier. The results of these computations are shown in figures 3.14a and 3.14b. The figures display some large inequalities, especially for the twist deformation. This can have a number of causes. Listed below are those which have been investigated.

- Pressure interpolation in the steady module (EXTPROPTEC & PROCAL).
- Computation differences between steady and unsteady PROCAL simulations.
- Geometric interpolation differences in the steady and unsteady module (PROPART Toolbox).
- Geometric linearization in unsteady module (Modal analysis).

#### Pressure interpolation in the steady module:

A simulation for both the unsteady and the steady solver was performed for the first iteration only, i.e. no coupling, was performed. This yielded an accurate resemblance between the bend displacements, but the twist deformations started diverging immediately (see figure 3.15). It should be noted that a even a minor difference in pitch will significantly change the end result of the simulation due to the iterative nature of the solution. The observations suggest that, while the sum of the applied forces is correct, the positions where they are applied may differ slightly. This may be explained by the different methods in transforming pressures to forces in the steady and unsteady FSI modules. The steady case uses the pressures at the panel corners whereas the unsteady case applies the center pressures. The pressures at the panel centers, i.e. the collocation points of the panels, are direct results of the system of equations solved by PROCAL. The pressures at the panel corners applied in the steady FSI module are interpolated values. On top of that, the steady procedure applies EXTPROPTEC to distribute the pressures over the radial positions specified in the propeller geometry file. This is another interpolation, and in this case also leads to a decrease in the radial resolution of the pressure description.

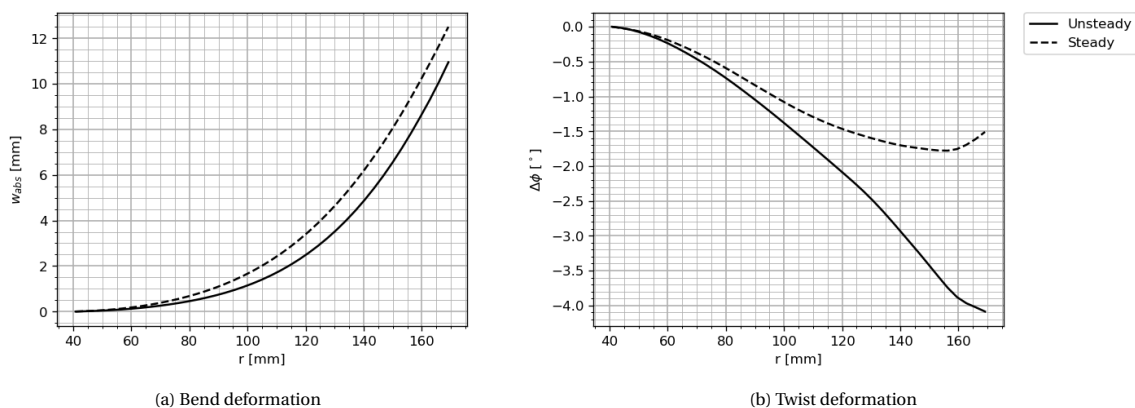


Figure 3.14: Initially computed deformations in uniform flow ( $n = 15$  rps,  $J = 0.6$ )

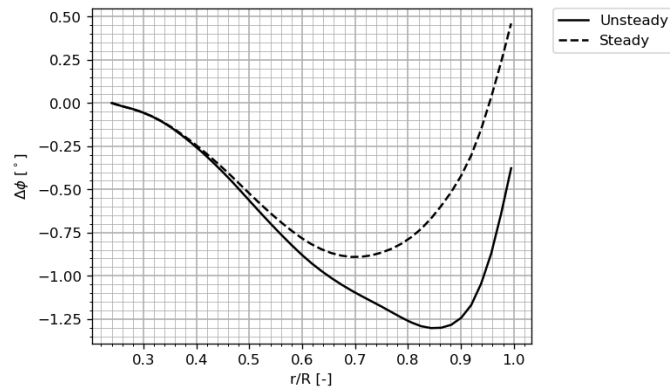


Figure 3.15: Twist along radius for 1<sup>st</sup> iteration ( $n = 15$  rps,  $J = 0.6$ )

### Computation differences steady and unsteady PROCAL simulations:

Another explanation for the difference in twist angles could be the small differences between steady and unsteady PROCAL computations. Therefore the pressure distributions were compared for both cases at various radial positions. Though the total thrust difference for the steady and unsteady PROCAL solutions is just 0.1 %, on a local scale the deviations become more significant. Figure 3.16 displays the pressure difference between the pressure and suction side along the chord in the tip and root region for the undeformed blade. For  $r < 0.45R$ , the unsteady method yields a larger pressure difference near the trailing edge of the cross section, such that more twist deformation would be expected. For  $r > 0.85R$  the opposite holds, such that less twist is expected. Looking at the predicted twist deformations against the non dimensional radius in figure 3.15, these pressure deviations may have a small influence on the result, though it is clearly not the only factor of influence.

### Geometric interpolation differences in the steady and unsteady module:

Next, the influence of Points2Prop was investigated, this is the PROPART toolbox which transforms the deformed finite element structure to a panel, and geometry file. Again, this is an interpolation step, as it smoothens the propeller surface such that a realistic blade shape without any sharp corners arises. To define the consequence of such interpolation on the predicted lift forces, PROCAL simulations have been performed for the original blade shape, as well as one generated by Points2Prop with the undeformed finite elements grid. These were then compared and revealed three issues: 1) The radial grid distribution after Points2Prop was linear. 2) The chordwise grid distribution changed. 3) The geometries showed small differences.

The FEM grid is uniformly distributed in space, whereas the original BEM grid is locally refined in the tip and root area. Points2Prop generates a panel grid with the same resolution as the original, but uniformly distributed along the radius, consequentially the local resolution in the root and tip decrease. In order to find to what extent this influences the fluid computations, the lift coefficients were compared. The lift coefficient

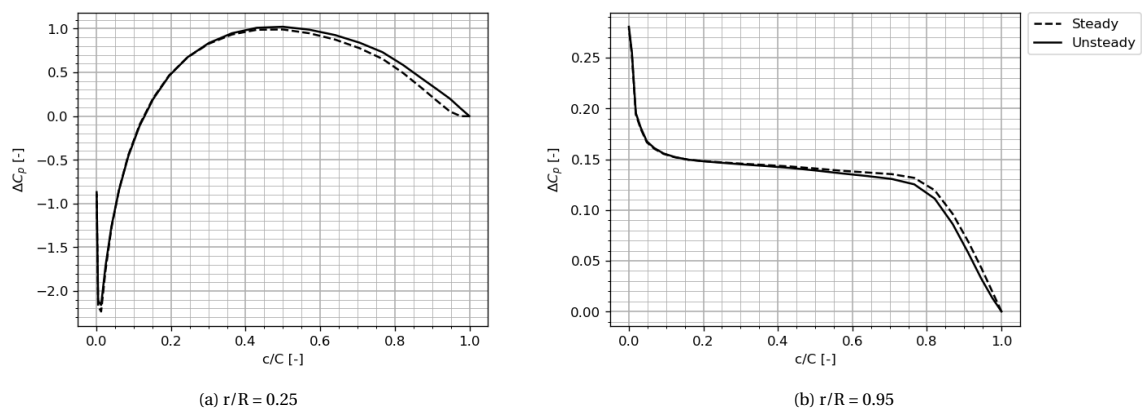


Figure 3.16: Pressure difference along chord in uniform flow (undeformed,  $n = 15$  rps,  $J = 0.6$ )

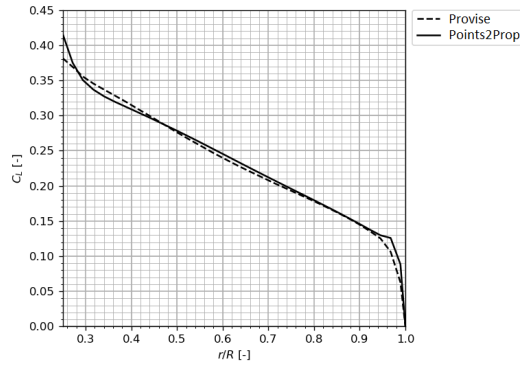


Figure 3.17: Lift coefficients along blade radius in uniform flow (undeformed,  $J = 0.6$ )

is defined with the normal force ( $C_n$ ), and tangential force ( $C_t$ ) components obtained by PROCAL:

$$C_L = C_n \cdot \sin \phi - C_t \cdot \cos \phi = \frac{F_T(r)}{\frac{1}{2} \cdot \rho g c(r) \cdot (nr)^2} \tag{3.14}$$

where  $F_T$  denotes the local thrust force per unit blade length and  $c$  the local chord length. Figure 3.17 displays the lift coefficients for the Provisé grid and for the Points2Prop generated grid. Notable is that the differences are most significant in the tip and root area. This is a result of the difference in grid distribution. Mainly differences in the tip region will influence the predicted thrust, since the local thrust force is higher nearby the tip due to the higher blade velocity, but also the relative difference between lift coefficients is significantly larger. Thrust differences near the tip region have an even larger effect on the bend deformation, as it is a  $3^{rd}$  order function of the blade radius (eq: (3.8)). However, this effect can be mitigated by increasing the radial resolution of the panel grid.

The difference in chordwise panel distribution was found to influence the positions of the applied point loads. This was due to the conversion of panel center pressures to FE nodal loads. Since the load is applied to the undeformed FE model, Compropapp used the panel center coordinates of the original panel distribution in the conversion. Therefore, the panel grid needs to be consistent in all revolutions in order to get the point loads at the correct positions. This problem was solved by initially using the Points2Prop generated panel grid, rather than the one constructed with Provisé grid to ensure a consistent grid distribution.

Provisé and Points2Prop use the same propeller geometry (\*.ppg) file to construct a grid, but have different methods for interpolation between the given coordinates in the geometry file. As a consequence the geometry of the Points2Prop generated panel file differs from the panel file generated with Provisé. Note that this problem occurs regardless of the grid refinements, it depends on the geometry file. Therefore, it can be solved by using a \*.ppg file which is more refined in the tip region.

A new panel grid was constructed with Points2Prop, a higher grid resolution (30x30), with a new \*.ppg file (the new geometry file for the testing propeller, which has a finer tip resolution). It significantly decreased

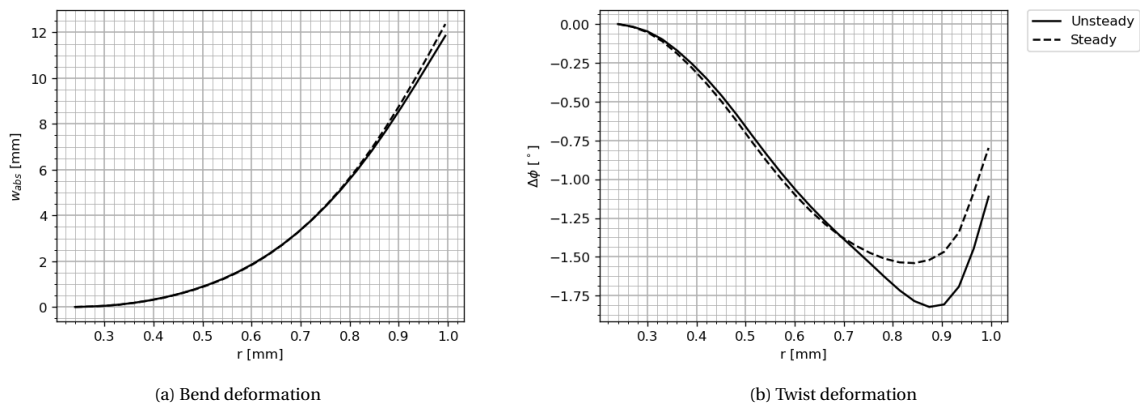


Figure 3.18: Deformation along radius in uniform flow ( $n = 15$  rps,  $J = 0.6$ )

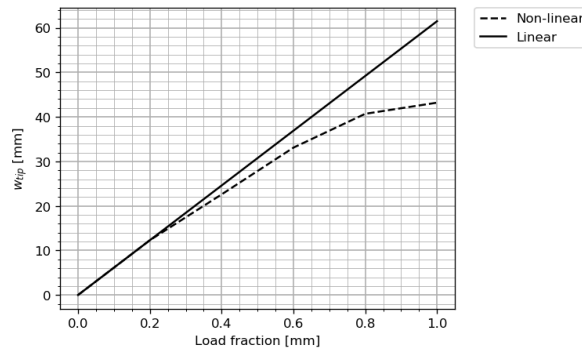


Figure 3.19: Comparison linear and non-linear tip deflections

the difference between both solvers, as is shown in figure 3.18. The main cause of this improvement is the now consistent panel grid, hence an adjustment to ComPropApp was performed in which a new PROPART toolbox, Propart4Comprop (P4C) always generates the panel file. Therefore the user is no longer required to supply a blade panel file.

### Geometric linearization in unsteady module:

To determine the significance of the linearity assumption, a non-linear analysis was compared with a linear analysis for deformations up to 60 mm. Figure 3.19 displays this comparison. It shows that the non-linear solution starts to experience stiffening behavior for deformations  $> 13$  mm. Hence the conditions modelled thus far are within the linear regime. Based on this knowledge, the non-linear effects are considered to be negligible for, say,  $w_{tip} < 10$  mm. With this particular blade having a 340 mm diameter,  $w_{tip}/D_p < 0.03$  is considered as a guideline to suffice the linearity assumption.

### 3.5.2. Wakefield conditions

The next step in the verification process is evaluating the computations in more realistic, non-uniform flow conditions. The cavitation tunnel at MARIN offers the possibility to generate wakefield conditions. Measurements have been performed on these wakefields for a number of different flow velocities. Figure 3.20 displays the non-dimensionalized axial velocity measured at 4 m/s. These measurements are time-averaged values since the inflow is turbulent and therefore time dependent. It should be noted that this is the nominal wakefield, which does not consider propeller-hull interaction, hence it will differ slightly from the effective wakefield. It is of interest to determine in what way the propeller is influenced by this non-uniformity. This can be performed in three different ways:

- Static, tangentially averaged flow: This is the simplest method, where the measured wakefield is averaged in tangential direction but kept varying along the radius.
- Quasi-static, tangentially varying flow: Here the radial velocity distribution is taken at a finite number of angular positions to obtain a number of tangentially invariant wakefields.
- Hydro-elastic: For this approach the original wake field is applied, the dynamic vibrations of the propeller, and the fluid behavior as a consequence of the vibrations are considered as well.

The (quasi-) static approach can be performed with the steady FSI module of ComPropApp, since the imported wakefields are not time dependent in this case. The hydro-elastic approach is simulated with the unsteady FSI module. All three approaches were elaborated in order to determine the significance of modeling the dynamic propeller behavior.

To obtain a wakefield for the static approach that is only varying in radius, the wakefield, which is given in polar coordinates is averaged over the tangential direction:

$$\mathbf{v}_i = \frac{\sum_{j=1}^{N_j} \mathbf{v}_{i,j}}{N_j} \quad (3.15)$$

where  $\mathbf{v}$  denotes the velocity vector in axial, radial and tangential direction. The wakefile is distributed in  $N_i$  radial and  $N_j$  tangential coordinates.

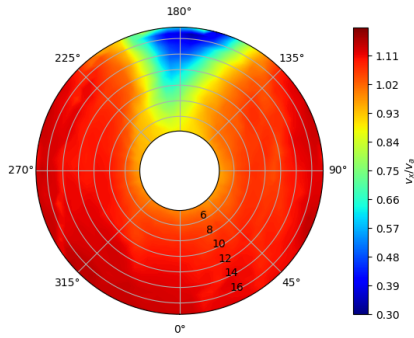


Figure 3.20: Nominal axial wakefield measured at 4 m/s

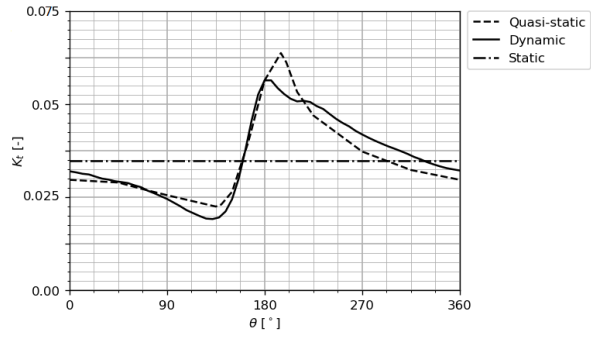


Figure 3.21: Quasi-static versus dynamic BEM results

For the quasi-static approach, the wakefield shown in figure 3.20 is utilized to create 16 different wakefields, all varying in radial direction but tangentially constant. The wakefields are obtained by extracting the radial velocity distribution at 16 angular positions.

With the unsteady FSI module, a non-uniform wakefield can be implemented with the large advantages that it accounts for the vibration velocities in the unsteady potential solution and that the dynamic structural response is modelled. Prior to the unsteady FSI simulations, a modal analysis was performed in order to find the eigenmodes and the natural frequencies. The wet and dry natural frequencies are displayed in table 3.6.

Mode number	$\omega_d$ [Hz]	$\omega_w$ [Hz]
1	178.5	45.0
2	388.9	110.2
3	597.4	186.1
4	786.8	265.8
5	968.4	351.2

Table 3.6: Natural frequencies Epoxy

Prior to performing the simulations in ComPropApp, steady and unsteady BEM simulations were performed in the case of a rigid propeller. Where open water conditions yield almost equal results ( $\Delta K_t \pm 0.1\%$ ), there are significant differences in wakefield conditions. A comparison of the thrust coefficients is shown in figure 3.21. The static, quasi-static, and hydro-elastic methods yield similar results for the total thrust delivered throughout one revolution, i.e. the total area under the thrust curves are equal ( $\pm 1\%$ ). With that, one can conclude that the static approach is a reasonable method to predict the delivered thrust and average deflection of the propeller blades. However, as the objective of flexible propellers is to reduce blade loading locally at a certain point along the revolution, the static approach does not describe the thrust in sufficient detail. Hence, the comparison is reduced to the quasi-static and hydro-elastic approach only.

In order to define a criterion for when a hydro-elastic computation is preferred over a quasi static solution, simulations were performed for various conditions. Following the findings in the previous section, a consistent panel grid was applied in the simulations to overcome the problems with Points2Prop. Figure 3.22

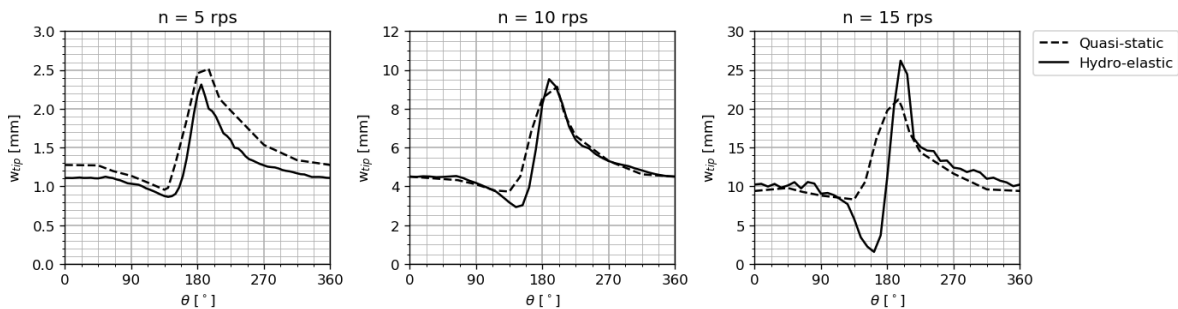


Figure 3.22: Tip deflection throughout revolution ( $J = 0.6$ )

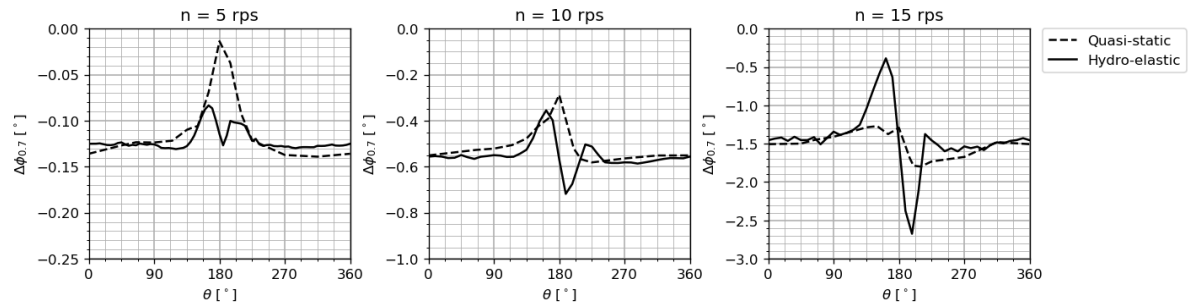


Figure 3.23: Twist deflection throughout revolution ( $J = 0.6$ ,  $r/R = 0.7$ )

displays a comparison between a quasi-static and a hydro-elastic computation for the tip displacement, for a range of shaft velocities. The variations in deflection are large, due to the local differences in flow velocity changing the advance ratios. The advance ratios can locally vary in the range  $0.2 < J < 0.7$ . As expected, at higher shaft velocities the dynamic effects start to become more significant and the quasi-static approach is no longer representative. With the modal analysis it was found that the first mode shape is mainly responsible for the behavior seen in the figures, and that it starts to resonate above  $n = 10$  rps. A FEM analysis was performed to find the first wet natural frequency ( $\omega_{w1} = 45\text{Hz}$ ), which is slightly above the excitation observed in figure 3.22 for 15 rps. At the lower shaft velocities, a more constant error in tip deflection is observed. This is due to the steady FSI module, which has a limited validity for low thrust ( $T < 250$  N). At 5 rps the average thrust is 50 N, as can be seen in figure 3.13b a similar error can be found for open water conditions. The twist deformation is displayed in figure 3.23, where the dynamic effects are clearly visible. For low vibration velocities of the propeller cause a change in load prediction by PROCAL, which reduces the twist peak predicted, whereas resonance occurs at higher vibration velocities. These effects are not captured in the quasi-static solution.

### 3.5.3. Oblique wake conditions

The previous section showed large deviations between the quasi-static and dynamic solution in a measured wakefield. To have a fair comparison between the two methods, a condition is required for which the quasi-static approach is expected to be valid. Hence, the choice was made to compare both computations for an oblique wake. This is a uniform flow with a constant inflow angle, as illustrated in figure 3.24, in this case  $\gamma = 20^\circ$ . In a Cartesian coordinate system, the velocity now has a  $y$ -component ( $v_y = \sin \gamma \cdot v_a$ ). Transforming this to a radial and tangential velocity component in the polar coordinate system yields:

$$\begin{aligned} v_\theta &= v_y \cdot \sin \theta \\ v_r &= -v_y \cdot \cos \theta \end{aligned} \quad (3.16)$$

That means the effective angle of attack is a sinusoidal function of the propeller revolution. Hence, an oblique wake causes one excitation frequency to the blade equal to the shaft rotation frequency. To qualitatively compare the hydrodynamic solution with the quasi-static solution, the excitation frequency should be much lower than the 1st wet natural frequency ( $\omega \ll \omega_{w1}$ ). To compensate for the differences in thrust prediction between a quasi-steady and unsteady PROCAL simulation Set Point Iteration (SPI) was applied, such

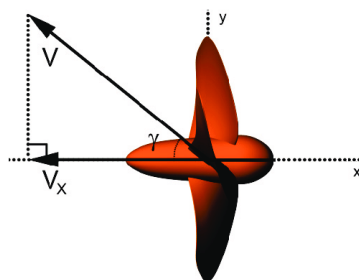
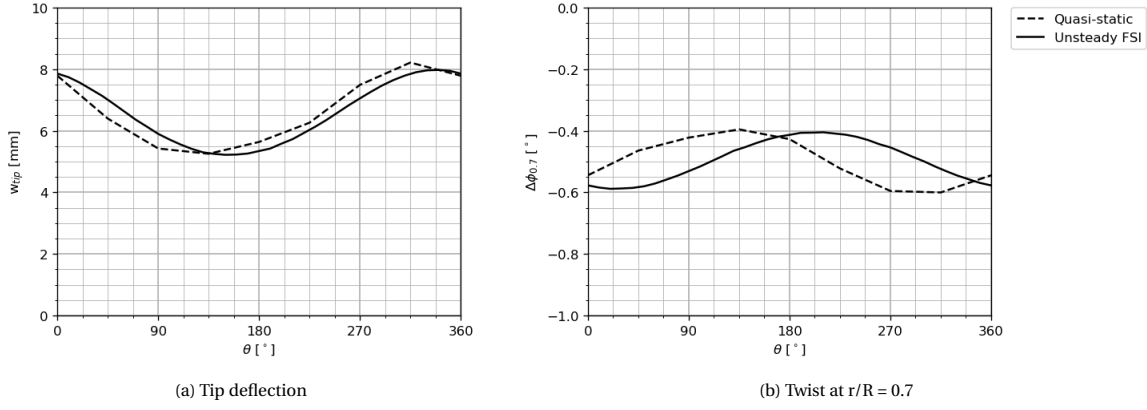


Figure 3.24: Illustration oblique wake (adapted from [23])

Figure 3.25: Deformations in oblique flow ( $\gamma = 20^\circ$ ,  $n = 10$  rps,  $J = 0.6$ )

that the thrust prediction for the undeformed geometry was equal for both cases. The results of the computations are shown in figure 3.25. While the period and magnitude of the deformations are comparable, there clearly is a phase difference between the both solutions. To find what causes this phase lag in the dynamic solution, a simplified 1-DoF (Degree of Freedom) spring-damper model was considered. The equations of motion for a forced vibration solution are:

$$M \cdot \ddot{x} + D \cdot \dot{x} + K \cdot x = F \quad (3.17)$$

where  $F$  is a harmonic function that can be described in complex notation as:

$$F = F_{amp} \cdot e^{i(\omega \cdot t + \epsilon_F)} \quad (3.18)$$

The displacement is also expected to behave harmonically:

$$\begin{aligned} x &= x_{amp} \cdot e^{i(\omega \cdot t + \epsilon_x)} \\ \dot{x} &= x_{amp} \cdot i\omega \cdot e^{i(\omega \cdot t + \epsilon_x)} \\ \ddot{x} &= -x_{amp} \cdot \omega^2 \cdot e^{i(\omega \cdot t + \epsilon_x)} \end{aligned} \quad (3.19)$$

Substitution of equations (3.18) and (3.19) into equation (3.17) yields:

$$(-\omega^2 \cdot M + i\omega \cdot D + K) \cdot x_{amp} \cdot e^{i(\omega \cdot t + \epsilon_x)} = F_{amp} \cdot e^{i(\omega \cdot t + \epsilon_F)} \quad (3.20)$$

Division by the harmonic part gives:

$$x_{amp} \cdot e^{i\epsilon_x} = \frac{F_{amp}}{-\omega^2 \cdot M + i\omega \cdot D + K} \cdot e^{i\epsilon_F} \quad (3.21)$$

The phase and amplitude of the displacement are:

$$\begin{aligned} x_{amp} &= \left| \frac{F_{amp}}{-\omega^2 \cdot M + i\omega \cdot D + K} \cdot e^{i\epsilon_F} \right| \\ \epsilon_x &= \arctan \frac{\operatorname{Im} \left( \frac{F_{amp}}{-\omega^2 \cdot M + i\omega \cdot D + K} \cdot e^{i\epsilon_F} \right)}{\operatorname{Re} \left( \frac{F_{amp}}{-\omega^2 \cdot M + i\omega \cdot D + K} \cdot e^{i\epsilon_F} \right)} \end{aligned} \quad (3.22)$$

That means the phase difference between the excitation and displacement are dependent on the damping coefficient, or rather the ratio between damping and mass/stiffness properties. However, for an estimated hydrodynamic damping ratio of 5%, a phase lag of just  $1.5^\circ$  was predicted for the case shown in figure 3.25. This led to conclude that while damping does cause phase lag, it does not dominate the behavior.

Another cause for the phase lag is the influence of the displacement velocity on the PROCAL simulations. An unsteady FSI computation was executed under similar velocities as in figure 3.25, but a smaller angle of incidence ( $\gamma = 10^\circ$ ). This reduces the load amplitude, and thus the displacement amplitude. Table 3.7 displays the consequence of reducing  $\gamma$ . It confirms that a reduction in vibration velocity significantly reduces the phase lag, thereby showing the importance of including the dynamic behavior in the BEM software.

Method	$\gamma$ [°]	$\Delta\varepsilon_{bend}$ [°]	$x_{amp}$ [mm]	$\dot{x}_{max}$ [m/s]
Quasi-static	20	0	1.38	0
Hydro-elastic	20	20	1.38	1.35
Hydro-elastic	10	10	0.66	0.341

Table 3.7: Evaluation for different angle of incidence

### 3.6. Verification

Several changes were applied to improve the ComPropApp, these were all implemented in the new version: ComPropApp 1.0.2. One important adjustment is the replacement of Points2Prop by Propart4Comprop (P4C). This solves the problem of inconsistency in grid distributions and has the additional advantage of not requiring a user supplied blade panel file, as it can generate a panel file directly from the geometry file. Another adjustment has been applied to the stress analysis. Initially, the stress analysis only applied the hydrodynamic load for one revolution. Due to startup phenomena in the time-domain, this had to be increased, the number of revolutions for which the analysis is performed is now a user defined parameter set to 5 revolutions by default. Further, a number of programming errors have been corrected. With all the corrections applied, the verification process could be finalized. The verification was performed for several conditions, with the steady FSI and unsteady FSI modules. These simulations are performed mainly for epoxy and Sikablock M700. Also, a simulation with a bronze propeller was performed, with the purpose to determine the influence of slight changes in the panel grid. As the deformation of the bronze propeller should be near zero, the last BEM computation in the ComPropApp should yield the same results as an undeformed BEM computation. A composite propeller simulation was performed as well by the ComPropApp, namely a glass fiber reinforced epoxy. Table 3.8 displays the conditions that have been computed.

#	Analysis type	Wake	Material	J [-]	n [rpm]	$v_a$ [m/s]
1	Unsteady, Stress	Open water	Sikablock M700	0.6	300	1.02
2	Unsteady, Stress	Open water	Sikablock M700	0.7	300	1.19
3	Unsteady, Stress	Open water	Sikablock M700	0.6	400	1.36
4	Unsteady, Stress	Open water	Sikablock M700	0.7	400	1.58
5	Unsteady, Steady, Stress	Open water	Epoxy	0.6	600	2.04
6	Unsteady, Steady, Stress	Open water	Epoxy	0.6	900	2.04
7	Unsteady, Steady, Stress	Open water	Epoxy	0.73	1190	4.92
8	Unsteady, Stress	Wakefield (fig: 3.20)	Epoxy	0.6	600	2.04
9	Unsteady, Steady, Stress	Open water	Composite [0°/90°]	0.57	1025	3.31
10	Unsteady, Steady, Stress	Open water	Composite [0°/30°]	0.57	1025	3.31
11	Unsteady	Wakefield (fig: 3.20)	Bronze	0.6	1000	3.40

Table 3.8: Conditions for verification

For the listed conditions, a stress analysis was performed as well. In the stress analysis the load of the last revolution in the unsteady FSI is applied to the structure. Like the unsteady FSI, it solves the dynamic problem using modal analysis, though it is applied in the time domain as a forced vibration analysis. Besides the stresses, this method yields the deformations, those can be compared to the (un)steady results as an additional check.

### 3.6.1. Sikablock M700

The results performed for the Sikablock M700 propeller are displayed in figure 3.26. The measured material properties for SikaBlock are displayed in table 3.9. The comparison of the unsteady FSI with the deformations found in the stress analysis, agrees well in general. The predicted bend deformations are nearly identical, for the twist small differences are observed. That said, the twist is the gradient of deflection and in general quite small. As a result of that, a relatively large error is difficult to avoid. The differences between the two solutions can be explained by rounding errors in the TRIDENT environment. Nevertheless, the results are conclusive enough to confirm that the Fourier transform, transforming time to the frequency domain, is being applied correctly. This is mainly where the unsteady FSI differs from the stress analysis, both approached experience the load input generated by the last PROCAL computation.

<b>Parameter</b>	<b>Value</b>
Material density	650 $kg/m^3$
Young's modulus	800 $MPa$
Poisson's ratio	0.35
Flexural strength	26 $MPa$

Table 3.9: SikaBlock M700 properties

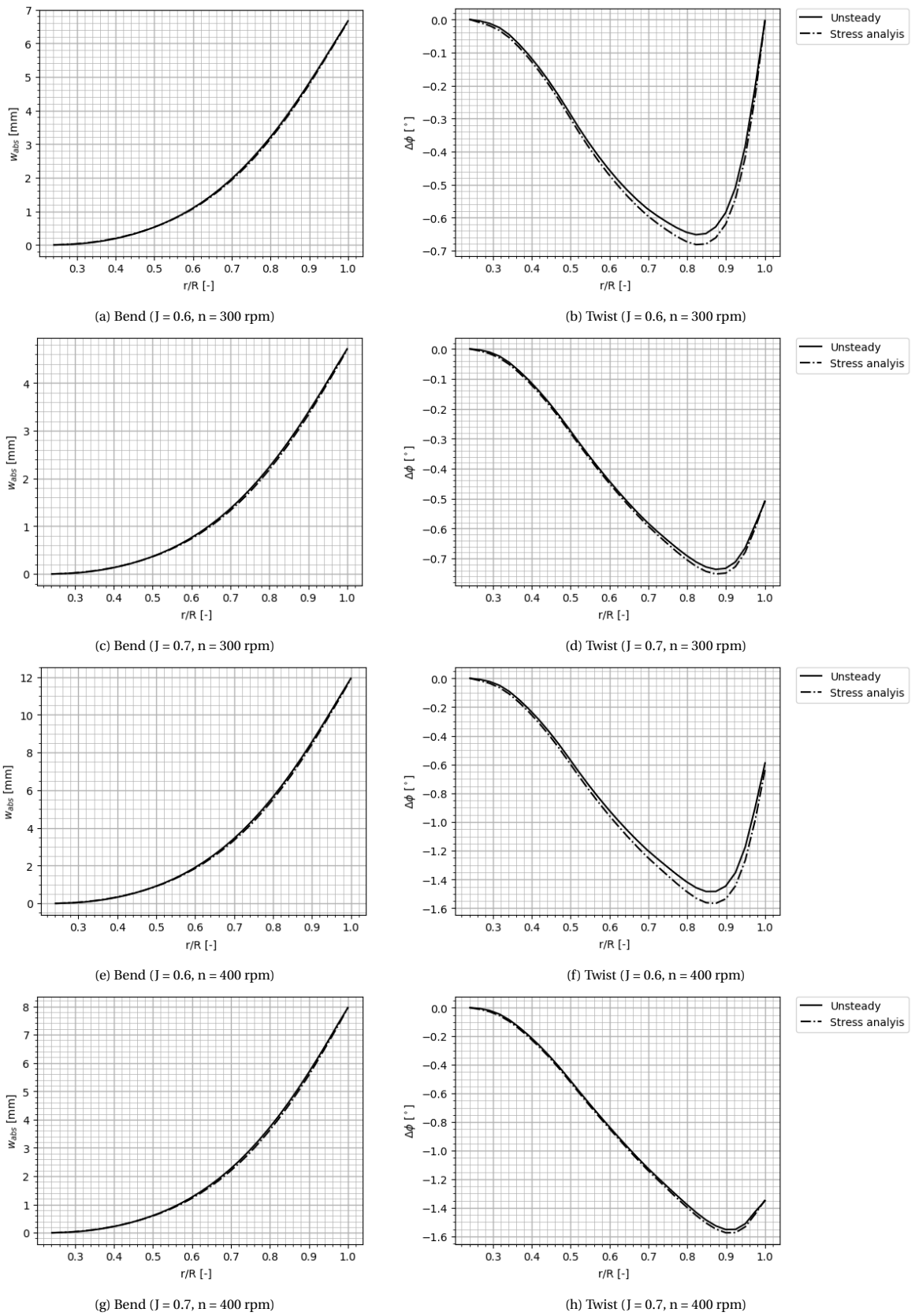


Figure 3.26: Comparison unsteady FSI and Stress analysis (Sikablock M700, Open Water)

### 3.6.2. Epoxy

The simulations for epoxy have been performed for both open water, as well as wakefield conditions. For open water conditions the results have also been compared with the steady FSI analysis.

#### Open water:

Next, the open water results for epoxy are presented. In this case, a comparison is made for the steady FSI, unsteady FSI, and the stress analysis results. For these simulations, also the camber deformation is given, though only for the steady and unsteady analysis. Like for the Sikablock material, the stress analysis agrees well with the unsteady FSI results. The difference between steady and unsteady solver is much more significant. In general, the unsteady solver predicts larger deformations than the steady FSI.

Starting with the solutions for  $J = 0.6$ , a smaller twist deformation is predicted by the steady FSI module. A plausible explanation for these deviations arises from the aforementioned problems, viz., small changes in pressure distribution for steady and unsteady solvers, and the pressure interpolation steps in the steady FSI. Consequentially, less twist deformation should lead to an over prediction in bend, although the bend deformation is smaller. Also at 900 rpm a smaller bend is predicted in the steady FSI. The over predictions may be explained by the differences in camber deformation, but also by the linearity assumption in the unsteady FSI.

For the case with a high advance ratio ( $J = 0.73$ ), a larger error between both solvers is observed. This can most likely be explained by the combination of a high rpm and advance ratio. The high shaft velocity causes large twist deformations, which decreases the  $P/D$  such, that the effective thrust coefficient approaches zero ( $k_t < 0.05$ ). As discussed earlier, panel methods become less reliable at high advance ratios i.e. low thrust coefficients. This led to a rather unstable solution in both cases, hence it can be concluded that neither provides a reliable solution at a high advance ratio in combination with a high shaft velocity.

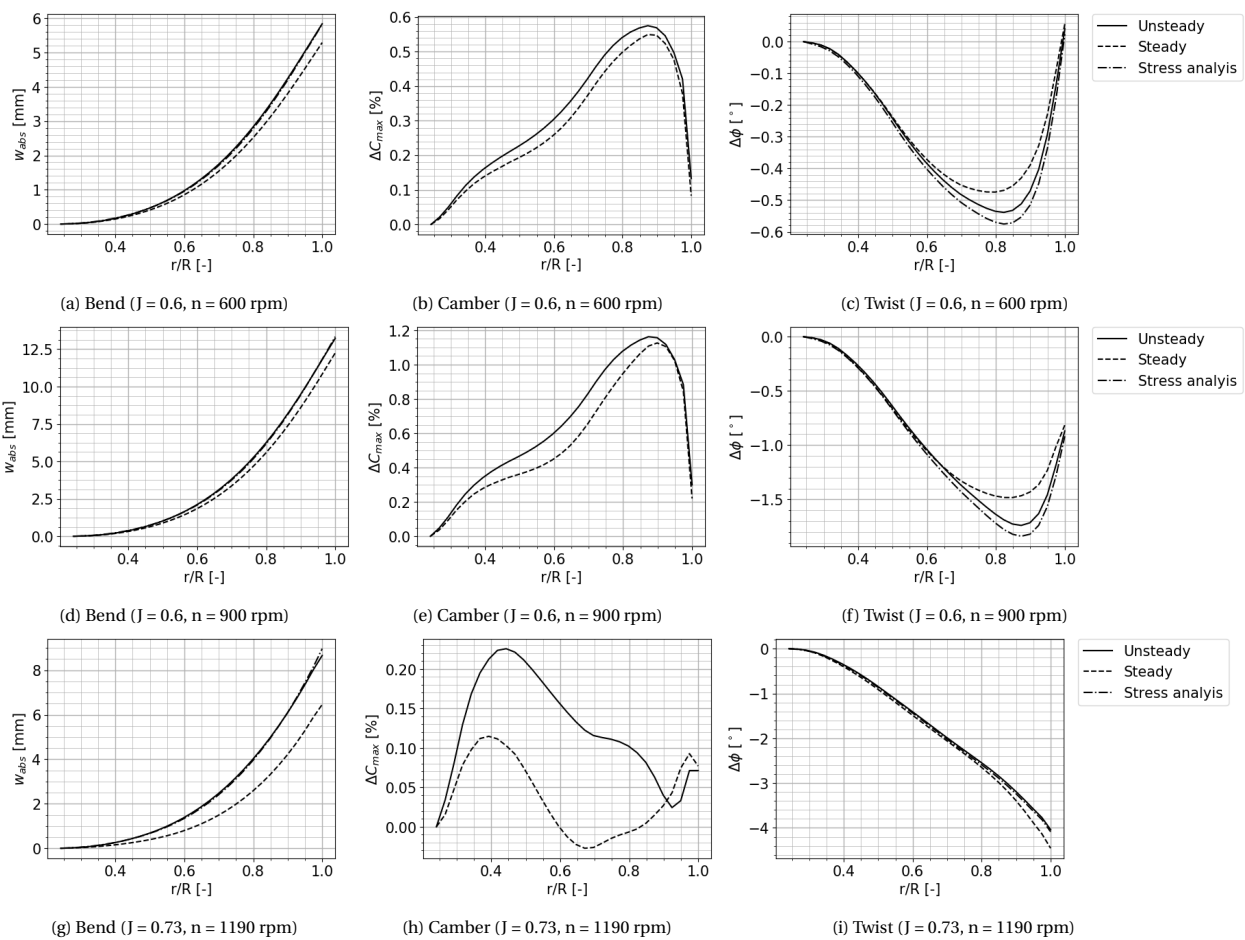


Figure 3.27: Comparison unsteady FSI, Stress and steady analysis (Epoxy, Open Water)

### Wakefield conditions:

Next, the results of the unsteady wakefield computations are shown. This particular condition has already been compared with the quasi-static solution, which did not fully capture the response of the blade. Hence the results are compared to the stress analysis only. Figure 3.28g displays the convergence of the stress analysis, which is performed in the time domain. The stress analysis suffers from startup problems, hence several revolutions have to be performed before reaching convergence. This emphasizes the benefit of modeling in the frequency domain, where these startup effects do not occur, saving significant computational time. Looking into the last revolution only, some fluctuation remains in the stress analysis which may be a cause of the critical damping ratio, which is set fixed at 2%. However, increasing this value may lead to incorrectly capturing the deflection when the excitation frequency is nearing a mode shape's natural frequency. The other sub figures in figure 3.28 display a comparison for the last revolution at a number of angular blade positions, whereas the tip displacement is evaluated over the entire revolution. Though the differences are more significant than for open water conditions, they still show good agreement.

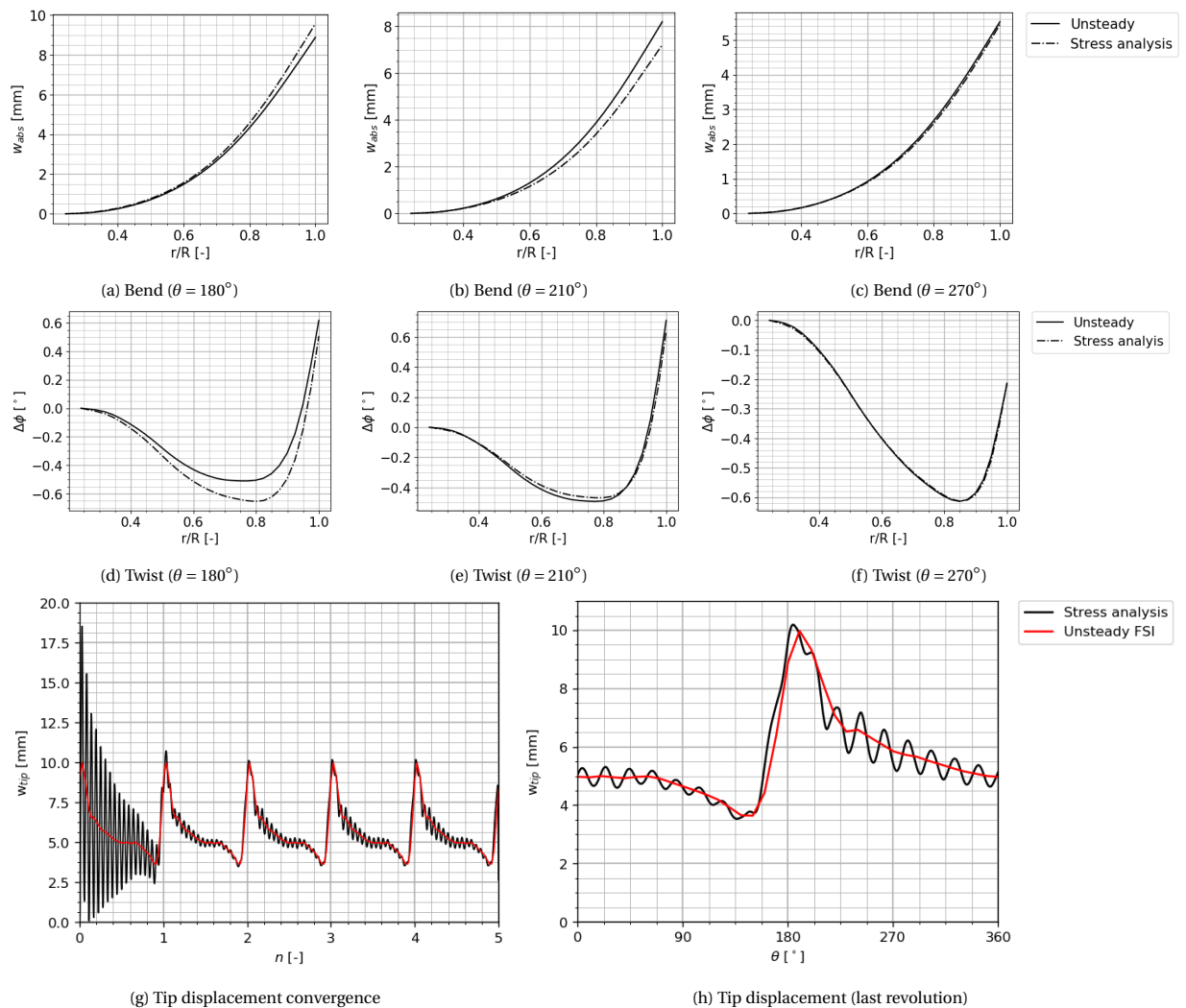


Figure 3.28: Comparison unsteady FSI and Stress (Epoxy, Wakefield)

### 3.6.3. Glass fiber reinforced epoxy:

To evaluate the ComPropApp’s capability of modeling composites, two computations have been performed for a glass fiber reinforced epoxy. Both composites consist of 34 plies, one with alternating orientations between 0° and 90°, the other between 0° and 30°. These angles are measured with respect to the radial line through the blade, in the plane created with the radial and tangential line of the blade. The ply properties are shown in table 3.10. The composite with alternating plies between 0° and 90° still has some isotropic behavior ( $E_1 = E_2$ ), since the plies are oriented perpendicular to each other and are present in the same quantity. Hence a second composite was evaluated, in which case  $E_1 > E_2$ .

$E_1$	$E_2$	$E_3$	$\nu_{12}$	$\nu_{23}$	$\nu_{31}$	$G_{12}$	$G_{23}$	$G_{31}$
44.1	9.93	9.93	0.310	0.229	0.0677	3.28	2.38	3.28

Table 3.10: Ply properties glass reinforced epoxy

The results of the computations are displayed in 3.29. A similar pattern as for epoxy is observed for twist and bend deformation in this case, both predicted higher for the unsteady FSI. The computed deformations by applying a modal analysis are generally higher than for the non-linear static analysis. Though these deformations are of significantly smaller magnitude than for epoxy, a relatively large difference remains. This led to conclude that the difference does not occur as a result of non-linear load application. If that were the case the relative difference between both solvers should decrease for smaller deflections. Interestingly, the camber deformation agrees much better than for an isotropic material. Also, adapting the composite lay-up yields reasonable results. The results show that the [0°/30°] has a slightly higher bend stiffness, which can be expected when more fibers are oriented more in the longitudinal material direction.

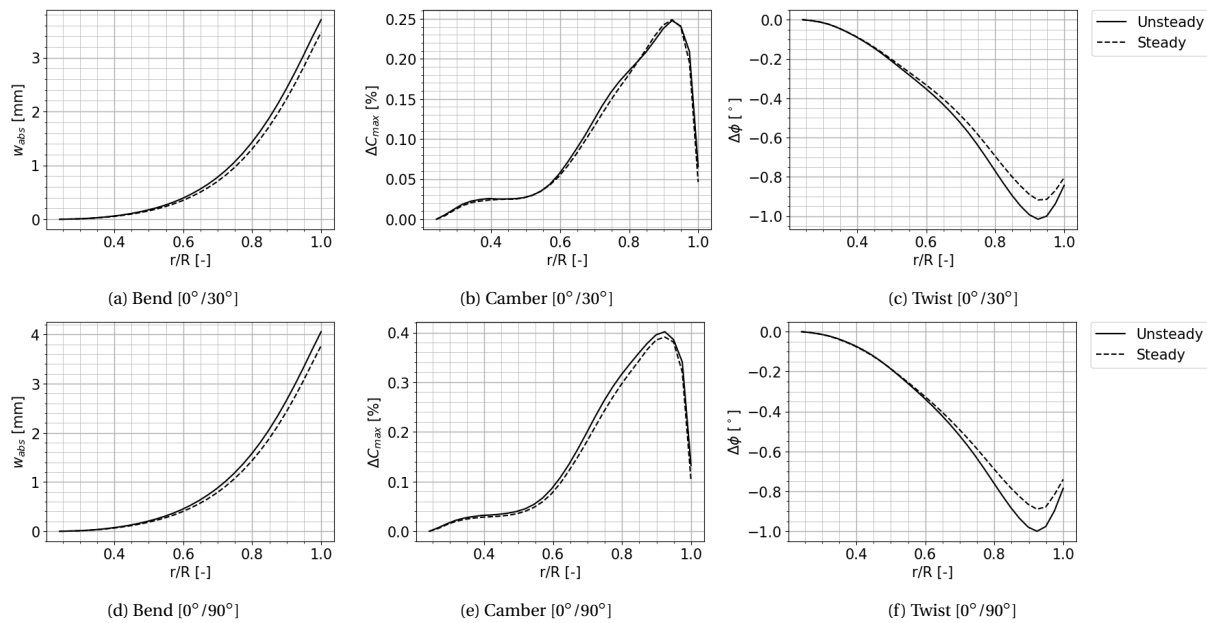


Figure 3.29: Comparison unsteady FSI and steady FSI (Composite, Open Water,  $J = 0.57$ ,  $n = 1025$ )

### 3.6.4. Bronze:

A computation with a bronze propeller was performed, the purpose of which was to determine the influence of slight changes in the panel grid. The main changes expected to occur in the panel grid is a loss of refinement in the root and tip region of the blade, since the current version of PROPART (P4C) applies a constant grid distribution along the radius. Figure 3.31 displays the consequence of the constant radial distribution on the tip resolution. As the deformation of the bronze propeller should be near zero, the last BEM computation in the ComPropApp should yield the same results as an undeformed BEM computation with a grid designed following the Provis guidelines (section 3.2.2). The properties used for bronze are displayed in table 3.11.

Parameter	Value
Material density	8800 $kg/m^3$
Young's modulus	110 $GPa$
Poisson's ratio	0.341
Flexural strength	450 $MPa$

Table 3.11: Bronze properties

An unsteady computation was executed in a wakefield, after which the thrust coefficient and torque coefficient were compared with a Provis generated grid. The results are shown in figure 3.30. Though small (maximum difference < 1.5%), this adds an uncertainty factor to the ComPropApp results. A recommended change is therefore to adjust the PROPART toolbox, such that it generates a similar grid as Provis does.

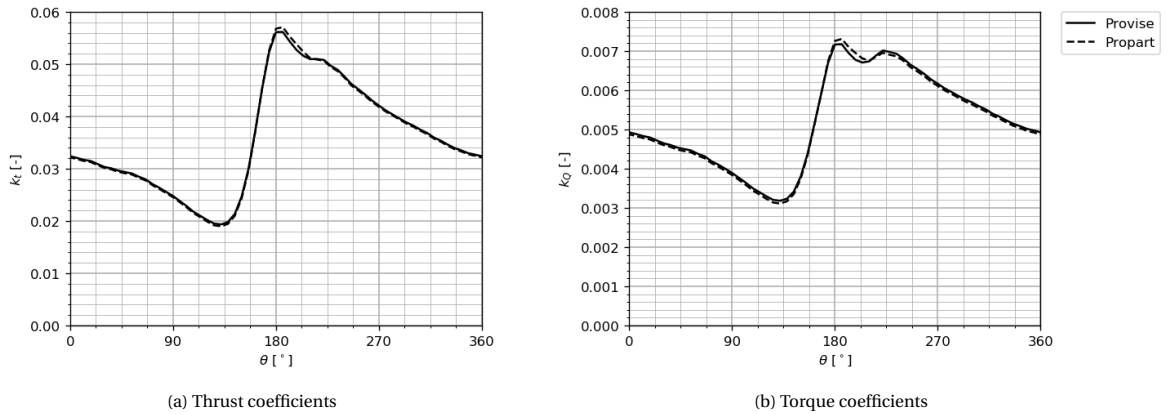


Figure 3.30: PROCAL results prior and after ComPropApp simulations (Bronze, wakefield,  $J = 0.6$ ,  $n = 1000$  rpm)

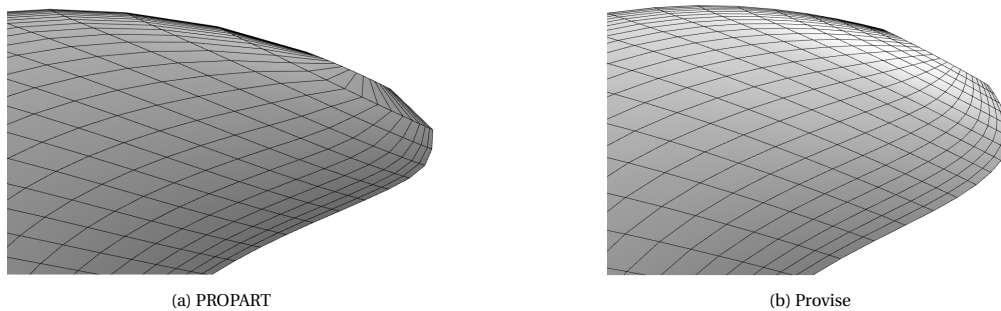


Figure 3.31: Comparison BEM grids ( $30 \times 30$ )

### 3.7. Conclusions

In this chapter, a verification study on the BEM-FEM coupling software has been presented. In order to ensure that the individual solvers applied in the ComPropApp would yield reliable results, they have first been treated separately. For the FE and BE methods, grid studies were performed. PROCAL simulations were executed for the undeformed propeller geometry, and compared with experimental results. The comparison showed that BE methods are most accurate for intermediate advance ratios ( $0.3 < J < 0.7$  for  $P/D = 0.8$ ). The loss of accuracy at  $J > 0.7$  can be explained by the increasingly dominant viscous forces, for which empiric adjustments are applied in PROCAL. For  $J < 0.3$  inaccuracies may occur due to stronger leading edge vortex separation, which is not captured by BEM software.

The initial phase of the verification has been performed with the aid of simplified analytical cases, and manually performing procedures followed in the ComPropApp as a sanity check to locate any major errors. Furthermore, the steady and unsteady solution methods were compared in open water conditions for which they are both valid. This led to the discovery of a number of defects in the software. The following main problems have been encountered in the process:

- Stress analysis: Initially applied for one revolution only, but due to startup phenomena in the time-domain, this is now a user defined parameter set to 5 revolutions as standard.
- PROPART Toolbox: Initially, the first PROCAL simulation was performed with a Provis generated panel grid, whereas the deformed blade panel grid with the PROPART Toolbox (Points2Prop) had a significantly different panel distribution. Since this changed the effective load application, a consistent panel distribution was required. As a solution, the panel grid is no longer generated by the user. Instead, the grid is generated directly with an updated PROPART toolbox (Propart4Comprop) prior to the first revolution.
- Limited applicability of the steady FSI: The non-linear structural solver in VAST appears to yield invalid results for thrust values below 250 N. As this problem lies with the VAST software, it could not be resolved (thus far).
- Minor programming errors: E.g. Communication problems between the ComPropApp and Trident due to input file formats, Reading composite properties in the unsteady FSI, etc. These errors have been resolved.

The validity of the (quasi-) steady FSI was evaluated for a number of different conditions. As it has the benefit of computational simplicity, it was of interest to know for which conditions it may be sufficient to apply this method. It was found that for slow fluctuations in the effective flow direction (oblique wake), the magnitude of bend deformation was predicted well, but excluding the blade vibration velocities in the BEM computations led to a failure of capturing the response delay in bend and twist deformation accurately. For higher fluctuations (representative wakefield), the deviations with respect to the unsteady FSI increased as a result of the increasing importance of the structural dynamics. Therefore, the steady FSI can mainly be utilized for open water computations. However, when only the order of deformation size is required, for instance in preparing test conditions, the steady FSI can suffice also for non-uniform flow conditions.

The assumption of geometric linearization was verified, by applying a load in increments with the non-linear structural solver in VAST. It was found that for  $w_{tip}/D_p < 0.03$ , the deformations can be considered as linear.

Finalizing the verification, the ComPropApp with the applied corrections has been used to compute a total of 11 different operating conditions. The variables in these conditions were: flow velocity, advance ratio, (an)isotropic material properties and wake conditions. After observing the results of these computations, the following conclusions were drawn:

1. The unsteady FSI results for open water agree well with the stress analysis ( $\epsilon_{w,tip} < 1\%$ ,  $\epsilon_{\Delta\phi_{0.7}} < 5\%$ ). Both methods apply a modal analysis, with the main difference being the Fourier analysis applied in the unsteady FSI. This suggests that the Fourier analysis is being applied correctly, although for open water conditions the average Fourier component is applied.
2. The unsteady FSI results for wakefield conditions are comparable with the stress analysis results, though the stress analysis which is applied in the time domain does not converge perfectly ( $\epsilon_{w,tip}^{max} < 10\%$ ,  $\epsilon_{\Delta\phi_{0.7}}^{max} < 25\%$ ). The convergence may be improved by increasing the damping, though this may lead

to the failure to capture a modal response when it experiences an excitation near the natural frequency. Therefore it is recommended to adopt the damping ratio as a user defined variable. Nonetheless, based on these results it can be assumed that the Fourier analysis is applied correctly.

3. Open water conditions with various material properties and flow conditions show the same trend in the difference between steady and unsteady solutions. The unsteady FSI estimates approximately 10 % more deformation than the steady FSI. The differences in computed pressures, and thereby forces is insufficient to explain this overestimate. Though it can not be attributed to non-linearity of the structural response, it is assumed that this error originates from the different structural solution methods (linear modal analysis versus non-linear static). In addition, the steady FSI does not include centrifugal forces.
4. The geometric interpolations performed by the PROPART toolbox, increase the BEM discretization error by as much as 1.5%. Hence, for future purposes it is advised to adjust the PROPART such that it generates a panel grid according to the Prowise guidelines.

# 4

## Experiments

### 4.1. Introduction

With the ComPropApp verified, it can be utilized to determine the operating conditions for the experiments. This chapter initially treats the preparations performed before the tests took place. Initially, the uncertainties expected in the testing conditions, and also the measurements are discussed. Then, in order to define the conditions, computations were performed in several different operational conditions, i.e. varying advance ratios. For several fixed advance ratios, the shaft velocity was varied in the ComPropApp. The goal of initially determining experimental conditions is to obtain deflections large enough to be measured accurately whilst remaining well within the elastic regime. Once a number of open water tests were defined, a similar procedure was followed to determine the velocities in the wakefield that can be generated in the tunnel. With a selection of conditions made, tests were carried out in the cavitation tunnel for open water, as well as the generated wake. Finally, the results of the open water tests are compared in detail with the computations in order to validate the software.

### 4.2. Experimental setup

The experiments have taken place in the cavitation tunnel at MARIN. A propeller has been mounted inside the tunnel where the shaft velocity and stream velocity are specified by the user. The propeller shaft is connected to an encoder, which sends 360 impulse signals per revolution. A selection of these 360 impulse signals can be used to trigger strobe lights and cameras. The strobe lights illuminate the propeller at the moment an impulse comes through, such that the camera can capture the propeller at the same angular position(s) for each revolution. The experiments are conducted with the four bladed Wageningen C4-40 propeller, manufactured from the Sikablock-M700 polyurethane material. The cavitation tunnel was initially used for open water tests, after which tests in wakefield conditions were performed. A wakefield can be generated with a body placed upstream of the propeller, the shape of this body was determined with CFD simulations to generate a representative ship wakefield.

**Measurement technique** To measure the deformations of the propeller, the optical method Digital Image Correlation (DIC) is applied. It works by comparing digital photos of the propeller in different deformation stages, by means of tracking a certain pattern applied on the surface. This pattern is a randomly distributed high contrast speckle pattern, which can be painted on the propeller surface. For a sufficiently accurate DIC measurement, all speckles should have a distinctive size. DIC is applicable with one or two cameras, where the technique with one camera is limited to the measurement of only in-plane deformations. Therefore the choice is made to use two cameras aimed at the propeller from different angles to capture the deformation in three dimensions. Figure 4.1 displays a DIC measurement performed on the Sikablock propeller. It shows the deformed propeller blades at the resolution of the cameras ( $1024 \times 1280$ ).

**Uncertainties** The DIC measuring technique is an accurate method, with measuring errors expected of about  $50 \mu m$ . This has been determined in [20], where the different uncertainty mechanisms that may play a role were investigated. The experimental uncertainties consist of precision and systematic errors. Precision

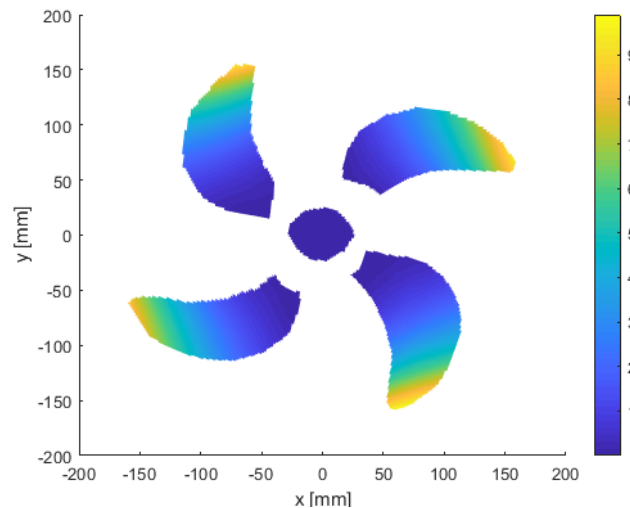


Figure 4.1: Absolute deflection measured with DIC ( $n = 400$  rpm,  $J = 0.6$ )

errors can be mitigated by time averaging the captured deformation over time. Deformations as a result of high frequency blade vibrations, and possible bubbles or particles in the water are filtered out by means of image averaging over several revolutions. The same holds for revolution speed, torque and flow speed. A small precision error remains for the camera measurements due to the contraction and expansion of the cavitation tunnel as a result of the flow velocity. This error was measured at  $20 \mu m$ . The systematic error is assumed at  $30 \mu m$ , based on measurements on blade response at the root, where normally zero deformation would be expected.

On top of the measuring uncertainties, the modelling accuracy should be taken into account. Different mechanisms are responsible for uncertainties in the model, listed below are those related to incorrect conditions for the comparison:

1. Fluid model limitations.
2. Structural model limitations.
3. Geometry uncertainties.
4. Velocity distribution errors in wakefield conditions
5. Laminar flow conditions

#### Fluid model limitations:

In the BEM model, the cavitation tunnel walls are not modelled though they will impact the flow slightly. To compensate for this inaccuracy a correction can be applied to the free stream velocity, known as the Glauert Correction [1]. Also, as discussed in section 3.4.3, the BEM is most accurate at intermediate advance ratios. Hence the aim was to perform experiments in the range  $0.4 < J < 0.7$ .

#### Structural model limitations:

Structural model limitations could be the case when the material properties as given by the manufacturer deviate from the actual properties. To overcome this problem, measurements have been performed on the propeller material to define the exact properties. The result of these measurements yielded a significantly lower Young's modulus, viz., 800 MPa compared to the 1000 MPa indicated by the manufacturer. The initial computations were performed for the measured properties. As these showed over estimates for the deflections, it has been discussed whether the measurements are a decent representation of the actual material properties. The measurements were performed on a material sample, hence it does not ensure that the propeller has similar properties. While the material is isotropic at a particular point, it may not have a uniform stiffness distribution throughout the material. As a result, one can at least assume that the model propeller has a Young's modulus between 800 MPa and 1000 MPa. Therefore computations were also performed for the stiffer material.

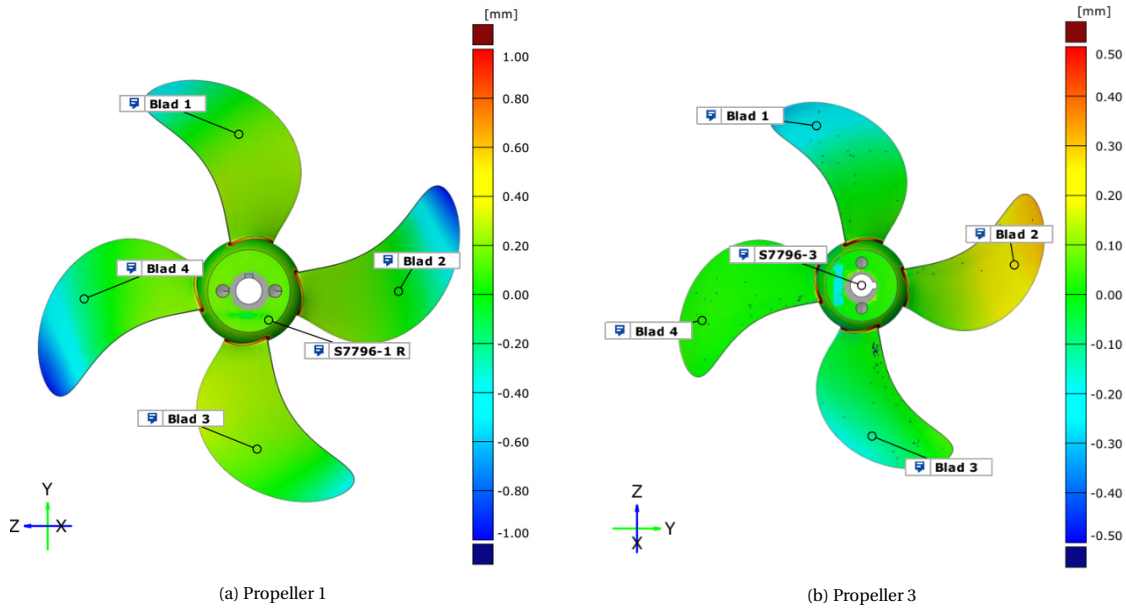


Figure 4.2: 3D measurements Sikablock propeller

**Geometric uncertainties:**

The discretized model for the simulations is based on the same three dimensional model as the one used for preparing the CNC milling machine. There are undoubtedly some inaccuracies in the machining process of the propeller. To find the magnitude of this error, a three dimensional scan of the machined propeller model was executed. Three models were machined, of which two have been used in the experiments. Figure 4.2b displays the measurements of the unused propeller, and figure 4.2a measurements of one which has been used. Note that the used propeller has much more significant deformations than the unused one. Initially, it was assumed that the propeller had undergone plastic deformation during the experiments. However, a scan of the third model was performed showing deformations up to 1 mm in the opposite direction. This propeller was also used in the experiments, but much less than the other (80 % of the tests were performed with the propeller shown in figure 4.2a). In addition, this propeller had undergone stresses in the same direction, ruling out the possibility that plastic deformation was the main cause of the different geometries. Therefore, it is assumed that coincidentally the unused propeller was machined most accurately, but actually, the machining process has an uncertainty in the tip of  $\pm 1$  mm. This large error in the machining process is likely caused by the high flexibility of the blades, which led to deformations in the machining process.

**Velocity distribution errors in wakefield conditions:**

While there are measurements available of the velocity distribution inside the tunnel with the wake generator installed, the lowest velocity where measurements were performed is 4 m/s. This is significantly higher than the Sikablock propeller could resist ( $V < 2$  m/s), therefore no reliable data is available for the actual wakefield. Figure 4.3 illustrates the severity of this problem. It can be seen that the variation in velocity rapidly increases

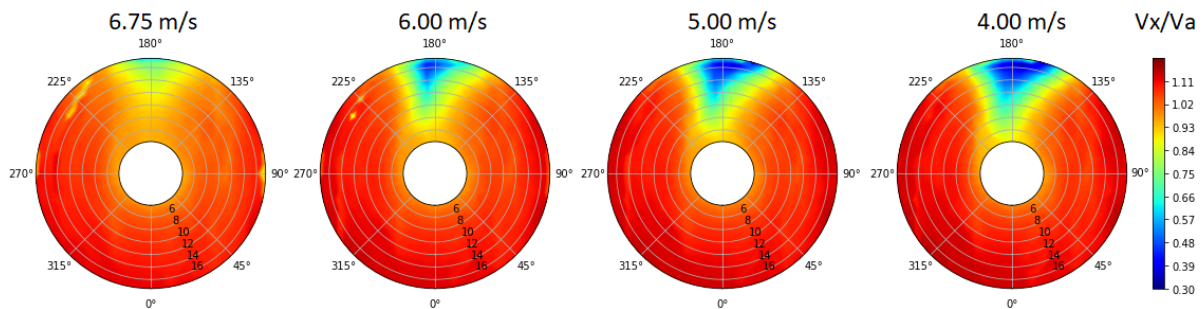


Figure 4.3: Comparison of measured wakefield in different flow velocities

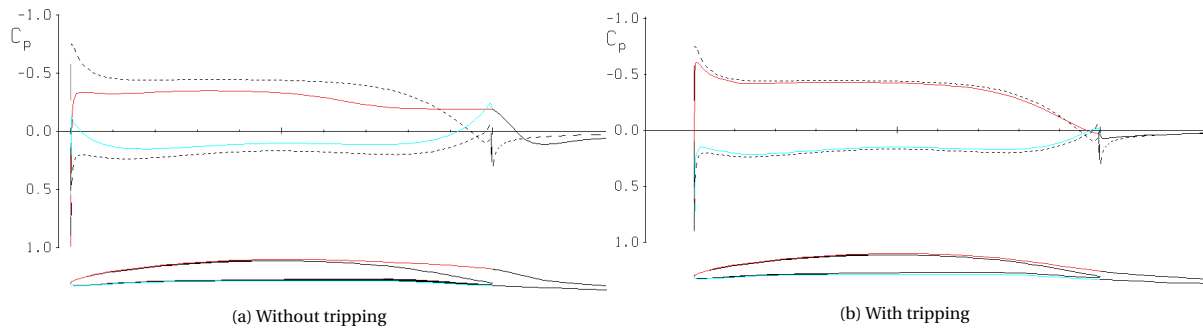


Figure 4.4: XFOIL simulation at 0.7R ( $Re = 10^5$ )

with decreasing tunnel flow velocities. To determine the extent of this problem, a Reynolds Averaged Navier Stokes (RANS) simulation was performed for a flow at 1.5 m/s. The results of these computations have shown flow separation effects near the tunnel walls, creating a very unstable flow field.

#### Laminar flow conditions:

At low Reynolds numbers, it can be expected that the flow may reach laminar conditions at some positions of the blade. To mitigate these effects, tripping can be applied. Tripping is creating a roughness to the surface, e.g. with sand grains, to prevent uncontrolled laminar flow from occurring. Prior to the experiment, a two dimensional XFOIL simulation was performed on 70% of the radius for  $Re = 10^5$ . XFOIL is a program developed to design and analyze isolated airfoils. This is done to determine whether flow separation would occur. Figure 4.4a shows the pressure distribution as obtained by XFOIL. The dotted lines display the results given by PROCAL, where the solid lines display the actual pressure distribution when viscous effects are taken into account. The figure shows that flow separation does indeed occur at the trailing edge. To prevent flow separation during the experiments, tripping is applied directly behind the leading edge. When applied, the flow separation is largely avoided, as is displayed in figure 4.4b, thus yielding the possibility of performing experiments at lower flow or shaft velocities.

### 4.3. Defining conditions

To define the operating conditions for the experiment, the properties of the polyurethane have been determined with measurements performed at DRDC. These properties are displayed in table 3.9. This is a much more flexible material than epoxy, hence the propeller will operate at a significantly lower shaft velocity.

#### 4.3.1. Deformation size

To determine a suitable range for the testing deformations, a number of factors should be considered. The deformations have to be large enough such that they can be accurately measured, the deformations should remain within the linear regime and the material should remain well within the boundaries of failure. On top of that, the flow velocities have a lower limit as well to ensure a turbulent flow regime. The measurement error was estimated at  $50 \mu m$ , that is, the bending measurement error. The error for the twist is determined differently, as the twist is determined with the difference between the leading edge and trailing edge of a local cross section (equation (3.2)). Assuming the precision error is approximately constant in a specific condition, it should not influence the twist prediction. The remainder is the systematic error of  $30 \mu m$ , which translates to a twist prediction error of  $0.1^\circ - 0.3^\circ$  for this propeller, depending on the radial position. To obtain measurement errors below 1% a bend deflection of  $5 mm$  is required.

To find the failure limit for the deformations, a static analysis on the maximum bending deformation before failure was performed. At a flexural strength of 26 MPa, the material is only expected to fail at tip deformations above 70 mm, which is far outside of the testing conditions.

The tunnel flow velocity is not only limited by the maximum propeller deformations, in fact, it also has a lower limit, since the experiments require a certain minimal Reynolds number to avoid laminar flow.

Considering the factors mentioned above, the choice was made to test at tip deformations in the range 5-10 mm. This way sufficiently accurate measurements can be obtained, whilst remaining in the linear regime, well within the failure limits of the material.

### 4.3.2. Tip deformation matrix

A number of open water computations are performed with varying shaft velocities and advance ratios. The computed tip deflections are displayed in table 4.1. As a result of the low Young's modulus of the polyurethane, the propeller lift has a strong dependency on the advance ratio and rotational velocity. Since the measured deflections are rather large, significant pitch changes but also camber changes were observed. Since pitch and camber deformations increase with shaft velocity and advance ratio, the deformations at high advance ratios and high revolution speed are expected to be less accurate. Due to the aforementioned linearity assumption in the load application, predicted tip deflections above 10 mm are considered as less accurate. Finally, as a result of laminar flow effects the BEM software is expected to be more accurate at higher shaft velocities. When a shaft velocity of  $n > 300$  rpm is used,  $Re_{0.7} > 200,000$ , and  $Re_{root} > 100,000$ . Taking all these factors into account, led to conclude that the tip deflections colored in red are less suitable testing conditions.

		Shaft Velocities [rpm]				
		250	300	350	400	450
Advance ratios [-]	0.55	5.77	8.22	11.0	13.8	16.5
	0.60	4.93	7.00	9.19	11.3	13.3
	0.65	4.13	5.81	7.44	8.95	10.2
	0.70	3.32	4.54	5.68	6.39	7.04
	0.75	2.54	3.33	3.91	4.17	3.83

Table 4.1: Open water tip deflections [mm]

The adverse effect of the relatively large twist deformations at the blade tip, is that it increases the sensitivity to small deviations in the flow velocity, i.e. non-uniform flow conditions. This may cause unstable behavior of the propeller blades, hence the testing conditions were built up carefully to prevent failure of the material. To determine the wakefield conditions, similar criteria for the deformation magnitude was applied, considering the average tip deflection. Initially, these calculations were performed for an effective wakefield, computed for a propeller rotating at 1300 rpm in a 6.75 m/s wakefield of the cavitation tunnel. Tables 4.2 and 4.3 display the computed average and maximum tip deflection respectively.

		Shaft Velocities [rpm]			
		250	300	350	400
Advance ratios [-]	0.55	4.64	7.01	9.62	12.4
	0.60	4.12	5.94	8.04	10.4
	0.65	3.51	4.99	6.61	8.77
	0.70	2.78	3.88	5.02	6.17

Table 4.2: Wakefield average tip deflections [mm]

		Shaft Velocities [rpm]			
		250	300	350	400
Advance ratios [-]	0.55	6.30	9.50	13.3	15.6
	0.60	6.11	8.78	11.5	16.7
	0.65	5.92	8.47	11.1	15.9
	0.70	5.11	7.28	9.37	14.7

Table 4.3: Wakefield maximum tip deflections [mm]

## 4.4. Results

### 4.4.1. Open Water

The results of the open water tests were compared with the unsteady FSI computations. These are shown in figure 4.5, where bend deflection is compared for a number of load conditions. The tests were performed at slightly higher load conditions than initially determined with the numerical computations, which is a result of the deformations being lower than predicted. The cause of this overestimate, was expected to be a consequence of the uncertainties in the material specifications. The initial computations were performed for a Young's modulus of 800 MPa, though the actual properties may vary anywhere between 800 and 1000 MPa. The line of the computations denotes the computation results for  $E = 900$  MPa. The shaded area for the computations represents the uncertainty region, which is mainly a consequence of the material Young's modulus. The red line represents the average deflection of the four blades, the test uncertainty can be subdivided into uncertainties due to periodic fluctuations at each evaluated blade position, and the differences between the individual blades. The measuring uncertainty was considered as negligible for deformations of this magnitude. The standard deviation ( $\sigma$ ) of the periodic fluctuations was determined during the tests at 1 % of the measured deflection. The uncertainty plots include a  $\pm 3\sigma$  deviation of the measurement. Hence, the main factor for testing uncertainty is the difference between blades. A plausible explanation for this is the low accuracy obtained in the milling process, which causes an initial deflection, but also an initial twist altering the hydrodynamic properties. The result, a difference in tip deflections of  $\pm 20\%$ . It is not expected that these inaccuracies are a result of the low flow velocities, resulting in laminar flow conditions or flow separation from the tunnel walls. If that were the case the accuracy should improve as the tunnel speed increases, which it does not. The low flow velocities are therefore not considered as a dominant source of error in this case. The results shown in figure 4.5 show a reasonable resemblance, though it is a difficult comparison to make due to the many uncertainties in the experiments.

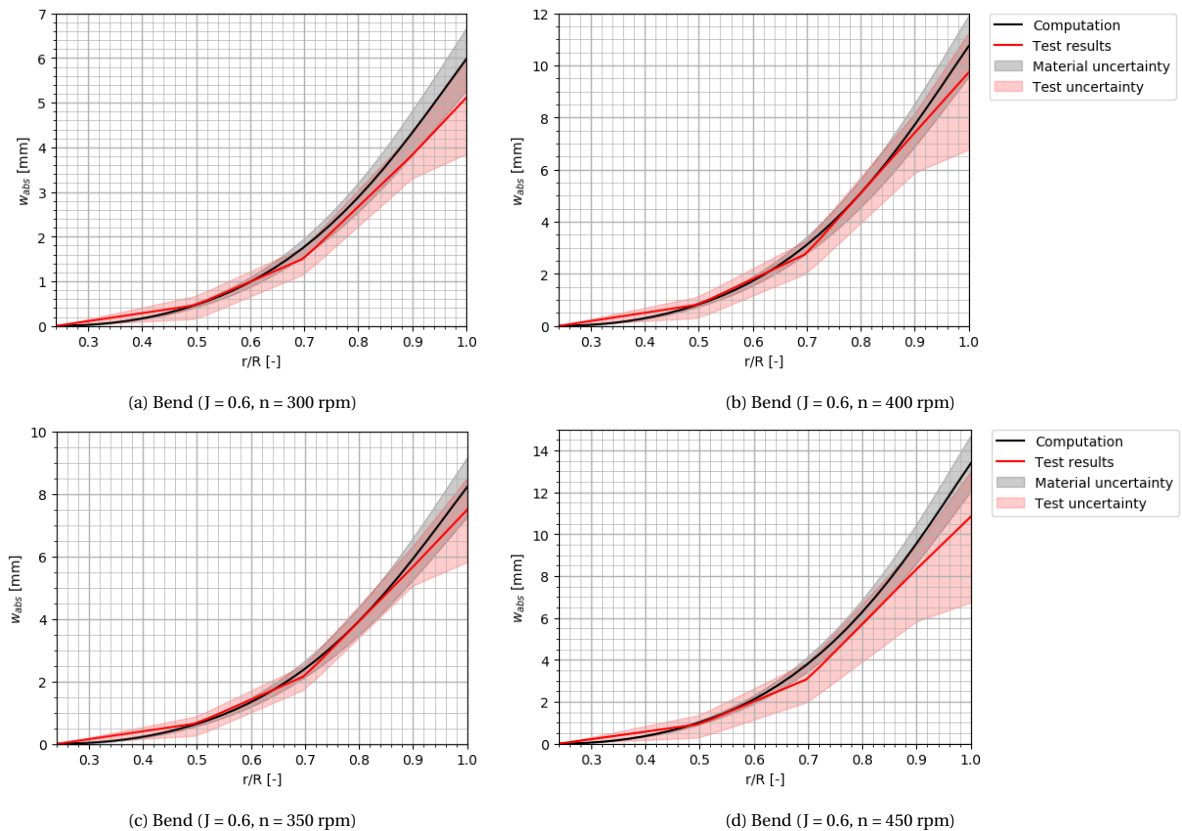


Figure 4.5: Comparison FSI computations with test results (Sikablock M700, Open Water)

#### 4.4.2. Wakefield Conditions

The tests with the wake generator placed in the cavitation tunnel have taken place at relatively high advance ratios ( $J = 0.7$ ) in comparison with the open water tests. This brings the advantage of introducing higher flow velocities inside the tunnel, to overcome the problems of flow separation along the tunnel walls. Nonetheless, the problem of flow separation persisted and the measurements yielded large periodic fluctuations in deformation. Therefore, statistic methods are required to determine a representative time average of the blade shapes. On top of that, a new wakefield needs to be computed for the experimental flow velocities by means of RANS solvers, which was already discovered to be a difficult task at these velocities. An alternative may be to utilize the thrust measurements in the tests (performed with a rigid propeller) in order to apply a correction to obtain the effective average velocity field. However, with regard to time, it was chosen not to include this in the study.

### 4.5. Conclusions

This chapter presents a validation of the ComPropApp software by means of a comparison with model scale tests. From this comparison between the measurements and computations, it can be concluded that the software can make a qualitatively comparable prediction of the deformations in open water testing conditions. That said, the Sikablock polyurethane used for the validation has brought several large uncertainties. While a material with this highly flexible behavior does reduce the relative measuring uncertainty by introducing larger deformations, it does present a number of drawbacks. The first of which is a reduction in machining accuracy as a result of the blades deforming during the milling process. This not only had a considerable effect on the undeformed propeller, but also on the measured deformations which are greatly influenced by the deviations in hydrodynamic properties of the undeformed blade. The other major uncertainty is the material elasticity modulus, where a sample was measured at 20 % below the one supplied by the manufacturer. These uncertainties reduce the reliability of the open water validation. For the wakefield conditions, an additional uncertainty in the flow field distribution was introduced as a result of the low flow velocities ( $V < 2$  m/s). Very unstable behavior was observed during the tests, which together with RANS simulations have led to conclude that the wakefield generated by the body in the cavitation tunnel causes flow separation, which cannot be neglected. As a result, the wakefield tests performed for the Sikablock are inconclusive and require further research to be done.



# 5

## Composite application

### 5.1. Introduction

Claimed benefits of composite propellers are higher efficiencies, reduced acoustic signatures, and mitigating cavitation. While cavitation clearly has an influence on acoustic signatures, it also induces pressure pulses on the ship hull. Hence, for structural and/or comfort reasons, there are certain guidelines for minimal clearance levels between hull and propeller. Mitigating cavitation can, therefore, result in lower clearances, creating the possibility to install a larger propeller. The increase of the propeller diameter can lead to higher efficiencies, since a lower shaft speed is required to deliver the same thrust, reducing axial losses. This can be explained by momentum theory, which states that the ideal efficiency of a propeller is defined as:

$$\eta_{ideal} = \frac{1}{1 + \frac{|v_{out}|}{|v_{\infty}|}} \quad (5.1)$$

where  $v_{out}$  is the velocity behind the propeller. From this relation, it can be derived that it is generally more efficient to accelerate a large fluid mass by a small amount than a small fluid mass by a large amount. It should be noted that even though the open water efficiency increases, the hull efficiency may be negatively influenced by the larger diameter, as well as by reducing clearance. Interestingly, it seems that cavitation plays an important role in both the efficiency and acoustic signatures, which is why it is undoubtedly an aspect to elaborate. The first section of this chapter describes the fundamentals of cavitation, and how flexible propellers have the potential to mitigate it. Subsequently, a material study is performed for the Wageningen C4-40 propeller based on the required deformations for cavitation inception.

### 5.2. Cavitation on marine propellers

As discussed earlier, the main driving principle by which a propeller generates thrust is the pressure difference between the suction and pressure side of the propeller. Once the pressure coefficient is low enough, water evaporates into gas, which evolves into vapor pockets, called cavities. When these cavities collapse they can cause hammer like impact loads on the blades. It is the collapse of the cavities that results in damages to the propeller blade surfaces that have been observed. Once a marine propeller blade is rotating in a ship wake, these hammer impacts will happen on a periodic i.e. once per blade passage basis, with the adverse consequence of generating large vibrations that are then transferred to the ship. There are several different cavitation phenomena that may occur with marine propellers. These are listed below, and displayed schematically in figure 5.1 [11].

- Sheet cavitation: Occurs when large suction side pressures are building up near the leading edge of the blade. It causes a sheet of bubbles covering the blade towards the trailing edge. This form of cavitation is largely dependent on the local angles of attack. When very unstable, for instance in a non-uniform wakefield, it can cause serious vibration problems and damages.
- Cloud cavitation: Typically found near the collapse region of sheet cavitation and may cause extreme damages and vibrations. Here large numbers of bubbles collapse simultaneously.

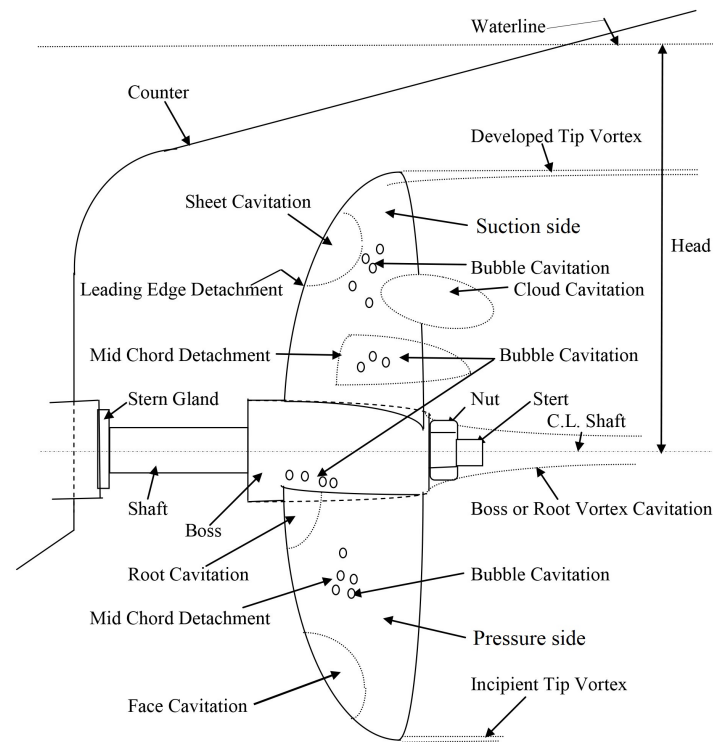


Figure 5.1: Several types of cavitation (altered from [11])

- **Face cavitation:** Occurs at the pressure side of the propeller and is usually a consequence of the pitch distribution along the radius, where negative angles of attack occur locally. This often occurs with controllable pitch propellers.
- **Tip vortex cavitation:** Caused by the low pressure areas in vortices shed near the tip, which arise as a consequence of the large pressure differences between pressure and suction side.
- **Bubble cavitation:** This generally occurs at the mid-chord section of the blade as a consequence of too much camber applied to the blade. It can be avoided by proper design of the cross sectional blade shape.
- **Root cavitation:** Quite uncommon on full scale, it usually occurs at high velocity and heavily loaded propellers. It is located on the suction side of the blade root area where it has maximum thickness.
- **Hub vortex cavitation:** A consequence of a high angle of incidence between the flow direction and the blade.
- **Supercavitation:** With supercavitation, a cavitation bubble is utilized to reduce skin friction along a body. Its application is mostly limited to very high speed submerged vessels, such as torpedoes, and lies outside the scope of this research.

When focusing on the application of flexible propellers, it has been observed that the blades experience bend and twist deformations [20]. This implies that of the cavitation types listed above, the most likely to be influenced are tip vortex cavitation, and sheet or face cavitation thus consequentially cloud cavitation, hence these types of cavitation are treated more elaborately.

### 5.2.1. Tip vortex cavitation

Tip vortices are an important occurrence with ship propellers, since the core of a vortex has a low pressure peak, which can cause cavitation. This type of cavitation is usually not erosive but it may be a source of noise emissions. Where noise emissions are clearly important for navy vessels, there is also an increased concern regarding the interference with marine life. Therefore the interest in reducing tip vortex cavitation is also rising for commercial shipping.

As mentioned earlier, tip vortices occur as a result of large pressure gradients between pressure and suction side of the blade. The cause of tip vortex cavitation can be described, be it at a very limited accuracy, with a two-dimensional vortex model to describe the local velocity field. In this model a vortex is considered, having all its vorticity concentrated in an infinitely small circle. The strength of the vortex can be described with  $\Gamma$ . When the circulation is constant across the radius, the tangential velocity can be described as:

$$V_t = \frac{\Gamma}{2\pi r} \quad (5.2)$$

This approximation is known as the Rankine vortex, and it shows that the tangential velocity component approaches infinity inside the core of the vortex. Physically this is not realistic, but it does indicate the cause of low pressure peaks inside the core. These low pressure peaks arise as a consequence of the centrifugal forces in the rotating flow [5].

### 5.2.2. Sheet cavitation

Sheet cavitation is a vapor region which, when relatively steady, seems almost fixed to a propeller blade. In this condition, the surface of the cavity can be considered as a free, impermeable surface.

**Leading edge** Since sheet cavitation occurs as a result of a strong low-pressure peak near the leading edge of the foil (two-dimensional cross section of the blade), its leading edge is usually near the leading edge of the foil. The surface of the cavity has a constant pressure, namely the vapor pressure. This has consequences for the streamlines at the beginning of the cavity shown in figure 5.2. This constant pressure implies that the streamlines of the cavity separate tangentially from the surface, which leads to a very thin cavity, thin enough for surface tension to become significant [6]. As a result, the leading edge of the cavity moves backward (point C in figure 5.2), with the distance between S and C depending on the surface tension between vapor and water. Viscosity causes the water in the light red area to circulate, which is very close to vapor pressure at this point. Surface tension can cause the pressure to drop slightly below the vapor pressure, which may cause a significant portion of the vapor production, although this is not proved. For propeller blade cross sections this distance between S and C is short, and the exact structure of the cavity's leading edge is not important [6].

**Cavity closure** Because the pressure inside the cavity is lower than its surroundings, the water streamlines always tend to curve towards the cavity surface. This causes the cavity to reattach to the foil, as displayed in figure 5.3, showing that the flow splits up in two directions. Part of the flow reattaches to the foil following the flow, the remainder travels upstream as a so-called re-entrant jet. The re-entrant jets cause the liquid to flow into the cavity which cannot be a steady process, otherwise, the cavity would simply be filled with water. Instead, the cavity is gradually filled with fluid until part of the cavity, in some cases, the entire cavity is shed from the foil which is known as cloud cavitation. Notable is that this unstable behavior occurs in steady flow conditions, although more violently under unsteady conditions.

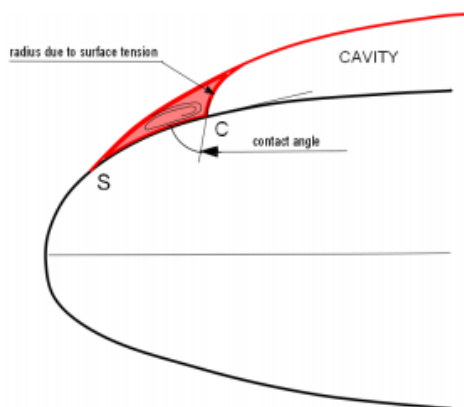


Figure 5.2: 2-D structure of sheet cavity (obtained from [6])

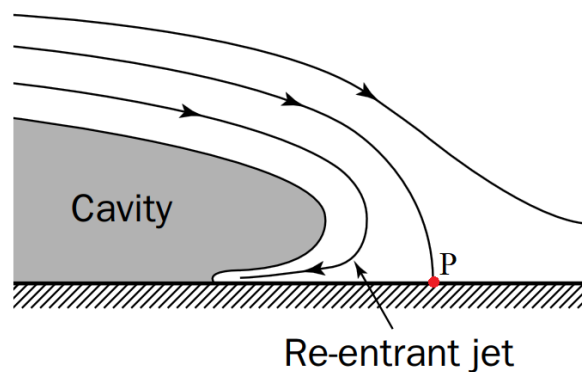


Figure 5.3: Re-entrant jet (adapted from [15])

### 5.2.3. Cloud cavitation

As mentioned, cloud cavitation (or shedding) is a violent unstable phenomenon that happens as a consequence of sheet cavitation. Generally, the shedding becomes less violent with shorter cavities, i.e. higher pressures, but remains present nevertheless [15]. Further, it is dependent on the steadiness of the flow in which the propeller is operating. In many steady flow conditions, the natural shedding does not cause erosion or vibrations. In such conditions the cavitation sheet varies little in time due to locally converging re-entrant flow, as a consequence, the natural shedding becomes almost periodical [6]. Non-uniform flow conditions significantly increase the aggressiveness of the shedding process. This is because the angles of attack are no longer constant, having the consequence that the length of the sheet cavity starts to grow and shrink throughout the revolution. Point P in figure 5.3 denotes the stagnation point of the flow behind the cavity. When the cavity grows, point P starts to move with the flow and the re-entrant jet starts to disappear. If point P would move at the same velocity of the flow, the pressure would equal vapor pressure such that no liquid re-enters the cavity. The opposite occurs when the cavity shrinks, in this case, the re-entrant flow becomes stronger. The re-entrant flow converges inside the cavity and collides, cutting through the cavity which ultimately causes a much more aggressive and violent shedding.

### 5.2.4. Cavitation number

To determine whether a system is vulnerable to cavitation, a non-dimensional cavitation number was set up. In order to define it, first a reference pressure close to where cavitation can be expected is determined. For a propeller, that would be the static pressure at the depth of the hub. The cavitation number is the ratio of the difference between reference ( $p_r$ ) and vapour pressure ( $p_v$ ) and the actual pressure difference ( $\Delta p$ ):

$$\sigma_v = \frac{p_r - p_v(T)}{\Delta p} = \frac{p_0 + \rho g h - p_v(T)}{\frac{1}{2} \rho |\mathbf{v}|^2} \quad (5.3)$$

The vapor pressure is a function of temperature (T) and the pressure difference depends on the local velocity (Bernoulli's law). The higher the cavitation number is, the less vulnerable the system is to cavitation. However, determining a suitable threshold is difficult since it depends on numerous factors, such as flow geometry, viscosity, surface tension, levels of turbulence, wall roughness, and fluid gas content [11]. It should be noted that the cavitation number is defined by dynamic parameters, hence scaling is difficult to apply, as it requires altering the reference pressure. Figure 5.4a displays a cavitation diagram. This diagram displays how a combination of the angle of attack and cavitation number can cause certain types of cavitation. It confirms that sheet cavitation on the suction side (back-side) occurs as a consequence of reaching too high angles of attack, as can happen when a propeller operates in a non-uniform flow field. Then the advance ratio is non-constant, which is related to the angle of attack by the following relation:

$$\alpha(r, \theta) = \phi(r, \theta) - \tan^{-1} \left( \frac{J(r, \theta) \cdot D}{2\pi r} \right) \quad (5.4)$$

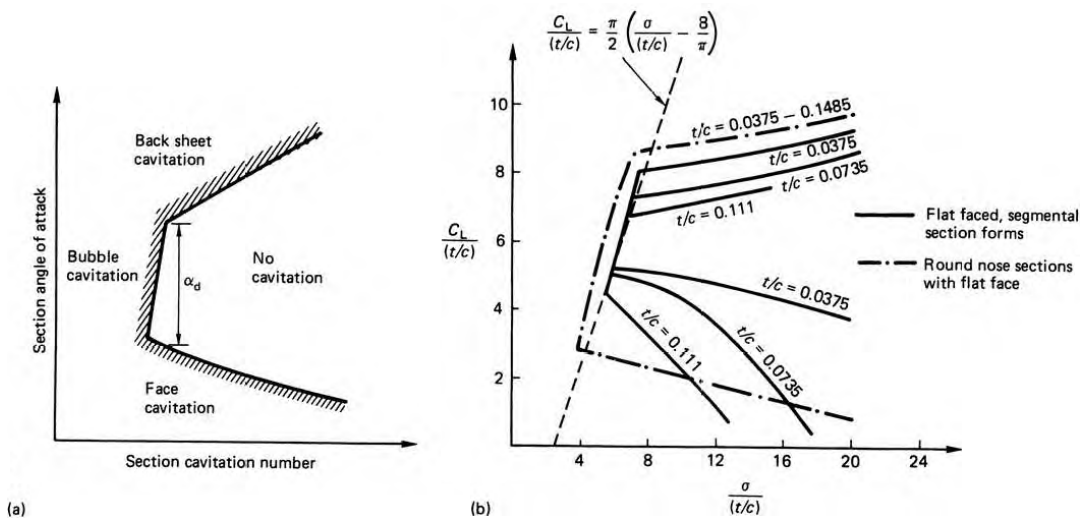


Figure 5.4: Cavitation diagrams, (a) basic features and (b) Walchner's foil experiments with flat-faced sections (obtained from [16])

with  $\alpha$  denoting the angle of attack,  $\phi$  the pitch angle. In the case of a flexible propeller in a non-uniform flow field,  $\theta$  and  $J$  are dependent on the radial ( $r$ ) and tangential ( $\theta$ ) position of the blade. Figure 5.4b displays an example of a cavitation diagram based on experimental results with flat-faced foils, with a number of thickness over chord-length ratios ( $t/c$ ).  $C_L$  denotes the lift coefficient of the foils that increases with the angle of attack.

### 5.2.5. Modelling of Cavitation

Cavitation models can be implemented in BEM software, as has been done in PROCAL, based on the model of Fine (1992) [13]. The modeling of cavitation occurs after a normal steady or unsteady flow simulation has been executed. It differs from the normal flow simulations since different boundary conditions apply. These boundary conditions are non-linear, hence an iterative procedure is required to define the cavity. In a cavitating flow, the dipole strength on the cavity is related to the dipole strength at the cavity detachment, determined by the dynamic boundary condition. The source strength on the cavity should be determined in order to compute the cavity thickness. The cavity thickness is then evaluated at the aft of the cavity where it should equal zero, an iterative procedure repeats itself until this criterion is met.

The kinematic boundary condition for cavitating flow states that any point on the cavity surface cannot leave this surface, i.e. it follows the streamlines:

$$\frac{D}{Dt} (s_3 - \eta(s_1, s_2, t)) = \left( \frac{\partial}{\partial t} + \mathbf{v} \cdot \nabla \right) (s_3 - \eta(s_1, s_2, t)) = 0 \quad (5.5)$$

Here  $\eta$  denotes the height of the cavity and  $s_1, s_2, \text{ and } s_3$  respectively represent the chordwise, spanwise and orthogonal direction with respect to the panel. The boundary condition is used to solve the cavity thickness with a central difference method to find the derivative in spanwise direction. The time derivative of the thickness is found by using an implicit method. The thickness is calculated by integrating in chord direction.

The dynamic boundary condition implies that the pressure at the surface of the cavity is equal to the vapour pressure. By applying Bernoulli's equation, the following equation holds:

$$|\mathbf{v}|^2 = |\mathbf{v}_\infty|^2 \sigma_v + |\mathbf{v}_0|^2 - 2gz - 2 \frac{\partial \phi}{\partial t} \quad (5.6)$$

Here  $z$  denotes the distance below the water surface, and  $\sigma_v$  the cavitation number.  $\mathbf{v}_0$  denotes the undisturbed velocity consisting of the free stream velocity and the velocity component due to blade rotation. Since it is expected that the flow is dominant in chordwise direction, the velocity vector is written as the potential derivative in direction  $s_1$ :

$$\frac{\partial \phi}{\partial s_1} = \sqrt{v_\infty^2 \sigma_v + |\mathbf{v}_0|^2 - 2gz - 2 \frac{\partial \phi}{\partial t} - v_{s_2^*}^2 - \mathbf{v}_0 \cdot \mathbf{e}_{s_1}} \quad (5.7)$$

where  $\mathbf{e}_{s_1}$  denotes the unit vector in chordwise direction and  $s_2^*$  the direction perpendicular to  $s_1$  and  $s_3$  ( $s_2^* = s_1 \times s_3$ ). The discrete potential can now be defined as:

$$\phi_{i,j} = \phi_{d,j} + \int_{S_d}^{S_i} \left\{ \sqrt{v_\infty^2 \sigma_v + |\mathbf{v}_0|^2 - 2gz - 2 \frac{\partial \phi}{\partial t} - v_{s_2^*}^2 - \mathbf{v}_0 \cdot \mathbf{e}_{s_1}} \right\} dS \quad (5.8)$$

Here  $\phi_{d,j}$  denotes the potential at the detachment location in chord direction at point  $j$  in spanwise direction. The potential value at the detachment location is established by interpolation from points ahead of the detachment panel, where cavitation not yet occurs.

### 5.2.6. Application to the Wageningen C4-40 series

In order to determine when the Wageningen C4-40 series is expected to experience cavitation, the non-dimensional cavitation boundaries shown in figure 5.4b have been defined for the propeller model. A number of BEM simulations have been performed at a constant advance ratio, varying the shaft velocity. As cavitation is usually a result of the non-uniform inflow, the wakefield as generated in the cavitation tunnel (figure 3.20) was taken as a reference. All BEM simulations were performed for cavitating and non-cavitating flow. This is because cavitation influences the local lift force, and it is of interest to what extent the undisturbed lift is related to cavitation occurrence.

Figure 5.5 displays the bucket diagram for points along the radius of the blade. These are the discretized radial points throughout one full revolution, i.e.  $N_j$  timesteps, where either sheet or face cavitation occurs. The bucket diagram gives a reasonable estimate of when and where to expect cavitation, the size of the dots is related to the cavity volume. A few minor cavities have been neglected in the determination of the cavitation boundaries. The diagram shows that both sheet and face cavitation starts to play a more significant role at increased shaft speed, and that the type of cavitation is dependent on the local advance ratio. At a low advance ratio, the relative angle of attack increases, consequentially the lift coefficient as well, leading to sheet cavitation. The opposite occurs at high advance ratios where local inflow angles may even become negative, yielding face cavitation. Face cavitation only occurs at 23 rps and above, as indicated in the diagrams. Figure C.1 in the appendix displays a Tecplot visualization of the cavities. The simulations display cavitation peaks near the expected angular positions. Since the lift is roughly proportional to the applied forces on the flexible propeller, one would expect to have deformations near the  $180^\circ$  position. With this in mind, a logical choice would be to reduce the blade loading once it reaches its top position. A way to obtain this loading reduction would be to decrease the angle of attack locally. The angle of attack on a blade can be defined using equation (5.4). For small angles, one can assume that the angle of attack is linearly proportional to the lift coefficient, such that lift can be described as:

$$C_L = a + b \cdot \alpha = a(r) + b(r) \cdot \left( \phi^0(r) - \tan^{-1} \left( \frac{J(r, \theta) \cdot D}{2\pi r} \right) + \Delta\phi(r, \theta) \right) \quad (5.9)$$

Here an adopted version of equation (5.4) is applied, where  $\Delta\phi$  denotes the local twist deformation. For the case of a rigid propeller the original lift coefficient  $C_L^0$ , can be defined:

$$C_L^0 = a(r) + b(r) \cdot \left( \phi^0(r) - \tan^{-1} \left( \frac{J(r, \theta) \cdot D}{2\pi r} \right) \right) \quad (5.10)$$

The rigid lift coefficients can be calculated with PROCAL for open water conditions as well as wakefield conditions, the results can be utilized to find a value for b. First the following relations are defined:

$$\begin{aligned} C_{L,ow}^0 &= a + b \cdot \alpha_{ow}^0 \\ C_{L,wake}^0 &= a + b \cdot \alpha_{wake}^0 = a + b \cdot (\alpha_{ow}^0 + \Delta\alpha) \end{aligned} \quad (5.11)$$

where  $\alpha_{ow}^0$  can be determined with equation (5.4), and  $\alpha_{wake}^0$  with an adopted version of (5.4) to account for the tangential velocity component in a wakefield:

$$\alpha^0 = \phi^0(r) - \tan^{-1} \left( \frac{u_x(r, \theta)}{2\pi nr - u_\theta(r, \theta)} \right) \quad (5.12)$$

These equations are then combined to find b:

$$b = \frac{C_{L,wake}^0 - C_{L,ow}^0}{\Delta\alpha} = \frac{C_{L,wake}^0(r, \theta) - C_{L,ow}^0(r, \theta)}{\tan^{-1} \left( \frac{J_{ow}(r) \cdot D}{2\pi r} \right) - \tan^{-1} \left( \frac{u_{x,wake}(r, \theta)}{2\pi nr - u_{\theta,wake}(r, \theta)} \right)} \quad (5.13)$$

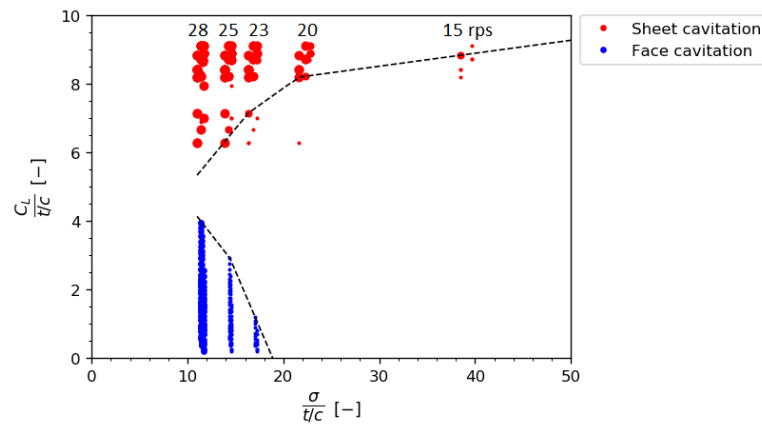


Figure 5.5: Bucket diagram of C4-40 operating in non uniform flow field ( $J = 0.65$ )

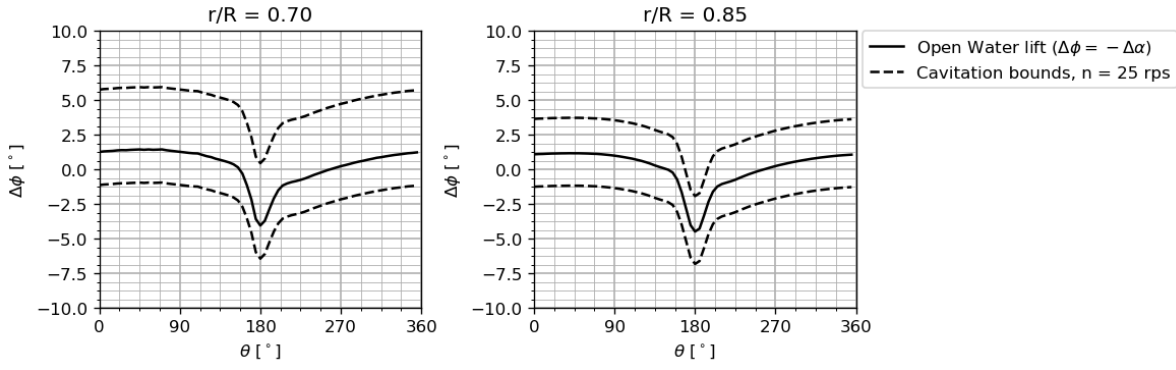


Figure 5.6: Twist deformation boundaries in non uniform flow field ( $J = 0.65$ ,  $n = 25$  rps)

When this is discretized and solved, values for  $b$  are computed at each radial and angular point. Because of the linearity assumption, the matrix is converted to a vector by taking each  $b$  at the best fitting angular position. The resulting vector  $b$  can be utilized to define the lift coefficient as followed:

$$C_L = C_{L,ow}^0(r) + b(r) \cdot (\Delta\phi(r, \theta) + \Delta\alpha(r, \theta)) \quad (5.14)$$

With a relation between the inflow angle and lift coefficient, the limits of the pitch angle can be defined by using the bucket diagram in figure 5.5. In figure 5.6 the boundaries for cavitation occurrence are shown, as well as the deformation required to reach open water lift conditions. It clearly shows that the required twist deformation increases towards the blade tip. As mitigating sheet cavitation is the main objective, the focus is lied upon finding the optimal angular displacement in the tip region. Note that the surface beneath the curve should equal zero, such that the thrust generated in a full revolution remains unaltered in comparison with a rigid propeller. That largely reduces the design freedom in this scenario, a reasonable choice is to aim for obtaining a twist to achieve open water lift conditions. This may improve the efficiency as well since it brings the local flow closer to the design conditions. As the deformation of the blade is a combination of twist and bend, the influence of the latter should be considered as well. The angle of attack is likely to be influenced by bending velocities of the blade as well. For a flexible propeller, the new equation for the angle of attack becomes:

$$\alpha = \phi^0(r) - \tan^{-1} \left( \frac{u_x(r, \theta) - U_x(r, \theta)}{2\pi nr - u_\theta(r, \theta) - U_\theta(r, \theta)} \right) + \Delta\phi \quad (5.15)$$

Where  $U_x$  and  $U_\theta$  denote the axial and tangential blade velocity respectively. The influence of the blade vibrations is accounted for in the PROCAL DLL applied in the unsteady FSI. The main goal here is to passively adapt the pitch at a limited bend deformation to mitigate the vibration influence of the blades. That said, the bend velocity and pressure induced camber may be utilized as well to locally unload the blade, but that lies outside the scope of this study.

Considering the above, twist deformations (at  $r/R = 0.85$ ) in the order of  $\Delta\phi \approx 5^\circ$  are required to yield optimal efficiency, and  $\Delta\phi \approx 2^\circ$  to prevent cavitation in this particular loading condition. At higher shaft velocity this increases rapidly. As it may not be very realistic to have deformations of such magnitude, an important question is whether cavitation has to be incepted or not. Research has shown that vibrations induced by cavitation are proportional to the second time derivative of the cavity volume [14]. That is, the pressure fluctuations are dependent on the rate of change of the slope of the cavity volume curve. As discussed earlier, a cavity in a uniform flow inflicts significantly smaller pressure pulses because of the relatively stable cavity volume. The gradient of the cavity volume is strongly related to the gradient of the effective inflow angle. When the twist deformation is insufficient to deplete cavitation but counteracts the difference in  $\alpha$  throughout the revolution, it will flatten the gradient in the inflow angle and therefore still mitigate the pressure pulses. Further, the operational profile of the vessel is of importance as well, since this is a passive system. The deformations are linearly proportional to the thrust, and quadratically proportional to the ship speed. Defining the right deformation then, is clearly a trade off. The objective in the following section is to find the material required to achieve sub optimal thrust conditions at the radial positions shown in figure 5.6, without negatively influencing the efficiency at lower loading conditions.

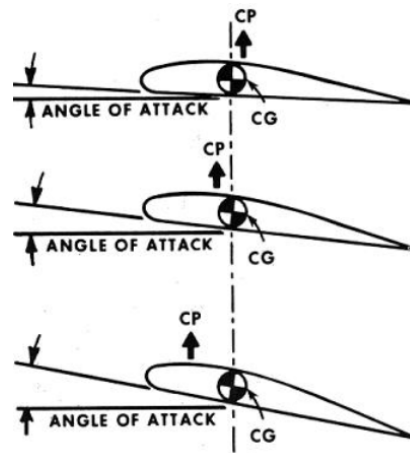


Figure 5.7: Change in center of pressure with AoA (obtained from: [19])

### 5.3. Material setup

The objective is to design a propeller blade, which passively adapts the pitch, dependent on the loading condition. That is, the pitch should decrease in the vicinity of the ship boundary layer when a blade is in the upward position. When an isotropic material is used for the C4-40 propeller the opposite occurs. To understand why this is the case, the forces acting upon a propeller cross section were examined. When a blade approaches the ship boundary layer and the loading increases, the center of pressure moves forward (in chordwise direction). An illustration of this is displayed in figure 5.7. As a result, the twist angle increases, ultimately leading to an increase in blade loading, the opposite of what is required. Two possible methods to overcome this problem are either applying skew to the blades or using anisotropic materials. Although skew can positively influence the twist behavior, it does present limitations, e.g. emergency braking may damage the blades when too much skew is applied on a fixed pitch propeller. Moreover, geometric design lies outside the research scope, hence the focus was placed upon finding a suitable anisotropic material.

#### 5.3.1. Composite properties

There are several possibilities to manufacture composites, generally, they are manufactured by combining a resin with a reinforcement material. For marine applications, the most commonly used reinforcement materials are glass- and carbon fibers. Where carbon fibers are applied for advanced marine vehicles with extremely high strength and stiffness requirements, glass fibers have a more cost effective application and good processability [31]. Typical resins for marine applications are polyesters, epoxies, and vinyl esters. Polyesters are the cheapest, for normal applications. Then vinyl offers a significantly better corrosion and impact resistance, be it at a higher cost. In more advanced designs often epoxies are applied, providing better corrosion resistance than vinyl esters and excellent fatigue resistance. That said, due to handling concerns epoxies are usually limited to small scale marine applications [31]. Though expensive, glass or carbon reinforced composites combined with vinyl esters or epoxy resins show impressive behavior in terms of impact, corrosion, and fatigue resistance.

**Isotropic versus anisotropic** When a material experiences elastic deformations, a distinction is made between isotropic and anisotropic materials. When a longitudinal load is applied on an isotropic plate, it only experiences extension and a small compression in transverse direction. An anisotropic plate on the other hand would experience an angular distortion and a transverse contraction. In case of small deformations, the stress-strain relation for a two-dimensional isotropic plate can be written as:

$$\begin{Bmatrix} \varepsilon_x \\ \varepsilon_y \\ \gamma_{xy} \end{Bmatrix} = \begin{bmatrix} \frac{1}{E} & -\frac{\nu}{E} & 0 \\ -\frac{\nu}{E} & \frac{1}{E} & 0 \\ 0 & 0 & \frac{1}{G} \end{bmatrix} \begin{Bmatrix} \sigma_x \\ \sigma_y \\ \tau_{xy} \end{Bmatrix} \quad (5.16)$$

With  $\nu$  denoting the Poisson ratio,  $E$  the elasticity modulus and  $G$  the shear modulus defined as:

$$G = \frac{E}{2(1 + \nu)} \quad (5.17)$$

This means that the elasticity of the anisotropic material can be characterised by two constants,  $\nu$  and  $E$ . For the anisotropic plate, the following holds:

$$\begin{Bmatrix} \varepsilon_x \\ \varepsilon_y \\ \gamma_{xy} \end{Bmatrix} = \begin{bmatrix} \frac{1}{E_x} & -\frac{\nu_{yx}}{E_y} & 0 \\ -\frac{\nu_{xy}}{E_x} & \frac{1}{E_y} & 0 \\ 0 & 0 & \frac{1}{G_{xy}} \end{bmatrix} \begin{Bmatrix} \sigma_x \\ \sigma_y \\ \tau_{xy} \end{Bmatrix} \quad (5.18)$$

Where  $\nu_{xy}$  can be written as function of  $\nu_{yx}$ :

$$\nu_{xy} = \nu_{yx} \frac{E_x}{E_y} \quad (5.19)$$

In this case the number of independent variables raises to four:  $E_x, E_y, G_{xy}$  and  $\nu_{yx}$ .

**Laminates** A composite material is composed of several plies, which together form a structural system. A ply consists of the reinforcement material (fiber) and resin. Typical parameters determining the properties of the ply are the fiber mass fraction,  $M_f$ :

$$M_f = \frac{\text{Fiber mass}}{\text{Total mass}} \quad (5.20)$$

and the ply thickness, defined as:

$$t_p = \frac{m_f}{V_f \rho_f} \quad (5.21)$$

with  $V_f$  denoting the fiber volume fraction,  $\rho_f$  the fiber density and  $m_f$  the fiber mass in grams per square meter of material. Typical ply thicknesses are 0.125 mm - 0.175 mm [2]. With the volume fractions and the properties of the fiber and resin, the properties of the ply can be determined. The elasticity moduli are:

$$\begin{aligned} E_\ell &= E_{f,\ell} \cdot V_f + E_r \cdot V_r \\ E_t &= E_r \left[ \frac{1}{(1 - V_f) + \frac{E_r}{E_{f,t}} V_f} \right] \end{aligned} \quad (5.22)$$

where the subscript f and r denote the fiber and resin respectively. The longitudinal direction is denoted by  $\ell$ , and the transverse direction by  $t$ . Here the resin is isotropic and the fiber is anisotropic. The shear modulus is defined as followed:

$$G_{\ell t} = G_r \left[ \frac{1}{(1 - V_f) + \frac{G_r}{G_{f,\ell t}} V_f} \right] \quad (5.23)$$

The Poisson coefficient is:

$$\nu_{\ell t} = \nu_{f,\ell t} \cdot V_f + \nu_{r,\ell t} \cdot V_r \quad (5.24)$$

The laminate is a superposition of many ply layers. One of the fundamental advantages of laminates is their ability to control the fiber orientation, such that the mechanical behavior can be optimized in a specific direction. It is important to predict in what matter the relative orientations of the plies influence the laminate resistance. To ensure a proper resistance against bi-axial tension and shear stress, the fibers should be oriented perpendicular to each other. This way, when shear is applied, causing tension and compression in the perpendicular direction, the fibers can always support the tension, while the resin supports the compression. For processability reasons, the thickness of a laminate is at least one millimeter, consisting of a number of plies with different orientations. Using many consecutive plies with the same orientation should be avoided in order to limit interlaminar stresses [2]. When constructed, the laminates are heated to high temperatures for a curing process. After that, they are cooled again, but then thermal residual stresses arise, which are dependent upon the ply orientation. Therefore the ply orientation always has a symmetry plane in the middle of the laminate to prevent deformations [2].

The properties of the anisotropic laminate structure, i.e. the variables in equation (5.18), are dependent on the variation in plies applied in the structure. They can be determined with the use of Classic Laminate

Theory (CLT). CLT has been developed for a laminate under in-plane loads. For this theory to be valid, the plies are assumed as orthotropic and homogeneous [27]. Note that this theory may not yield valid inter-laminar stresses, since it is usually applied for very thin plates ( $L/t > 30$ ). In this case though, the theory is applied to determine strains rather than stresses. A relation is described between the strains and curvatures of a laminate, and the forces and moments of a laminate:

$$\begin{bmatrix} N_x \\ N_y \\ N_{xy} \\ M_x \\ M_y \\ M_{xy} \end{bmatrix} = \begin{bmatrix} A_{11} & A_{12} & A_{16} & B_{11} & B_{12} & B_{16} \\ A_{12} & A_{22} & A_{26} & B_{12} & B_{22} & B_{26} \\ A_{12} & A_{26} & A_{66} & B_{16} & B_{26} & B_{66} \\ B_{11} & B_{12} & B_{16} & D_{11} & D_{12} & D_{16} \\ B_{12} & B_{22} & B_{26} & D_{12} & D_{22} & D_{26} \\ B_{16} & B_{26} & B_{66} & D_{16} & D_{26} & D_{66} \end{bmatrix} \begin{bmatrix} \varepsilon_x^0 \\ \varepsilon_y^0 \\ \gamma_{xy}^0 \\ \kappa_x \\ \kappa_y \\ \kappa_{xy} \end{bmatrix} \quad (5.25)$$

where N and M denote the forces and moments respectively.  $\varepsilon$  and  $\gamma$  denote the strains, and  $\kappa$  the curvatures. x represents the longitudinal direction and y the transverse direction of the beam. A, B and D are respectively the extensional, coupling and bending stiffness matrices, defined as:

$$\begin{aligned} A_{ij} &= \sum_{k=1}^{N_p} [\bar{Q}_{ij}]_k (h_k - h_{k-1}) \\ B_{ij} &= \frac{1}{2} \sum_{k=1}^{N_p} [\bar{Q}_{ij}]_k (h_k^2 - h_{k-1}^2) \\ D_{ij} &= \frac{1}{3} \sum_{k=1}^{N_p} [\bar{Q}_{ij}]_k (h_k^3 - h_{k-1}^3) \end{aligned} \quad (5.26)$$

with  $h_k - h_{k-1}$  denoting the thickness of ply k, i.e. the difference between upper and lower side.  $Q_{ij}$  are the elements of the transformed reduced stiffness matrix for one ply:

$$\begin{aligned} \bar{Q}_{11} &= Q_{11}c^4 + Q_{22}s^4 + 2(Q_{12} + 2Q_{66})s^2c^2 \\ \bar{Q}_{12} &= (Q_{11} + Q_{22} - 4Q_{66})s^2c^2 + Q_{12}(c^4 + s^2) \\ \bar{Q}_{22} &= Q_{11}s^4 + Q_{22}c^4 + 2(Q_{12} + 2Q_{66})s^2c^2 \\ \bar{Q}_{16} &= (Q_{11} - Q_{12} - 2Q_{66})c^3s - (Q_{22} - Q_{12} - 2Q_{66})s^3c \\ \bar{Q}_{26} &= (Q_{11} - Q_{12} - 2Q_{66})s^3c - (Q_{22} - Q_{12} - 2Q_{66})c^3s \\ \bar{Q}_{66} &= (Q_{11} - Q_{22} - 2Q_{12} - 2Q_{66})s^2c^2 + Q_{66}(s^4 + c^4) \end{aligned} \quad (5.27)$$

c and s denote  $\cos\theta_p$  and  $\sin\theta_p$  respectively,  $\theta_p$  is the orientation of the ply.  $Q_{11}$ ,  $Q_{12}$ ,  $Q_{22}$  and  $Q_{66}$  are calculated as follows:

$$\begin{aligned} Q_{11} &= \frac{E_\ell}{1 - \nu_{\ell t}\nu_{t\ell}} \\ Q_{12} &= \frac{\nu_{\ell t}E_t}{1 - \nu_{\ell t}\nu_{t\ell}} \\ Q_{22} &= \frac{E_t}{1 - \nu_{\ell t}\nu_{t\ell}} \\ Q_{66} &= G_{\ell t} \end{aligned} \quad (5.28)$$

For a symmetric laminate, the coupling matrix (B) is zero, due to the quadratic term in the expression. In that case equation (5.25) reduces to the following sets of equations:

$$\begin{bmatrix} N_x \\ N_y \\ N_{xy} \end{bmatrix} = \begin{bmatrix} A_{11} & A_{12} & A_{16} \\ A_{12} & A_{22} & A_{26} \\ A_{12} & A_{26} & A_{66} \end{bmatrix} \begin{bmatrix} \varepsilon_x^0 \\ \varepsilon_y^0 \\ \gamma_{xy}^0 \end{bmatrix} \quad (5.29)$$

$$\begin{bmatrix} M_x \\ M_y \\ M_{xy} \end{bmatrix} = \begin{bmatrix} D_{11} & D_{12} & D_{16} \\ D_{12} & D_{22} & D_{26} \\ D_{16} & D_{26} & D_{66} \end{bmatrix} \begin{bmatrix} \kappa_x \\ \kappa_y \\ \kappa_{xy} \end{bmatrix} \quad (5.30)$$

The E-modulus in x direction can be determined with Hooke's law, and then substituting equation (5.29):

$$E_x = \frac{N_x/h}{\varepsilon_x} = \frac{1}{h} \left[ A_{11} + A_{12} \left( \frac{A_{26}A_{16} - A_{12}A_{66}}{A_{22}A_{66} - A_{26}^2} \right) + A_{16} \left( \frac{-A_{16}}{A_{66}} + \frac{A_{26}A_{12}A_{66} - A_{26}^2A_{16}}{A_{22}A_{66}^2 - A_{26}^2A_{66}} \right) \right] \quad (5.31)$$

A similar procedure is then followed for the E-modulus in y direction:

$$E_y = \frac{N_y/h}{\varepsilon_y} = \frac{1}{h} \left[ A_{12} \left( \frac{A_{16}A_{26} - A_{12}A_{66}}{A_{11}A_{66} - A_{16}^2} \right) + A_{22} + A_{26} \left( \frac{-A_{26}}{A_{66}} + \frac{A_{16}A_{12}A_{66} - A_{16}^2A_{26}}{A_{11}A_{66}^2 - A_{16}^2A_{66}} \right) \right] \quad (5.32)$$

The shear modulus is calculated as follows:

$$G_{xy} = \frac{N_{xy}/h}{\gamma_{xy}} = \frac{1}{h} \left[ A_{66} - \frac{A_{26}^2}{A_{22}} + \frac{2A_{12}A_{16}A_{26}A_{22} - A_{12}^2A_{26}^2 - A_{16}^2A_{22}^2}{A_{11}A_{22}^2 - A_{12}^2A_{22}} \right] \quad (5.33)$$

The Poisson ratios are the ratio between longitudinal and transverse strain:

$$\begin{aligned} \nu_{xy} &= \frac{-\varepsilon_y}{\varepsilon_x} = \frac{\left( A_{12} - \frac{A_{16}A_{26}}{A_{66}} \right)}{\left( A_{22} - \frac{A_{26}^2}{A_{66}} \right)} \\ \nu_{yx} &= \frac{-\varepsilon_x}{\varepsilon_y} = \frac{\left( \frac{A_{16}A_{26}}{A_{66}} - A_{12} \right)}{\left( \frac{A_{16}^2}{A_{66}} - A_{11} \right)} \end{aligned} \quad (5.34)$$

In order to verify this approach, the independent variables ( $E_x, E_y, G_{xy}, \nu_{xy}$ ) have been computed for a glass fiber reinforced epoxy, with a volume fraction  $V_f = 0.6$ . This was done for a number of different ply orientations displayed in table 5.1, together with the results of the CLT calculations.

#	0° [%]	45° [%]	90° [%]	$E_x$ [GPa]	$E_y$ [GPa]	$G_{xy}$ [GPa]	$\nu_{xy}$ [-]
1	50	0	50	28.5	28.5	3.72	0.113
2	20	60	20	18.7	18.7	7.29	0.269
3	40	20	40	25.7	25.7	5.33	0.169
4	50	30	20	29.3	18.7	5.95	0.247

Table 5.1: Results for CLT computations (Glass/Epoxy Laminate,  $V_f = 0.6$ )

These computations can be validated with experimental data. In [2], experimental data from measurements on composite plates is present. These graphs are given in appendix A, from this the independent variables can be obtained. Table 5.2 displays the data obtained from the graphs, and the relative difference with the CLT results. From these results, it can be concluded that the theory can suffice as a preliminary design tool, but is insufficient for accurate predictions of the independent variables. The results show that in general, the Young's moduli are predicted more accurately than the shear modulus and Poisson ratio. Also, the predictions improve when only 0° and 90° plies are present, as it simplifies the structure.

#	$E_x$ [GPa]	$E_y$ [GPa]	$G_{xy}$ [GPa]	$\nu_{xy}$ [-]	$\Delta E_x$ [%]	$\Delta E_y$ [%]	$\Delta G_{xy}$ [%]	$\Delta \nu_{xy}$ [%]
1	28.7	28.7	4.50	0.13	0.70	0.70	21	15
2	21.2	21.2	9.45	0.36	13	13	29	33
3	26.5	26.5	6.15	0.19	3.1	3.1	15	12
4	30.0	20.5	6.98	0.28	2.4	9.6	17	13

Table 5.2: Experimental date compared with CLT computations (Glass/Epoxy Laminate,  $V_f = 0.6$ )

### 5.3.2. Defining material properties

In order to define the required composite properties, an analytic method is presented, where the propeller blade has been simplified to a laminate fixed at one end. This laminate has length L, width b and thickness t, consisting of a number of plies,  $N_p$ . An illustration is given in figure 5.8.

In this simplified case, only a moment in one direction is applied,  $M_x$ . Rearranging equation (5.30) yields the following set of equations:

$$\begin{bmatrix} \kappa_x \\ \kappa_y \\ \kappa_{xy} \end{bmatrix} = \begin{bmatrix} D_{11} & D_{12} & D_{16} \\ D_{12} & D_{22} & D_{26} \\ D_{16} & D_{26} & D_{66} \end{bmatrix}^{-1} \begin{bmatrix} M_x \\ 0 \\ 0 \end{bmatrix} \quad (5.35)$$

Now the bending curvature  $\kappa_x$  and twisting curvature  $\kappa_{xy}$  are dependent on the four properties describing the ply, the bending moment, and the thickness, orientation, and number of plies. The properties of the ply are dependent on the resin and fiber material and their volume fractions, (equations (5.22), (5.23) and (5.24)). An iterative python script was constructed to optimize the twist over bend ratio of the composite. The design variables in this procedure are the fiber materials, their volume fraction, and the ply orientations. The following constraints have been implemented in the procedure:

1. The maximum number of consecutive layer is limited to 4, in order to limit inter-laminate stresses [2]
2. The number of plies is set constant,  $N_p = 12$
3. The ply thicknesses are assumed constant,  $t_p = 0.15mm$
4. The ply orientation is between  $-75^\circ$  to  $90^\circ$ , with a step size of  $15^\circ$ . This is for the workability of the material and limiting the computational time
5. At least two plies (on both symmetry sides) should be oriented perpendicular to each other, in order to yield sufficient resistance against bi-axial loading.
6. The resin material is epoxy, with the properties displayed in table 5.3
7. The fiber volume fractions are:  $V_f = [0.3, 0.4, 0.5, 0.6, 0.7]$
8. A selection of fibers is used, these are displayed in table 5.3

Property	Epoxy	Glass	Kevlar	Carbon H.T.	Carbon H.M.
$E_\ell$	4.5	74	130	230	390
$E_t$	4.5	74	5.4	15	6.0
$G_{\ell t}$	1.6	30	12	50	20
$\nu_{\ell t}$	0.40	0.25	0.40	0.30	0.35

Table 5.3: Properties of resin and fiber selection (obtained from [2])

The results of the computations are shown in table 5.4. Interestingly, the ply orientations, as well as the fiber volume fractions, are comparable for all fiber reinforcement materials. Note that the longitudinal and transverse Elasticity moduli, and the twist over bend ratio are estimated for the beam. Hence, they may not be an accurate representation of the actual blade properties.

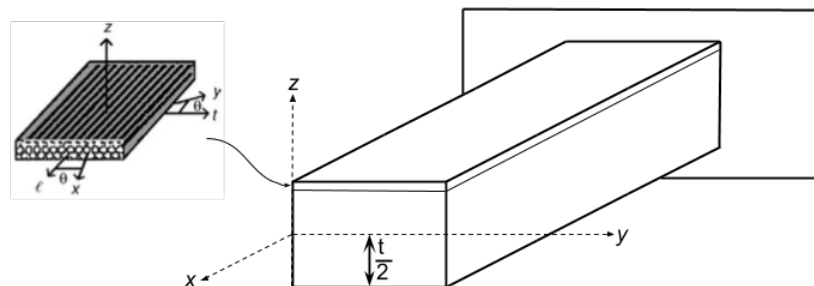


Figure 5.8: Laminate fixed at one end

Fiber	$V_f$ [-]	Ply orientations [°]	$E_x$ [MPa]	$E_y$ [MPa]	$\kappa_{xy}/\kappa_x$ [-]
Glass	0.6	[15. 15. 15. 15. 90. 0. 0. 90. 15. 15. 15. 15.]	32.3	16.2	-1.348
Kevlar	0.6	[15. 15. 15. 15. 90. 0. 0. 90. 15. 15. 15. 15.]	46.0	17.7	-2.112
Carbon H.R.	0.5	[15. 15. 15. 15. 90. 0. 0. 90. 15. 15. 15. 15.]	72.6	29.9	-2.477
Carbon H.M.	0.6	[15. 15. 15. 75. 0. 90. 90. 0. 75. 15. 15. 15.]	90.4	66.7	-2.966

Table 5.4: Epoxy composite setup for optimal twist/bend

PVAST requires the equivalent moduli and Poisson coefficients in the 1st, 2nd and 3rd principle direction for each ply as input. These are determined as followed:

$$\begin{aligned}
 E_1 &= E_\ell \\
 E_2 &= E_3 = E_t \\
 G_{13} &= G_{31} = G_{\ell t} \\
 G_{23} &= \frac{E_t}{2(1 + \nu_r)} \\
 \nu_{13} &= \nu_{\ell t} \\
 \nu_{23} &= \nu_r \\
 \nu_{31} &= \nu_{t\ell}
 \end{aligned} \tag{5.36}$$

## 5.4. Results

The results of the ComPropApp computations for the four different composites, displayed in table 5.3 are displayed in figure 5.9. The bend deformation is remarkably similar for Glass, Kevlar, and H.T. (High Tensile strength) carbon fibers, the differences in twist slightly more significant. The H.M. (High Modulus) carbon reinforced epoxy is clearly stiffer than the others, therefore it has significantly smaller bend and twist deformations. In general, all reinforced epoxies show a clear increase in twist deformation in the highly loaded area in the revolution. An increase in twist leads to a decrease in pitch, thus decrease in angle of attack and consequentially the load. This suggests that it is possible to passively adapt the twist such that it positively influences the load distribution throughout the revolution. That said, the twist differences are insufficient to fulfill the requirements set in section 5.2.6, which leads to conclude that this is a case of mitigating cavitation, rather than suppressing. To obtain larger twist deformations the fiber volume fractions may be lowered, although this has the side effect of increasing the bend deflection as well. The alternative is to re-design the propeller geometry, for instance by increasing skew.

All cases show an average twist deflection that will decrease the total thrust generated by the propeller. In order to overcome this, the undeformed propeller geometry has been revised by slightly increasing the P/D value. This was done for the glass reinforced composite, by means of adding the difference between average deformed and undeformed P/D to the undeformed propeller geometry. The total generated thrust is compared for a rigid blade and the Glass/Epoxy blade with an altered P/D ratio. This comparison is displayed in figure 5.10. The average hydrodynamic properties are compared as well and shown in table 5.5. The deformed blade generates slightly more thrust on average (2.2%), whereas it clearly has a lower peak value than the rigid blade. Interestingly, the efficiency is slightly increased as well for the composite propeller. To deter-

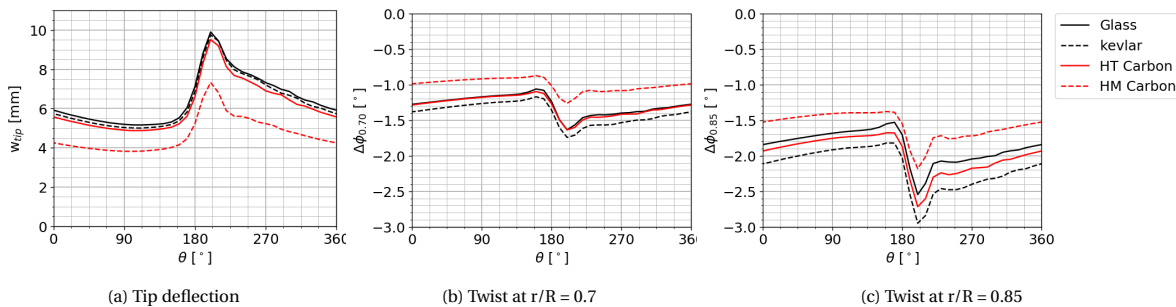


Figure 5.9: Deformations in wakefield (n = 25 rps, J = 0.65)

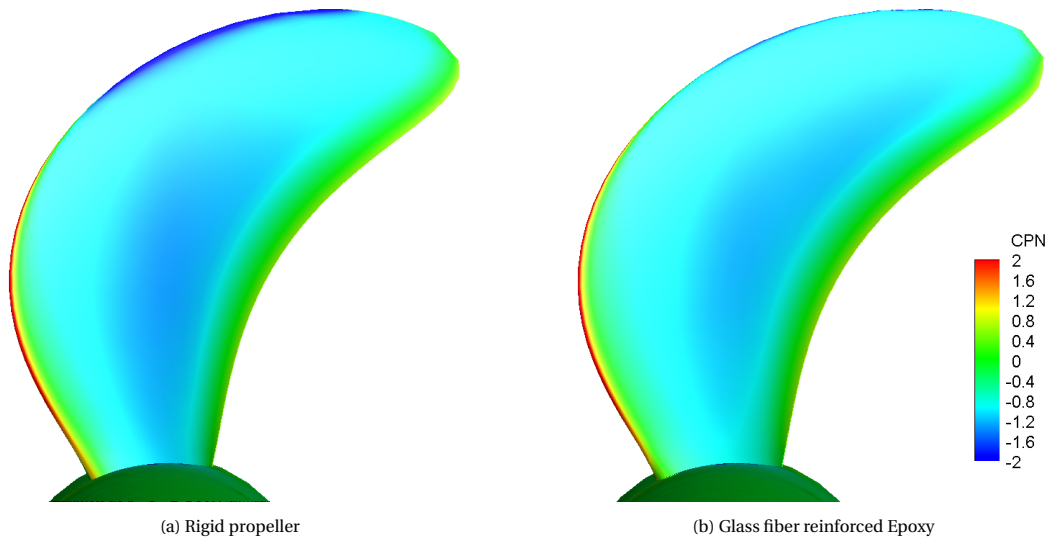


Figure 5.11: Dynamic pressure distributions at  $\theta = 180^\circ$  (Suction side,  $J = 0.65$ ,  $n = 25$  rps)

mine the exact effect of the local blade unloading on the dynamic pressure field, the pressure distributions at the  $180^\circ$  blade position were evaluated for the rigid and Glass/Epoxy materials. The suction side pressure distributions are shown in figure 5.11. cavitation originates in the low pressure region near the leading edge of the blade, which is clearly visible for the rigid blade. These figures confirm that cavitation is indeed less likely to occur, as the low pressure peak of the composite is much less significant.

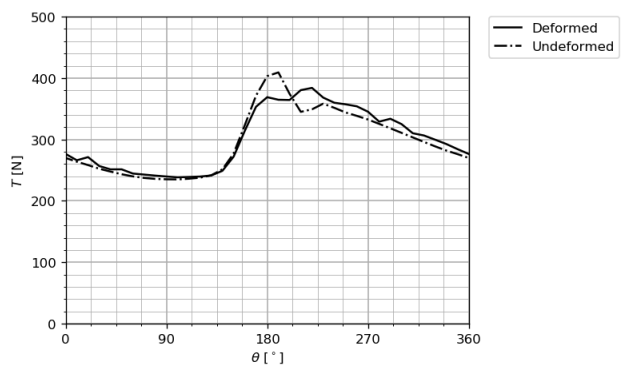


Figure 5.10: Thrust Comparison between rigid and Glass/Epoxy propeller

Parameter	Rigid	Glass/Epoxy
T [N]	1074	1098
Q [Nm]	54.34	54.66
$k_T$ [-]	0.1289	0.1317
$k_Q$ [-]	0.01917	0.01929
$\eta$ [%]	70.70	71.85

Table 5.5: Comparison hydrodynamic parameters

## 5.5. Conclusions

An approach to design a self twisting composite propeller was presented in this chapter, with the purpose to mitigate cavitation. It was found that cavitation is strongly related to the effective inflow angle with respect to the propeller blade. Suppressing cavitation can be achieved by passively adapting the pitch, such that the local angles of attack do not exceed a critical point. However, it can also be mitigated by minimizing the angles of attack up to a realistic extent and reducing the (second) time gradient of the pressure field, which the aggressiveness of cavitation is related to. An important assumption in this study is that only the twist of the blade influences the hydrodynamic pressures. In fact, the vibration velocities significantly influence the PROCAL results. In a future study, it is therefore recommended to consider the vibration effects in the design process. Additionally, pressure induced camber deformations are of influence as well, it was found that in general this is of minor importance for composites. By means of an iterative script applying Classical Laminate Theory, where the propeller blade is modeled as a simplified clamped beam, a material setup was computed for a number of fiber reinforced epoxies. Computations performed with these materials in wake-field conditions showed that the propeller blade utilizes bend-twist coupling effects to unload the propeller blade in the ship boundary layer region of a wakefield. To ensure that a similar thrust would be generated in comparison with a rigid propeller, the  $P/D$  ratio was increased for the undeformed geometry. The simplified plate model ensures a fast optimization process, therefore this may be a suitable tool for the preliminary design of composite propellers. Note that while this approach does provide a better performing propeller in the design condition, it may not be beneficial in off design conditions. For instance, at lower velocities, i.e. less thrust, deformations will be smaller and therefore the  $P/D$  would be larger with respect to the rigid propeller. This translates directly into the torque required to drive the propeller. The relative torque (torque per rpm) required for the composite propeller will be higher below the design speed, whereas above the design condition the opposite is true. Such behavior may complicate engine fitting in future designs. On top of that, the propeller efficiency will quickly decrease above the design speed, as a result of the continuously decreasing  $P/D$  ratio. This emphasizes that there is no optimal solution, but rather a trade off to be made between flexibility in the operational profile, and alleviating cavitation.



# 6

## Recommendations

This thesis has presented a verification and validation on the Fluid Structure Interaction software package ComPropApp, after which a study has been performed on the applicability of the software. The first section of this chapter describes the findings in this research, and recommendations for future purposes. The subsequent section treats a number of guidelines to follow in order to use the ComPropApp.

During the verification study, a number of corrections have been performed to the software to ensure the software to provide reliable results. However, a few unresolved problems remain, which may require future research to be resolved. Firstly, an adaptation to the structural solver applied in the steady FSI is currently being investigated, and should be implemented in the ComPropApp to resolve the problems arising when small loads are applied. Then, the PROPART toolbox is currently generating panel files with a uniform radial grid distribution, at the cost of capturing the effects in the tip region accurately. It is advised to adapt this, such that a panel grid based on PROWISE guidelines is generated instead. Further, the resemblance between the steady and unsteady FSI may improve if the pressure to force conversion would be performed more consistently for both solvers. Currently, the steady module applies an additional interpolation step in that conversion. A final adaptation advised to ComPropApp is the method for determining the time step size in the stress analysis. At the moment this is determined with the Nyquist frequency based on the natural frequency of the highest considered mode. With the purpose of saving significant computational time, a more suitable method would be to base the time step size on the highest excitation frequency.

The validation study has led to conclude that the unsteady FSI software is capable of qualitatively predicting the bend deformations in open water conditions. However, due to the large uncertainties arising from the Sikablock material properties and machining quality, the measurements cannot be utilized to define the accuracy of the FSI software. In wakefield conditions the additional uncertainty of the wake velocity distribution meant that these measurements are inconclusive for the validation. In these testing conditions, the deformations would fluctuate on a periodic base as a consequence of a very unstable flow field. Therefore, setting up a new wakefield by means of RANS simulations at the lower tunnel velocities may be required, though this was already discovered to be a difficult task in these velocities. An alternative may be to utilize thrust measurements performed with a rigid propeller, in order to apply a correction to obtain the effective average velocity field. A third possible approach may be to re-design the wakefield generator in the tunnel by means of RANS simulations, which is able to generate a more stable wake at low velocities. However, there would still remain the material and geometric uncertainties. The material uncertainty may be reduced by performing strength measurements on a number of material samples. Since three-dimensional scans were performed on the propeller geometry, the results may be used to generate a new geometry file. That said, it is currently not possible to implement geometries with different blade orientations in the ComPropApp.

The design element of this study aimed to find the benefits composite propellers may have to offer, and to determine whether the ComPropApp can be applied as a suitable design tool. The ComPropApp has shown large potential in the application of anisotropic materials, since it was possible to realize bend twist coupling motions, such that the propeller would unload itself when the local advance ratio decreases, unlike what was observed for isotropic materials. Since the validation of the unsteady FSI method is still inconclusive, the steady module was used to verify these results. These computations have shown a similar trend of unloading

at a decreased advance ratio. However, to improve the strength of the conclusions drawn, a future validation study with composite materials is recommended. An important limitation to the performed material study is that a composite was optimized for a simple clamped beam structure. A future study is recommended where the composite lay up is optimized for the blade geometry. In addition, it was assumed that only variable hydrodynamic properties related to twist deformations, whereas the vibration velocities and camber deformations may play an important role in this as well. Hence, it is advised to investigate the significance of these secondary effects further. This study has focused upon the application of a composite material for an existing propeller design. However, a further improvement in mitigating cavitation may be obtained by altering the geometry, for instance by increasing skew angles of the blades.

## 6.1. ComPropApp Guidelines

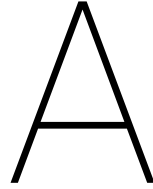
This section treats the recommended default settings to use as a starting point for the ComPropApp. The following steps have to be executed in preparation of an FSI computation.

1. Construct a \*.ppg file containing the propeller geometry. The layout of this file is elaborated in appendix D.1.
2. Construct a PROCAL control file (\*.ctr) and the panel file of the hub. This can be done within the Provis environment. The default settings of Provis suffice mostly, but a few adjustments are required in the control file (An example \*.ctr file is given in appendix D.3):
  - (a) The type of PROCAL analysis selected in the [Control] section must equal the type of FSI simulation selected:  
 STEADY FSI → Unsteady\_computation = false  
 UNSTEADY FSI → Unsteady\_computation = true
  - (b) Increase maximum number of revolutions to e.g. 100 in the [Control] section, since this is not reset between iterations in the ComPropApp → Revolutions = 100
  - (c) In the [Control] section the number of timesteps per revolution is given. This value must be at least 20 for open water calculations and at least 36 for wakefield conditions  
 → Timesteps\_revolution = 36
  - (d) Add a line to the [Geometry] section → splitHub = false
  - (e) To ensure that panel center pressures and panel normal vectors are output of PROCAL, add a line to the [Data] section  
 → DebugData\_output = true
3. Create the meshing instructions file (\*.cdr) for TRIDENT. The layout of this file is displayed in appendix D.2. A recommended value for the FEM grid resolution is  $30 \times 30$ , a higher value will significantly increase the computational time. Due to the interpolation steps between FE and panel grids, it is recommended to select similar distributions for both grids.
4. The advised settings within the ComPropApp environment are displayed in table 6.1.

Tab	Parameter	Value	Explanation
Steady FSI	Load Steps	1-5	Dependent on expected deformation size $w_{tip}/D = 0.01 - 0.1$
	Iteration Loops	Load Steps + 4	Minimum value required to reach convergence in thrust
Unsteady FSI	Relaxation	0.2 - 0.7	Decrease when fluctuations are large (wakefield)
	Tolerance	0.1 %	User specified accuracy for thrust convergence
Steady/Unsteady FSI	# Rad/Chord Panels	$30 \times 30$	Panel resolution for the Propart generated blade (see step 3)
Modal/Unsteady/Stress	# Modes	20	Captured > 99.99% of the deformation in previous simulations

Table 6.1: Recommended ComPropApp settings





# Composite properties

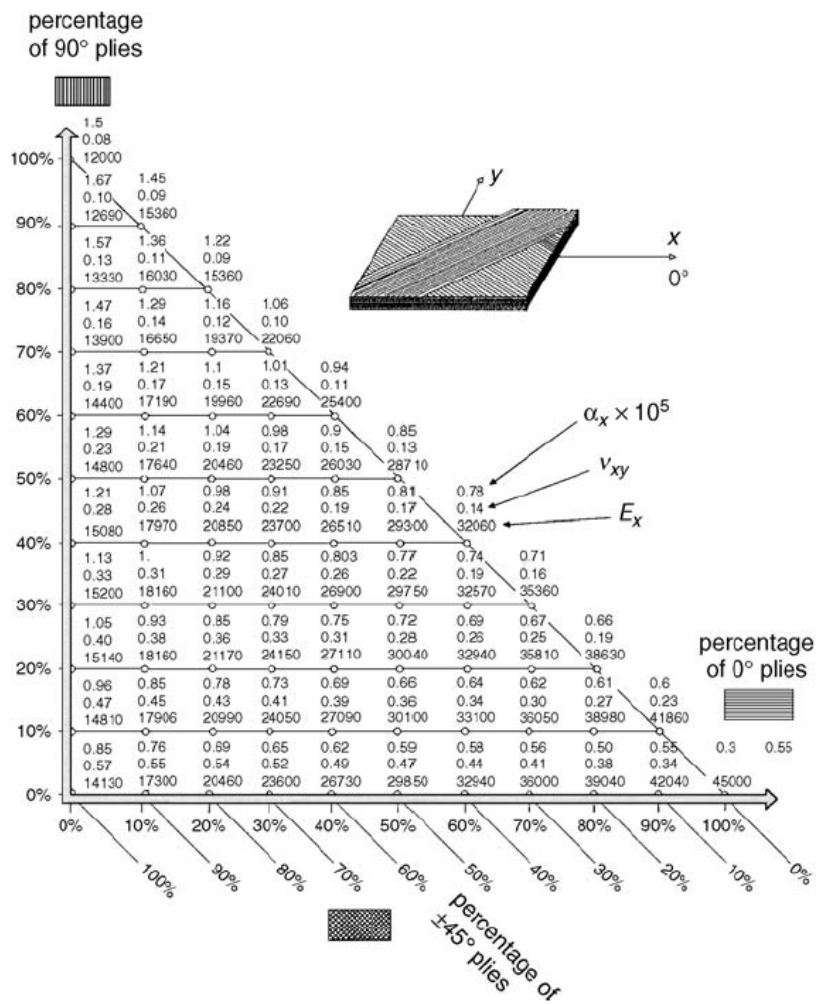


Figure A.1: Longitudinal modulus  $E_x$ , Poisson ratio  $\nu_{xy}$  and thermal expansion coefficient  $\alpha_x$  dependent on ply orientation for Glass/Epoxy laminates,  $V_f = 60\%$  (obtained from [2])

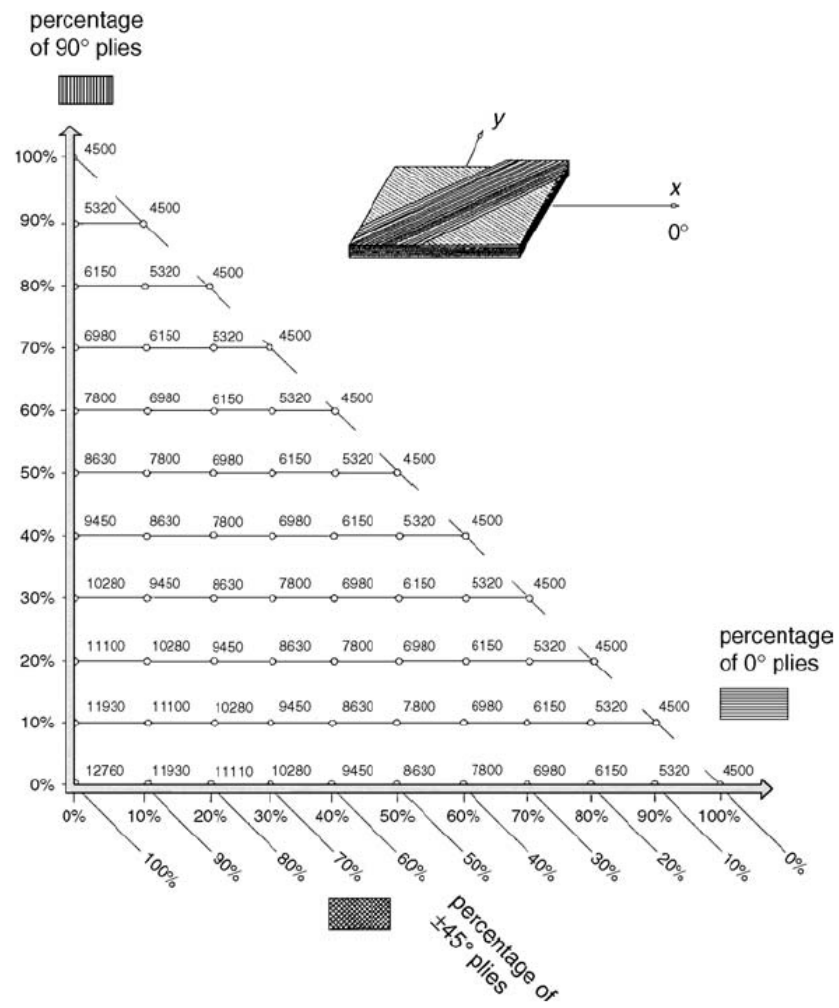


Figure A.2: Shear modulus  $G_{xy}$  dependent on ply orientation for Glass/Epoxy laminates,  $V_f = 60\%$  (obtained from [2])

# B

## Datasheet SikaBlock M700

Tooling & Composites

Product Data Sheet  
Version 02 / 2016

### SikaBlock® M700

#### Model board

**Areas of Application**

- Manufacture of data control models and cubings
- Manufacture of master models
- Manufacture of moulds for low pressure reaction injection moulding
- Vacuum forming moulds for lower number of pieces

**Product Benefits**

- Very high dimensional stability
- High compressive strength and edge stability
- Good solvent resistance
- High heat distortion temperature
- Easy machinability
- Low dust formation when milled
- Very dense, fine surface
- Easy to seal and good to varnish

**Description**

- Basis Polyurethane, light brown
- Adhesive **Biresin® Kleber braun Neu**, two component PUR system, brown
- Filler **Biresin® Spachtel braun Neu**, two component polyester system, brown

**Physical Data (approx.-values)**

SikaBlock® M700			
Density	ISO 845	g/cm <sup>3</sup>	0.7
Shore hardness	ISO 868	-	D 66
Flexural strength	ISO 178	MPa	26
E-Modulus	ISO 178	MPa	1,000
Compressive strength	ISO 604	MPa	25*
Impact resistance	ISO 179 Ue	kJ/m <sup>2</sup>	7
Heat distortion temperature	ISO 75 B	°C	90
Linear thermal expansion coefficient $\alpha_t$	DIN 53 752	K <sup>-1</sup>	55 x 10 <sup>-6</sup>

\* at 10% compressive strain

**Processing Data**

Adhesive / Filler		Biresin® Kleber braun Neu	Biresin® Spachtel braun Neu
Mixing ratio A : B	in parts by weight	100 : 65	100 : 2
Potlife	min	20	5
Setting time	h	8 - 10	> 20 min

**Packaging**

Board materials	<b>SikaBlock® M700</b>	1500 mm x 500 mm x 30 mm, 30 pieces / pallet 1500 mm x 500 mm x 50 mm, 36 pieces / pallet 1500 mm x 500 mm x 75 mm, 24 pieces / pallet 1500 mm x 500 mm x 100 mm, 18 pieces / pallet 1500 mm x 500 mm x 150 mm, 12 pieces / pallet
Adhesive	<b>Biresin® Kleber braun Neu</b> , resin (A) <b>Biresin® G53</b> , hardener (B)	1.5 kg net 4 kg; 0.975 kg net
Filler	<b>Biresin® Spachtel braun Neu</b> , resin (A) <b>BPO-Paste</b> , hardener (B)	2 x 8.34 kg net cartridges (A) 6 x 1.76 kg net tins (A) in a box 2 x 0.16 kg net sticks (B) (for cartridges - A) 6 x 0.04 kg net tubes (B) in a box (for tins - A)

SikaBlock® M700 1/2







Figure B.1: Datasheet SikaBlock M700 (obtained from [22])



# C

## Cavitation

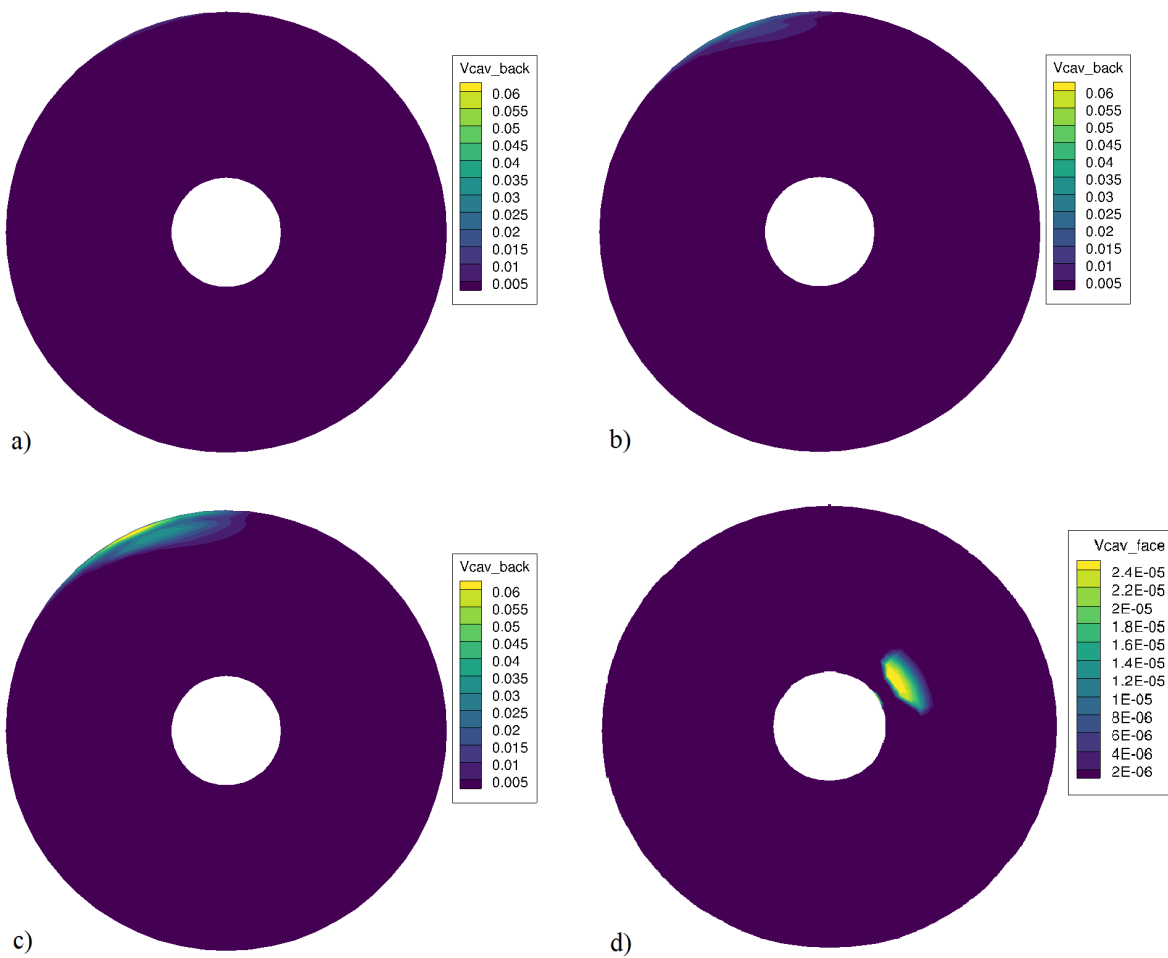


Figure C.1: Results unsteady cavitation simulation PROCAL at  $J = 0.6$ : a) Sheet cavitation at 15 rps, b) Sheet cavitation at 20 rps, c) sheet cavitation at 25 rps, d) face cavitation at 25 rps





# Constructing ComPropApp input files

## D.1. Propeller Geometry File (obtained from [3])

### D.1.1. Contents and Layout

The propeller geometry file input to Provise is divided into four parts as follows:

1. The first part describes general features of the propeller on separate lines including the propeller ID, propeller diameter in meters, hub diameter in meters, number of blades, two descriptive comment lines, the number of radial stations used for radial distributions of the key geometrical parameters for blade sections, the number of blade sectional profiles provided at the end of the file and a description of the sectional profile format. For the description of the sectional profile format, the value can be either BNF (Back & Face) to specify back and face coordinates normal to the chord line or CNT (Camber & Thickness) to specify camber offsets normal to the chord line and thickness normal to the camber line.
2. The second part of the file describes the radial distribution of key geometric parameters and starts with a comment line containing descriptive titles of the input parameters. These parameters are presented in separate columns for radius fraction, chord/diameter, skew in degrees, design rake/diameter, pitch/diameter, maximum thickness/chord and maximum camber/chord.
3. The third part of the file describes the blade sectional profiles at constant radii typically ordered from root to tip and with data for each radius formatted in four lines as follows:
  - non dimensional radius  $r/R$ , number of chord stations
  - a line of chord fractions or local  $x/c$ -coordinates
  - a line of local  $y_{back}/c$ -coordinates for format BNF (or local  $f/c$ -camber offsets for format CNT)
  - a line of local  $y_{face}/c$ -coordinates for format BNF (or local  $t/c$ -thickness values for format CNT)Local coordinates ( $y_{back}/c$ ,  $y_{face}/c$ ) or camber offsets ( $f/c$ ) for section profiles are defined to be positive on the back surface side of the chord line.
4. The fourth part of the file is optional. It contains offsets to describe the shape of the hub. It begins with a line to indicate how many offset points there are which is followed by the offsets themselves: two values per line giving  $(x,r)$  in PROCAL Polar Coordinates.

### D.1.2. Current Provise Restrictions on Input Data and Formatting

1. Only the first comment line for the propeller description is displayed in the Description field of the Propeller Dialog.
2. String data input from the file are case sensitive.
3. Provise currently requires the number and values of radial stations for the sectional profiles be the same as those used for the key geometrical parameters.
4. If the tip chord length has a value close to zero, it is recommended that it be set to zero since only a zero tip chord length can be modified in Provise to use a finite tip chord length.

5. The values for the maximum thickness and maximum camber are not required by Prowise to generate the blade surface geometry since this information is determined from the sectional profile offsets.
6. The propeller geometry definition is according to the ITTC standard and the input rake data are defined as design or applied rake and not the total rake (i.e. positive aft and excluding the skew-induced portion), and with the skew angle defined as positive when opposite to the direction of ahead rotation.
7. Numerical data can be specified in standard integer or floating point formats
8. Prowise currently does not allow empty or blank lines to be included between the rows of data items and comment lines must be located only at specified lines as indicated in the following sample file.
9. Prowise requires section profile coordinates (x/c, y/c) with chord stations x/c in the range 0 to 1 from leading edge to trailing edge. Prowise now allows finite leading edge offsets provided the leading edge is closed. Prowise also allows input of blunt trailing edges with different yback/c and yface/c values that will automatically be adjusted to a sharp edge before generating the blade surface paneling using one of three closure methods described in Generation of panels on propellers for CRS PROCAL and selected in the Blade Geometry tab on the Propeller Dialog.

### D.1.3. Example Propeller Geometry File

In the following example of a .ppg file, the text between brackets are comments that are not part of the file contents.

```

propeller id = P4119
propeller diameter = 0.3048
hub diameter = 0.06096
number of blades = 3
DTRC 4119 (1st comment line for propeller description)
example /ppg file (2nd comment line for propeller description)
number of radial sections = 13
number of sectional profiles = 13 (same radii as other geometry)
description of sectional profiles = BNF
(3rd comment line for descriptive column titles follows)
  r/R      c/D      skew[deg] rake/D   P/D      tmax/c  fmax/c
0.20000 0.32000 0.00000  0.00000  1.10500 0.20550 0.00000
0.25000 0.34200 0.00000  0.00000  1.10370 0.17870 0.00000
0.30000 0.36350 0.00000  0.00000  1.10220 0.15529 0.00000
0.40000 0.40480 0.00000  0.00000  1.09830 0.11800 0.00000
0.50000 0.43920 0.00000  0.00000  1.09320 0.09016 0.00000
0.60000 0.46100 0.00000  0.00000  1.08790 0.06960 0.00000
0.70000 0.46220 0.00000  0.00000  1.08390 0.05418 0.00000
0.80000 0.43470 0.00000  0.00000  1.08110 0.04206 0.00000
0.90000 0.36130 0.00000  0.00000  1.07850 0.03321 0.00000
0.95000 0.27750 0.00000  0.00000  1.07700 0.03228 0.00000
0.97500 0.20448 0.00000  0.00000  1.07609 0.03210 0.00000
0.99000 0.13276 0.00000  0.00000  1.07546 0.03188 0.00000
1.00000 0.00000 0.00000  0.00000  1.07500 0.00000 0.00000
0.20000 17
0.00000 0.01000 0.02500 0.05000 0.10000 (etc. for 17 values x/c)
0.00000 0.02031 0.03240 0.04633 0.06615 (etc. for 17 values yback/c)
0.00000 -0.01815 -0.02787 -0.03859 -0.05320 (etc. for 17 values yface/c)
0.25000 17
0.00000 0.01000 0.02500 0.05000 0.10000 (etc. for 17 values x/c)
0.00000 0.01823 0.02934 0.04230 0.06084 (etc. for 17 values yback/c)
0.00000 -0.01522 -0.02305 -0.03153 -0.04305 (etc. for 17 values yface/c)
.
.
.

```

```

etc. for each of the 13 sectional profiles ordered from root to tip
.
.
.
1.00000 17
0.00000 0.01000 0.02500 0.05000 0.10000 (etc. for 17 values x/c)
0.00000 0.00386 0.00653 0.00974 0.01447 (etc. for 17 values x/c)
0.00000 -0.00203 -0.00275 -0.00333 -0.00391 (etc. for 17 values x/c)
number of Hub offsets = 2 (These lines define a cylindrical hub of
-2.0 0.2 radius 0.2R extending 3R upstream and 2R
3.0 0.2 downstream of the propeller disk.)

```

## D.2. Trident instructions files

### D.2.1. Meshing instructions

Figure D.1 displays an example case of a Mesh instructions (\*.cdr) file. An important note regards the method of notation, which must remain unaltered for all values. That is, the decimal separator and number of digits should remain unaltered. For example, increasing the stiffness by a factor of 10:  $0.800E+03 \rightarrow 0.800E+4$ . The unmarked values can be left to default, listed below are the marked values:

1. Fluid density [ $10^{12} kg/m^3$ ]
2. Number of radial elements
3. First and last radial grid position, normalized by radius (respectively)
4. Number of chordwise elements
5. First and last chordwise grid position, normalized by chord
6. Composite material: 0 = false, 1 = true. In case of a composite, a prp file is required (sec. D.2.2)
7. Young's Modulus [MPa], Poisson's ratio [-], Material Density [ $10^{12} kg/m^3$ ], ignored for composites

```

FLUID
  2
  1 0
(1) 0.998E-09
BLADE1
  2 0
(2) 30 1
(3) 0.2400 0.9950 1.0000
(4) 30 1 0
(5) 0.0050 0.9950 1.0000
  0
BLADE2
(6) 2 0 1 0 0 0
(7) 0.800E+03 0.350E+00 0.650E-09
  0
LOADB
  3 0
LOADV
  0 1 2 0 1 0

```

Figure D.1: Example meshing instructions file

### D.2.2. Composite properties

In case of a composite, the cdr file shown in figure D.1 expands to the file below. Two sections are added (MATMAP and MATMP2), which contain information of the laminate setup. The MATMAP section contains information on subdivisions in the laminate, usually this can remain unaltered. The MATMP2 section is setup similarly as the BLADE1 section, hence the same number of elements/grid positions etc. should be used. The last line in the MATMP2 section describes the components of the first and second principal material axis ( $X_1, Y_1, Z_1, X_2, Y_2, Z_2$ ). The ply properties are described with respect to these axes.

```

FLUID
  2
  1 0
  0.998E-09
BLADE1
  2 0
  30 1
  0.2400 0.9950 1.0000
  30 1 0
  0.0050 0.9950 1.0000
BLADE2
  2 0 1 0 1 0
  0.360E+04 0.300E+00 0.114E-08
  0
LOADB
  3 0
LOADV
  0 1 2 0 1 0
MATMAP
  1 1 0
MATMP2
  1 1 1 0
  30
  0.2400 0.9950
  30
  0.0050 0.9950
  1
  0
  0.0000 1.0000 0.0000 1.0000 0.0000 0.0000

```

Below a typical \*.prp file is shown for an example composite material, the numbers between brackets are not part of the content, but there to indicate the properties described in the list.

```
LAM 1 GRP1 0 2
2.9412E+04 7.9050E+03 7.9050E+03 2.8067E+03 2.2300E+03 2.8067E+03 (1)
3.1200E-01 2.1314E-01 7.8101E-02 1.7080E-09 (2)
1.5050E+03 5.6100E+01 5.6100E+01 3.8681E+02 1.4652E+02 1.4400E+02 (3)
4.9558E+02 4.0059E+02 4.1298E+02 -5.0000E-01 -5.0000E-01 -5.0000E-01 (4)
0.0000E+00 0.0000E+00 0.0000E+00 0.0000E+00 0.0000E+00 0.0000E+00 (5)
0.0000E+00 0.0000E+00 0.0000E+00 (6)
MA5 1 GFRP 4 1
1 0.1000E+01 0.000E+00 (7)
1 0.1000E+01 9.000E+01
1 0.1000E+01 9.000E+01
1 0.1000E+01 0.000E+00
```

1. Young's Moduli:  $E_1 E_2 E_3$ , Shear Moduli:  $G_{12} G_{23} G_{31}$
2. Poisson's ratios:  $\nu_{12} \nu_{23} \nu_{31}$ , Ply density:  $\rho_{ply}$
3. Maximum stresses:  $\sigma_{1,tensile} \sigma_{2,tensile} \sigma_{3,tensile} \sigma_{1,compressive} \sigma_{2,compressive} \sigma_{3,compressive}$
4. Maximum shear:  $\sigma_{12} \sigma_{23} \sigma_{31}$ , Tsai-wu failure parameters:  $F_{12} F_{23} F_{31}$
5. Maximum strains:  $\epsilon_{1,tensile} \epsilon_{2,tensile} \epsilon_{3,tensile} \epsilon_{1,compressive} \epsilon_{2,compressive} \epsilon_{3,compressive}$
6. maximum shear strains:  $\epsilon_{12} \epsilon_{23} \epsilon_{31}$
7. identification number, ply thickness, ply angle

The 1,2 and 3 represent the first, second and third principle material direction respectively. The third principle direction is perpendicular to the plane formed by the first and second principle direction, hence it is not given in the \*.cdr file.

### D.3. PROCAL Control File

An example PROCAL control file for an unsteady analysis in a wakefield is displayed below.

```

;-----
; Solver Definition
; File Generated by DRDC-Atlantic PROVIDE tool
;-----

[Project]
Project_name      = default
Description       = unsteady_analysis
Code_version     = 2.4
ProcalAnalysisType = Unsteady ; Provide Only
ControlFileType  = Propeller ; Provide Only

[Operating_Condition]
NumberOfShipSpeeds = 1
Ship_speed         = 1.19
Rotation_rate      = 5
Prop_diameter      = 0.34
Reference_velocity = 5.1
Reference_length   = 0.34
Density            = 998
Kinematic_viscosity = 1.010e-06
Kp_rough           = 0
Atmospheric_pressure = 102500
Vapour_pressure    = 1700
Gravity            = 9.81
Shaft_immersion    = 2

[Control]
Unsteady_computation = true
Revolutions          = 100
Timesteps_revolution = 36
non-rot_wakepanels_length = 20
Postprocessing_revolutions = 1
HIC_memorystorage    = true
Nearfield_criterion_wake = 8
Farfield_criterion   = 8
Viscous_mode         = 1
Viscous_scale_factor = 1
TE_source_correction = false
TE_source_correction_factor = 1
Ct_minvalue          = 0
Number_parallel_cores = 1
Convergence_dkt_rms  = 0.5
Convergence_dkt_max  = 1

[Kutta_condition]
Iteration           = true
Iteration_cav       = false
Convergence_criterion = 0.01
NumberOfSteps       = 20
Epsilon_jacobian    = 0.01
IPKC_model          = 1

```

```
[Wake_alignment]
Alignment_mode      = 1
Prescribed_pitch    = 2
Prescribed_contraction = 2
Convergence_criterion = 0.01
Relaxation          = 0.2
NumberOfSteps       = 15
X_RfarWake          = 2
Viscous_core        = 0.0025
Convergence_metric  = 1

[Cavitation]
Cavitation_computation = false
Convergence_criterion = 0.01
Revolutions            = 4
Relaxation              = 0
Max_iter_lc            = 20
Detachment_mode        = 0
Cav_wake_ratio         = 0.1
CPmin_s_min_face      = 0
CPmin_s_min_back      = 0
CPmin_s_max           = 0.8
CPmin_r_max           = 1

[Geometry]
NumberOfSurfaceFiles  = 2
SurfaceFiles           = { .\input\S71892_Blade.pan,
                          .\input\S71892_Hub.pan }
SurfaceFilesRotating  = { .\input\S71892_Blade.pan,
                          .\input\S71892_Hub.pan } ; Provide Only
Reference_length      = 2
Propeller_surface     = blade
Hub_surfaces          = hub
Radius_smoothing      = 0.95
splitHub              = false

[Shipwake]
File_type             = 1
WakeFile              = .\wakefield.wak
Wake_correction_factor = 1
RightWardTurningPropeller = true
UseWakeInAlignment   = false
Steady_averaging     = true

[Field_Points]
Calculation           = false
Calculation_type      = 1
FieldPointWakeXcentres = 0

[Hull_Pressures]
CalculationType       = NONE
ViewHull              = false ; Provide Only
nHarmonics            = 2

[Post_processing]
Post_processing_type  = 0
```

```
Post_processing_Aref = 1
Post_processing_Lref = 1
Moment_position      = { 0, 0, 0 }

[DATA]
outputPath = .\procalOutput\
Ascii_output      = true
BodyForces_output = false
Excalibur_output  = false
Logfilethreshold  = INFO
Logscreeenthreshold = INFO
DebugData_output  = true

[SetPointIteration]
Iteration          = false
Target            = Kt
Targetvalue       = 0.3
Convergence_criterion = 0.001
NumberOfSteps     = 10
IterationParameter = "Ship Speed"

[NOZZLE]
Nozzle_computation = false
Nozzle_name        = Duct
Gap_name           = Gap
Boundary_layer_thickness = 0.04
Inflow_boundary_layer = true
Gap_iteration      = false
Cq                 = 0.1
maxIterations      = 5
force_iteration    = Off
Nozzle_force       = 0
source_correction_factor = 0
source_correction_model = Off
```

# Bibliography

- [1] Althaus D. Tunnel-wall corrections at the laminar wind tunnel, 1999. URL [https://www.iag.uni-stuttgart.de/dateien/pdf/laminarwindkanal\\_messtechniken/althaus\\_1.pdf](https://www.iag.uni-stuttgart.de/dateien/pdf/laminarwindkanal_messtechniken/althaus_1.pdf).
- [2] Gay D and Hoa S. *Composite Materials: Design and Applications*. CRC Press, Boca Raton, 2007.
- [3] Hally D, Heath D, and Oakey S. Users guide for provise. *Cooperative Research Ships*, 3.0.12, 04 2018.
- [4] J Dang, H.J.J. van den Boom, and J.Th. Ligtelijn. The wageningen c- and d-series propellers. *MARIN, The Netherlands*, 2013.
- [5] Open Course Ware TU Delft. Vortex cavitation, 2012. URL [https://ocw.tudelft.nl/wp-content/uploads/Chapter\\_9.pdf](https://ocw.tudelft.nl/wp-content/uploads/Chapter_9.pdf).
- [6] Kuiper G. Cavitation on ship propellers, chapter 6. *TU Delft OpenCourseWare*, 2012. URL [https://ocw.tudelft.nl/wp-content/uploads/Chapter\\_6.pdf](https://ocw.tudelft.nl/wp-content/uploads/Chapter_6.pdf).
- [7] Nikishkov G. P. Introduction to the finite element method. *University of Aizu*, 3.0.12, 2004.
- [8] Consultancy Services Group. Procal task 4.1e, panelling procedure. *Technical Investigations*, 2005.
- [9] Lee H, Song M, Suh J, and Chang B. Hydro-elastic analysis of marine propellers based on a bem-fem coupled fsi algorithm. *International Journal of Naval Architecture and Ocean Engineering*, vol. 6, no. 3, pp. 562–577, 2014.
- [10] Rob Haelterman, Joris Degroote, D. Heule, and Vierendeels. The quasi-newton least squares method: A new and fast secant method analyzed for linear systems. *SIAM Journal on Numerical Analysis*, 47:2347, 01 2009. doi: 10.1137/070710469.
- [11] News Hound. An introduction to propeller cavitation. *International Institute of Marine Surveying*, 2015. URL <https://www.iims.org.uk/introduction-propeller-cavitation/>.
- [12] J. Huisman and E. Foeth. Automated multi-objective optimization of ship propellers. *Fifth International Symposium on Marine Propulsors*, 2017.
- [13] Bosschers J. Procal v2.0 theory manual. *Cooperative Research Ships*, 2009.
- [14] Buiten J. *Shipboard Acoustics, Proceedings of the 2nd International Symposium on Shipboard Acoustics ISSA*. Springer Science & Business Media, 1986.
- [15] Franc J.P and Michel J.M. *Fundamentals of Cavitation*. Kluwer, 2001.
- [16] Carlton J.S. *Marine Propellers and Propulsion*. Butterworth-Heineman, 2007.
- [17] Jiasheng L, Yegao Q, and Hongxing H. Hydroelastic analysis of underwater rotating elastic marine propellers by using a coupled bem-fem algorithm. *Ocean Engineering*, vol. 146, no. 1, pp. 178–191, 2017.
- [18] Massachusetts Institute of Technology. Area and bending inertia of airfoil sections, 2005. URL <https://ocw.mit.edu/courses/aeronautics-and-astronautics/16-01-unified-engineering-i-ii-iii-iv-fall-2005-spring-2006/systems-labs-06/sp110b.pdf>.
- [19] Aviation online magazine. Airfoil pressure distribution, 2017. URL <http://avstop.com/ac/flighttrainghandbook/pressuredistribution.html>.
- [20] Maljaars P. Hydro-elastic analysis of flexible marine propellers, 2019. URL <https://doi.org/10.4233/uuid:19c9610b-9a72-42a6-8340-2ba01ec78cc6>.

- [21] van Pelt P. Genesis of the kutta condition. *Delft University of Technology*, 2019. URL <http://resolver.tudelft.nl/uuid:fe4ab61e-310e-488f-aed7-2d82d0ed010c>.
- [22] Sika Advanced Resins. Sikablock® m700 datasheet, 2016. URL [https://advanced-resins.sika.com/content/sikaaxson/main/en/solutions\\_products/product-groups/block-materials/model-and-tooling-boards/sikablock-m700.html](https://advanced-resins.sika.com/content/sikaaxson/main/en/solutions_products/product-groups/block-materials/model-and-tooling-boards/sikablock-m700.html).
- [23] Bart Schuiling. The design and numerical demonstration of a new esd, 2013. URL [https://www.researchgate.net/figure/The-Reference-Frame-for-a-Propeller-in-Oblique-Flow-A-definition-for-fig1\\_305618152](https://www.researchgate.net/figure/The-Reference-Frame-for-a-Propeller-in-Oblique-Flow-A-definition-for-fig1_305618152).
- [24] Stackexchange. Aviation, 2019. URL <https://aviation.stackexchange.com/questions/47251/what-is-the-physical-meaning-of-circulation-found-in-kutta-condition>.
- [25] Ali Takinaci, Mehmet Atlar, and Emin Korkut. A practical surface panel method to predict velocity distribution around a three-dimensional hydrofoil including boundary layer effects. *Ocean Engineering - OCEAN ENG*, 30:163–183, 02 2003. doi: 10.1016/S0029-8018(02)00015-X.
- [26] Koko T.S. and Yuen B.K. Investigation of a composite material configuration for a research vessel propeller. *Applied Technology Group*, 2016.
- [27] Koruche U.S and Patil S.F. Application of classical lamination theory and analytical modeling of laminates. *International Research Journal of Engineering and Technology(IRJET)*, 2015.
- [28] the free encyclopedia Wikipedia. Wing profile nomenclature, 2011. URL [https://en.wikipedia.org/wiki/File:Wing\\_profile\\_nomenclature.svg](https://en.wikipedia.org/wiki/File:Wing_profile_nomenclature.svg).
- [29] He X, Hong Y, and Wang R. Hydroelastic optimisation of a composite marine propeller in a non-uniform wake. *Ocean Engineering*, vol. 39, pp. 14–23, 2012.
- [30] Young Y. Fluid–structure interaction analysis of flexible composite marine propellers. *Journal of Fluids and Structures*, vol. 24, no. 6, pp. 799–818, 2008.
- [31] Young Y.L, Motley M.R, Barber R, Chae E.J, and Garg N. Progress and challenges adaptive composite marine propulsors and turbines: Progress and challenges. *ASME*, 2016.